# ENABLING HIGHER ENERGY AND POWER DENSITY LITHIUM ION BATTERIES THROUGH ELECTRODE DESIGN AND THE INTEGRATION OF SOLID-STATE ELECTROLYTES

By

Yunsung Kim

# A DISSERTATION

Submitted to
Michigan State University
in partial fulfillment of the requirements
for the degree of

Materials Science and Engineering - Doctor of Philosophy

2015

#### **ABSTRACT**

# ENABLING HIGHER ENERGY AND POWER DENSITY LITHIUM ION BATTERIES THROUGH ELECTRODE DESIGN AND THE INTEGRATION OF SOLID-STATE ELECTROLYTES

By

#### Yunsung Kim

At present, Li-ion technology is the leading battery chemistry to enable the large-scale adoption of electric vehicles. However, meeting the demands of hybrid and plug-in hybrid electric vehicles requires higher specific and volumetric energy density, faster charge rates, longer cycle life, and improved safety. A particular focus is on achieving high power density without compromising energy density. This dissertation seeks to determine the phenomena that couple energy and power density and to develop solutions to simultaneously increase both. An engineered electrode design is proposed that improves Li-ion transport in thick high energy density electrodes, while suppressing the deleterious formation of Li metal dendrites during charging. Furthermore, a novel hybrid cell design is proposed employing Li<sub>7</sub>La<sub>3</sub>Zr<sub>2</sub>O<sub>12</sub> (LLZO) ceramic electrolyte membrane technology, which acts as a physical barrier to prevent Li metal dendrite propagation. The overarching goal of this dissertation is to develop materials and materials processing technology to improve the performance and safety of Li-ion batteries.

Copyright by YUNSUNG KIM 2015

#### **ACKNOWLEDGEMENTS**

First, I would like to express my sincere appreciation to my advisor Dr. Jeff Sakamoto for giving me this opportunity to work in the field of energy storage. I would like to sincerely express my gratitude for his advice and his support throughout my Ph. D. degree. I would like to thank him for encouraging me to challenge myself and always do better.

I would like to thank my great colleagues of Dr. Sakamoto's group, including Dena Shahriari, Maria Regina Garcia Mendez, Asma Sharafi, Dan Lynam, Isabel David, Dr. Youngsam Park, Dr. Ezhilyl Rangasamy, Dr. Travis Thompson, Dr. Heechul Lee, Dr. Robert Schmidt, Dr. Eric Jianfeng Cheng, and others who always support me in intelligently and emotionally.

I would like to thank my committee members Dr. Carl Boehlert, Dr. Scott Calabrese Barton, Dr. Donald Morelli, and Dr. Viktor Poltavets for agreeing to be part of my committee. I would also like to thank them for their precious time and for their great personality to help me throughout the course of this Ph. D.

I would like to express my sincere appreciation to my former advisor Dr. Heeman Choe and his group: Eunji Hong, Dr. Hyelim Choi, Taehoon You, Minchol Hyeon, Yoonsook Noh, Dongjun Shin, Hyoungjoo Lee, Myounggeun Choi, Hyungyung Jo, Hyeji Park, Jooyoung Kim and Jina Kim who giving brains to me whenever I am having a tough time.

I have to also thank Dr. Jeff Wolfenstine, Dr. Andy Drews, Dr. Raji Chandrasekaran, Dr. Ted Miller, Eongyu Yi, and Per Askeland for their assistance in interpretation and characterization in my research.

Finally I would like to thank my parents Guansuck Kim and Yoosoon Jang, my sister Jinyoung Kim, and my brother Hyunsung Kim for their unconditional support and love during my Ph. D. studies. I would like to express my sincere appreciation to them respecting this endeavor.

# TABLE OF CONTENTS

LIST OF T	TABLES	ix
LIST OF F	IGURES	X
1 Introdu	action	1
1.1	Energy demand and storage technology need	
1.2	Energy storage technologies	
1.3	Li-ion batteries	
1.3.1	Li-ion battery operation principles	
1.3.2	Negative electrodes (anodes)	
	1.3.2.1 Graphite negative electrodes	
	1.3.2.2 Alloy negative electrodes	
1.3.3	Positive electrodes (cathodes)	
	1.3.3.1 Layered positive electrode compounds	
	1.3.3.2 Spinel positive electrode compounds	
	1.3.3.3 Olivine positive electrode compounds	
1.3.4	Electrolytes	
	1.3.4.1 Liquid electrolyte	
	1.3.4.2 Garnet-like solid electrolyte	
1.4	Challenges for electric vehicle systems	
1.4.1	Power and energy	
1.4.2	Safety	
1.5	Need for cell design	
1.5.1	Electrode design approaches	
1.5.2	Cell design with garnet-like solid electrolyte	
1.6	Scope of present work	
2 Experi	mental methodology	28
2.1	Electrode preparation	
2.2	Ceramic electrolyte processing	
2.2.1	Powder preparation	
2.2.2	Consolidation	
2.3	Electrochemical measurement methods	
2.3.1	Galvanostatic rate mapping test	32
2.3.2	Intentional overcharge test	
2.3.3	Galvanostatic intermittent titration technique (GITT)	
	2.3.3.1 Polarization interrupt test	
2.3.4	Electrochemical impedance spectroscopy (EIS)	
	2.3.4.1 Transmission line model (TLM) and electrochemical	
	spectroscopy using symmetric electrode (EIS-SC)	
2.4	Mechanical property characterization	
2.4.1	1 1 1	

2.4.2	Nano indentation	48
2.5	Other methods	49
2.5.1	Laser patterning	49
2.5.2	X-ray power diffraction (XRD)	
2.5.3	Scanning electron microscope (SEM)	
2.5.4	Raman	
3 Determ	nining power limiting process and understanding cell failure mechanisms	53
3.1	Intercalation vs deintercalation rate	
3.2	Rate limiting processes	
3.2.1	Electron injection and extraction resistances	
3.2.2	Ion insertion and extraction resistances at the interface between electrode and	
electro	lyte	57
	3.2.2.1 SEI and charge transport resistances	
	3.2.2.2 Tortuosity	
	3.2.2.3 Solid-state diffusion in graphite electrode	
3.3	Understanding cell failure mechanisms	
3.4	Summary	
	, and the second	
4 Laser p	patterned electrodes	73
4.1	Background: three dimensional (3D) electrode designs	73
4.2	Highly ordered hierarchical (HOH) graphite electrode	79
4.2.1	Laser patterning technique	
4.2.2	HOH electrode design	
4.2.3	HOH electrode design optimization	82
4.2.4	HOH electrode characterization	87
	4.2.4.1 Phase characterization by Raman spectroscopy	87
	4.2.4.2 Morphological analysis	
4.3	Summary	
5 Electro	chemical characterization of HOH electrodes	92
5.1	Solid-state Li diffusivity in graphite electrode	92
5.2	Rate mapping	
5.2.1	Effects of loading	
5.2.2	HOH graphite electrode vs conventional graphite electrode	97
	5.2.2.1 Effects of separators	
5.3	Cell impedance characterization	107
5.3.1	Polarization interrupt test	107
5.3.2	Transmission line method (TLM) and EIS characterization	108
	5.3.2.1 Reliability of TLM based EIS-SC technique	110
	5.3.2.2 Comparison the internal resistance of HOH electrodes vs conven	tional
	electrodes	114
5.4	Summary	116
6 The eff	fect of microstructure on the mechanical properties of hot-pressed cubic Li <sub>7</sub> La <sub>3</sub> Z	Zr <sub>2</sub> O <sub>12</sub>

6.1	LLZO ceramic electrolyte characterization	119
6.1.1	Density of LLZO	119
6.1.2	Phase characterization	119
6.1.3	Micro structure of LLZO	121
6.2	Mechanical properties of LLZO	127
6.2.1	Hardness of LLZO	127
6.2.2	Fracture toughness of LLZO	131
6.3	Ionic conductivity of LLZO	134
6.4	Summary	136
7 Summa	ry and future work	138
7.1	Summary	
7.2	Future work	
7.2.1	HOH charge abuse testing	139
7.2.2	Rate mapping at low temperature	
7.2.3	Realizing a novel hybrid cell design with ceramic electrolytes	
REFERENO	CES	147

# LIST OF TABLES

Table 1-1: USABC target of obtaining a high-energy storage and low-cost electric vehicle bapplications [57]. Depth of discharge (DOD), State of charge (SOC)	•
Table 2-1: Equations for fracture toughness based on Vickers hardness technique. ( $E$ Young's modulus, $H_v$ is the Vickers hardness, $c$ is the crack length, $a$ is the length of diagonal, and $P$ is the applied load.)	f half
Table 6-1: It presents the information of hot-pressed LLZO pellets as changing hot-pressing	

# LIST OF FIGURES

Figure 1-1: Comparison of the different battery systems in terms of gravimetric power and energy density [7]
Figure 1-2: Schematic of the principle operation of a Li-ion battery [7]. (Modified from [16])5
Figure 1-3: Schematic of (a) Li-ion intercalation process between graphene layers, (b) staging of graphite during Li intercalation process [22]. (Modified from [24])
Figure 1-4: (a) Voltage <i>vs</i> capacity of various electrode materials [28], (b) Volume change effects associated to the charge and discharge processes of metal Li-alloying electrodes in Li-ion battery (left lower) [27]. SEM images of the discharged Sn at different cycle numbers [26]10
Figure 1-5: The crystal structure of cubic LLZO.
Figure 1-6: Correlation between specific energy, electrode loading, and open porosity assuming LiMO <sub>2</sub> , graphite, 10 μm Cu foil, 19 μm Al foil, and no packaging21
Figure 1-7: Dependence of the power capability of SFG44 graphite electrodes in the electrode loading [19]
Figure 1-8: Schematic of hybrid cell design composed of graphite negative electrode, LiCoO <sub>2</sub> positive electrode, liquid electrolyte, and LLZO ceramic electrolyte where between electrodes25
Figure 1-9: Ragone plot for various energy devices [72]
Figure 2-1: Processes flow diagram describing the graphite electrode fabrication process29
Figure 2-2: (a) An image of the rapid induction hot-pressing. (b) Schematic of the cross-section of a graphite die with LLZO power for hot-press
Figure 2-3: (a) An image of a Swagelok® cell with 1/2 inch diameter stainless steel 304 pins. (b) Schematic and the image of stepped stainless steel 304 pins (Outer diameter: 1/2 inch, inner diameter: 3/8 inch), and (c) Swagelok® cell under pressure (45 N) by a force gage
Figure 2-4: Typical GITT plot.
Figure 2-5: Schematic of a symmetric cell for a free-standing electrode [80]40
Figure 2-6: Schematics of (a) a typical equivalent circuit for a solid electrolyte and (b) a cell preparation with solid electrolyte between blocking electrodes for EIS

Figure 2-7: Schematics of (a) simple equivalent circuit model and (b) a typical Nyquist behavior for porous electrodes
Figure 2-8: Nyquist plots for symmetric cells using two positive electrodes. (a) $SOC = 0\%$ (squares) and (b) $SOC = 50\%$ (circles). The solid lines are the best-fitted results with the equivalent circuits using $Eq. 2-6$ and $Eq. 2-7$ for (a) and (b), respectively [83]45
Figure 2-9: The laser patterning equipment fabricated by integrating a computer numerical control (CNC) 3D positioning system with the laser beam
Figure 3-1: Charge and discharge rate mapping of the low loading (1.15 mAh cm <sup>-2</sup> and 50 % total open porosity) graphite electrodes. Black data: Intercalation (charge) rate capability, Red data: deintercalation (discharge) rate capability.
Figure 3-2: (a) Schematic representation of possible Li-ion diffusion paths in electrolyte-filled pores in a graphite electrode, (b) Li intercalation process at a particle scale
Figure 3-3: Two mechanisms for the electrochemically induced reduction of carbonate-based solvents. RA is an abbreviation for "radical anion" [100]
Figure 3-4: Complex impedance plot of Li/graphite half-cell in the delithiated state (SOC=0%).60
Figure 3-5: (a) 3D reconstruction of a graphite electrode (2.8 mAh cm <sup>-1</sup> and 40 %) by FIB-SEM technique using MIMICS® software. (b) SEM image of a graphite electrode by FIB-SEM64
Figure 3-6: Schematic of spherical graphite particle. This figure shows solid state diffusion time according to SOC level. <i>L</i> is diffusion length, <i>t</i> is time for Li diffusion, and <i>D</i> is Li diffusion coefficient.
Figure 3-7: A schematic of thermal runaway causes fires by improper charging in Li-ion batteries. (a) normal state battery, (b) Li dendrite formation due to improper charge such as fast charging, (c) short-circuiting by Li dendrite growth and short circuit on the positive electrode causing instantaneous discharge, (d) cell temperature goes up (>70 °C) by Joule heating and electrolyte start to decompose, then flammable hydrocarbon gases are released, (e) Joule heating and exothermic reactions further increase temperature, and the metal oxide positive electrode starts to decompose (>150 °C), then releasing oxygen. These steps can cause cell failure and explosion. (Cell swelling figure [65])
Figure 3-8: (a) Optical image of the surface and (b) fracture surface of over charged SFG6 graphite electrode at 1 C-rate for 1 h, and (c) optical images represent color change in SFG6 graphite electrode by SOC
Figure 4-1: Previously reported 3D architecture electrode designs and fabrication methods. (a) Process for fabricating the hierarchical $V_2O_5$ electrode [68]. (b) Outline of the Ni foam fabrication by template based method. Lower image is $MnO_2$ electrode fabricated by electrodeposition on Ni foam [69]. (c) A schematic of 3D image of pillars by Super ink jet

printing [120]. (d) Outline of the electrode fabrication process. Left lower shows the surface of a patterned electrode and right lower shows cross-section of a patterned electrode [70]77
Figure 4-2: Schematic representation of possible Li-ion diffusion paths (a) in a conventional porous electrode, (b) in a HOH electrode, and schematic of top view of HOH electrode and short Li-ion diffusion length induced by hexagonal close-packed linear channels
Figure 4-3: Secondary SEM images of laser patterned electrode (Timcal, SFG6, 4.0 mAh cm <sup>-2</sup> , 50 % porosity) (a) top view of fabricated HOH electrode, (b) cross-section of a conical shaped pattern, (c) collapsed walls between laser-ablated channels, and (d) a laser cut HOH electrode after laser patterning (3/8 inch diameter).
Figure 4-4: Raman spot analysis of an HOH graphite electrode at various spots (1 to 4 and cross-section).
Figure 4-5: SEM images of laser patterned graphite electrode (SFG6 graphite electrode with 5.5 mAh cm <sup>-2</sup> and 50 % total open porosity). (a) Top view of HOH electrode before and (b) after rate mapping90
Figure 5-1: Typical potential <i>vs</i> x in Li <sub>x</sub> C <sub>6</sub> plot with 1.2 mAh cm <sup>-2</sup> and 63 % SFG6 graphite electrode.
Figure 5-2: The GITT plot of the graphite electrode with 1.2 mAh cm <sup>-2</sup> and 63 % porosity. The measured potential range was 80 mV to 0.75 V95
Figure 5-3: Results of rate mapping as a function of graphite electrodes with various loading from 1.15 mAh cm <sup>-2</sup> to 5.5 mAh cm <sup>-2</sup> with the same total open porosity (50 %). N=497
Figure 5-4: Charge rate mapping as a function of SFG6 graphite electrodes with conventional and HOH electrodes with 50 % total open porosity. (a) Capacity (%) <i>vs</i> intercalation rate with 4 mAh cm <sup>-2</sup> , (b) with 5.5 mAh cm <sup>-2</sup> , and (c) specific capacity (mAh g <sup>-1</sup> ) <i>vs</i> intercalation rate with 5.5 mAh cm <sup>-2</sup> . N=4
Figure 5-5: Schematic diagram showing the Li concentration and diffusivity profiles in a graphite electrode [126]
Figure 5-6: SEM images of (a) Celgard 2400® and (b) Zeus® separators
Figure 5-7: Typical preconditioning cycles with Zeus® separators and with different graphite electrode loadings, which were (a) 1.2 mAh cm <sup>-2</sup> and (b) 5.5 mAh cm <sup>-2</sup> , respectively106
Figure 5-8: Galvanostatic polarization, followed by interrupt and relaxation test (HOH vs Conventional electrode with 5.5 mAh cm <sup>-2</sup> and 50 %), and the schematic of symmetric cells for polarization interrupt [80].

Figure 5-9: Simulated Nyquist plots for a cylindrical pore in an electrode with different models. (a) Non-faradaic, (b) faradaic with low charge transfer resistance, and (c) is faradaic with high charge transfer resistance [83]
Figure 5-10: (a) Schematic representation symmetric cell (SC)[83], Nyquist plots after TLM-EIS-SC tests with (b) 1.2 mAh cm <sup>-2</sup> and 50 % and (c) 5.5 mAh cm <sup>-2</sup> and 50 % SFG6 symmetric cells
Figure 5-11: Nyquist plots for symmetric cells with two graphite electrodes at SOC 0 %. The loading of 5.5 mAh cm <sup>-2</sup> and porosity of 50 % conventional graphite electrodes were used114
Figure 5-12: Nyquist plots after TLM-EIS-SC test with HOH symmetric cell (5.5 mAh cm <sup>-2</sup> and 45 + 5 %).
Figure 6-1: X-ray diffraction patterns of Li <sub>6.19</sub> Al <sub>0.27</sub> La <sub>3</sub> Zr <sub>2</sub> O <sub>12</sub> calcined powder and hot-pressed pellets pressed for 30, 60, 90, and 240 min at 1050°C. * Pyrochlore (La <sub>2</sub> Zr <sub>2</sub> O <sub>7</sub> )120
Figure 6-2: Fracture surface of $\text{Li}_{6.19}\text{Al}_{0.27}\text{La}_3\text{Zr}_2\text{O}_{12}$ hot-pressed for: (a) 30 min, (b) 60 min, (c) 90 min, and (d) 240 min. The relative densities are indicated in top right of each image
Figure 6-3: Li <sub>6.19</sub> Al <sub>0.27</sub> La <sub>3</sub> Zr <sub>2</sub> O <sub>12</sub> hot-pressed pellets after thermal etching at 700°C for 30 min in air. The Li <sub>6.19</sub> Al <sub>0.27</sub> La <sub>3</sub> Zr <sub>2</sub> O <sub>12</sub> pellets were hot-pressed at 1050°C for: (a) 30 min, (b) 60 min, (c) 90 min, and (d) 240 min. The relative densities are indicated in top right of each image
Figure 6-4: Grain size distributions of hot-pressed Li <sub>6.19</sub> Al <sub>0.27</sub> La <sub>3</sub> Zr <sub>2</sub> O <sub>12</sub>
Figure 6-5: $H_v$ and $H_n$ of Li <sub>6.19</sub> Al <sub>0.27</sub> La <sub>3</sub> Zr <sub>2</sub> O <sub>12</sub> as a function of relative density
Figure 6-6: $H_v$ $vs$ lattice parameter for single crystalline garnets from the literature (open squares)[139] and the value for $Li_{6.19}Al_{0.27}La_3Zr_2O_{12}$ from this work (closed square)130
Figure 6-7: Fracture toughness of $Li_{6.19}Al_{0.27}La_3Zr_2O_{12}$ as a function of relative density132
Figure 6-8: The Vickers indentation crack propagation path trajectories for (a) relative density of 85 % and (b) relative density of 98 %. Arrows point to crack the propagation path in each grain
Figure 6-9: Total ionic conductivity of $Li_{6.19}Al_{0.27}La_3Zr_2O_{12}$ as a function of relative density135
Figure 7-1: (a) Optical top image and (b) fracture surface images of electrode with 5.5 mAh cm <sup>-2</sup> and 35 total porosity (30 % intrinsic porosity and 5 % laser ablated porosity) after overcharging at 1 C-rate for 1 h
Figure 7-2: Schematic of (a) cell configuration for asymmetric DC test, (b) the results of the DC test, and (c) DC cycling test. The DC test was conducted after conditioning cycles at 0.01 mA

cm <sup>-2</sup> for 10 symmetric cycles (each cycle takes 2h). Then DC cycling test was conducted	at 1
mA cm <sup>-2</sup> for 20 cycles. The each cycle takes 2h.	.144
Figure 7-3: Schematic of novel hybrid design of Li-ion batteries with combining HOH con	icept
and LLZO electrolyte for the higher performance and safety	. 146

#### 1 Introduction

# 1.1 Energy demand and storage technology need

Fossil fuels are the primary source of anthropogenic energy [1-2]. However, fossil fuels are not only non-renewable energy sources, their combustion results in air pollution such as carbon dioxide, sulfur dioxide, and nitrous oxide, the latter of which converts into ozone in the presence of sunlight [1,3]. To reduce and eventually eliminate the dependency on fossil fuels, renewable energy resources and technology have been investigated [4]. Most of the more mature renewable energy sources, such as thermal, wind, and solar energies, do not produce greenhouse gases, but they do not continuously produce energy [1,4]. To facilitate renewable energy generation technologies, complementary energy storage technology is needed.

## 1.2 Energy storage technologies

The large-scale stationary energy storage technologies enable to use intermittent renewable energy along the energy demand curve. Therefore, energy storage technology is a key enabler for the implementation of electric vehicles and the smart grid concept. However, developing large scale energy storage systems is not trivial.

Energy storage systems can be divided into several different categories such as mechanical, electrical, chemical, and electrochemical [5]. Examples of mechanical energy storage systems include flywheels, compressed air energy storage, and pumped-storage hydroelectricity (pumped hydro). Examples of electrical storage systems are capacitors and superconductive electromagnetic storage. An example of chemical storage is the energy stored in the form of

hydrogen. Electrochemical energy storage systems are those such as rechargeable battery, fuel cells, and redox flow batteries. Each energy storage systems typically have distinguishing performance characteristics, i.e. supercapacitors have high specific power (>10<sup>3</sup> W kg<sup>-1</sup>), but low energy density (<10 Wh kg<sup>-1</sup>)[6]. Electrochemical energy storage systems are typically considered as one of the most promising energy storage technologies because they generally possess a number of desirable characteristics such as long cycle life, moderate power and energy, high efficiency, and eco-friendly chemistry [7].

To date, several different types of batteries have been developed and utilized. A rechargeable battery is an electrochemical energy storage device that is able to store electrical energy, in the form of chemical potential, and convert the chemical energy into electricity, reversibly. Batteries are typically composed of negative electrode, positive electrode, and liquid electrolyte. During charging and discharging, ions move through the electrolyte, and electrons transport via an external circuit to maintain charge neutrality in the cell. The cell potential is determined by Nernst equation. Nickel-metal hybrid batteries are still used for some portable devices, but are being replaced by Li-ion. At present, lead-acid batteries are widely adopted as the battery of choice for vehicle starting and back up grid storage. In comparison, Li-ion batteries have the highest specific energy and power compared to other battery types (Figure 1-1)[7]. More detailed discussion about Li-ion batteries is presented below.

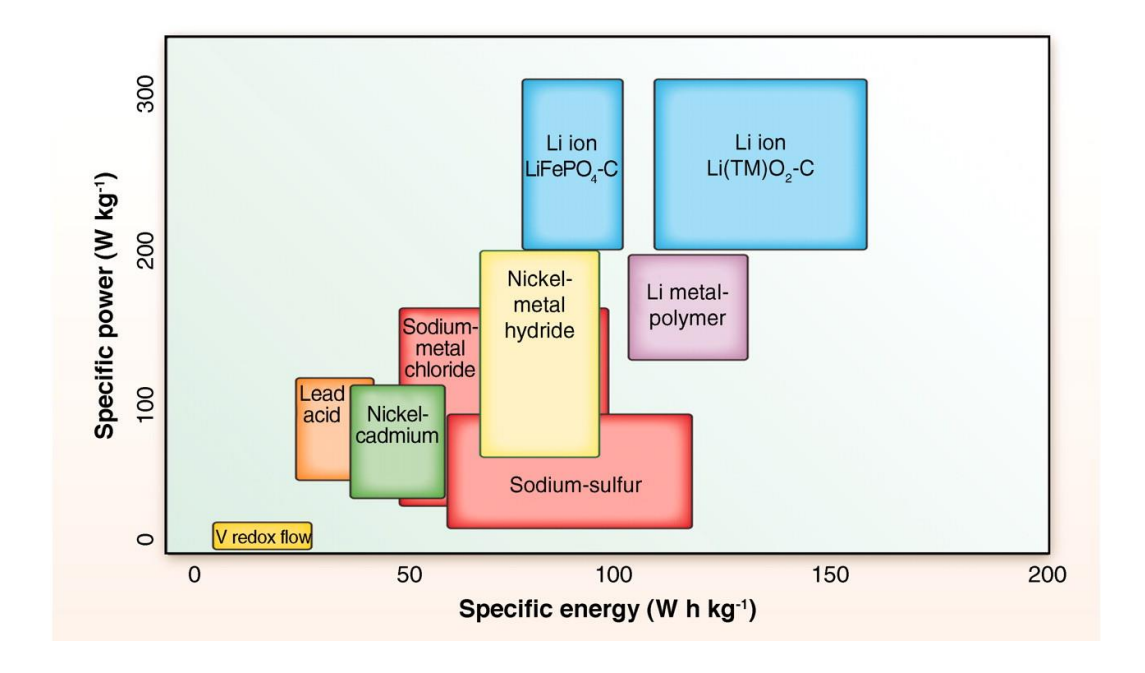


Figure 1-1: Comparison of the different battery systems in terms of gravimetric power and energy density [7].

#### 1.3 Li-ion batteries

Since Li has not only low redox potential to generate high cell voltage (-3.04 V *vs H/H*<sup>+</sup>), it is also light weight (0.53 g cm<sup>-3</sup>), making it a promising candidate electrode for batteries [8]. However, the use of metallic Li as a negative electrode is hindered by the formation of Li dendrites, which can cause short-circuiting leading to ignition [8]. To mitigate the Li electrode instability, yet take advantage of the low redox potential, alternative carbon-based negative electrodes were developed [9]. Rather than depositing Li on the surface, Li-ions are inserted into carbon-based negative electrodes, thus enabling the invention of Li-ion batteries. In 1991, the Sony® Corporation commercialized Li-ion batteries and since has dominated the market for

portable electronic devices such as cellular phones, computers, and digital cameras due to their high energy density compared to other batteries [4,8-11].

# 1.3.1 Li-ion battery operation principles

Li-ion batteries consist of three primary components: (i) a graphite negative electrode (anode), (ii) a non-aqueous liquid electrolyte permeating a porous polymeric membrane (separator) to transport Li-ions between electrodes, and (iii) a transition metal oxide, such as LiCoO<sub>2</sub>, LiMn<sub>2</sub>O<sub>4</sub>, or LiNi<sub>0.33</sub>Mn<sub>0.33</sub>Co<sub>0.33</sub>O<sub>2</sub> positive electrode (cathode)(Figure 1-2)[7,12-14]. During operation, Li-ions are inserted or extracted from the electrodes and diffuse through the liquid electrolyte while electrons are transported through an external circuit to maintain charge neutrality in the cell (Figure 1-2)[7]. The graphite negative electrode and transition-metal oxide positive electrode get reduced during the charge and discharge processes, respectively. The half-reactions and overall cell reaction can be written as

$$xLi^{+} + Li_{1-x}CoO_{2} \xrightarrow{Discharge} LiCoO_{2}$$

$$Li^{+} + e^{-} + 6C \xrightarrow{Discharge} LiC_{6}$$

$$6C + LiCoO_{2} \xrightarrow{Discharge} Li_{x}C_{6} + Li_{1-x}CoO_{2}$$

The chemical driving force for charge and discharge is caused by the difference of the chemical potentials between the electrode materials. The driving force for the redox reactions during charge and discharge processes is given by

$$\Delta G_r^o = -zFE$$
 (Eq. 1-1)

where  $\Delta G_r^o$  is free energy change for the reaction, z is the charge number of the mobile ionic species, F is Faraday constant (96,500 C), and E is cell potential between electrodes [15].

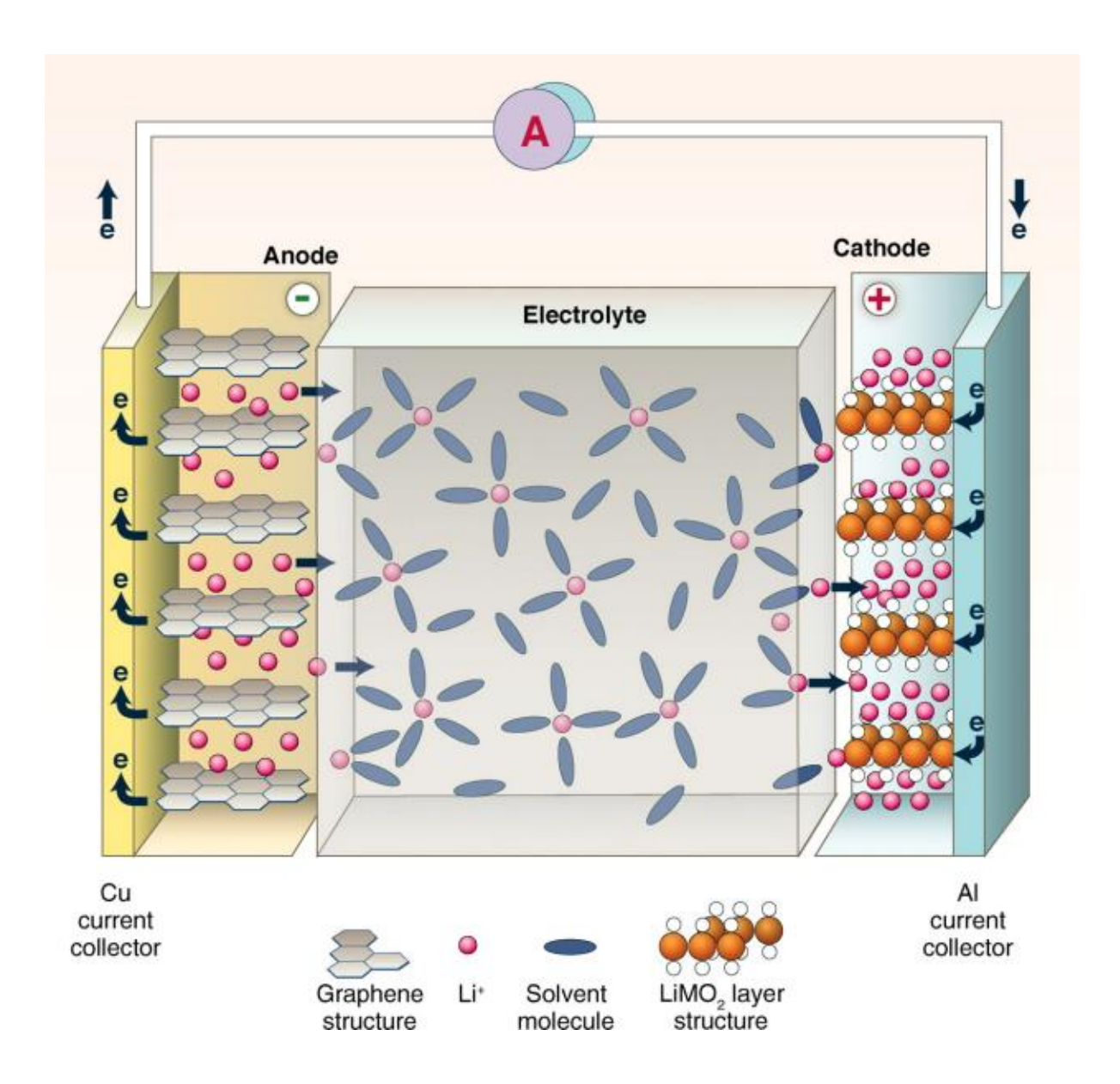


Figure 1-2: Schematic of the principle operation of a Li-ion battery [7]. (Modified from [16])

#### 1.3.2 Negative electrodes (anodes)

Based on convention, the negative electrode is the electrode where oxidation occurs during discharge [17]. To maximize battery performance, the negative electrode materials should have several attributes [15]. First, it should have a low redox potential to provide high cell potential when coupled with a relatively high redox potential positive electrode. Second, the volume change should be minimized during cycling to reduce fatigue and decrepitation. Third, the negative electrode materials ideally should be a mixed conductor with equally high ionic and electronic conductivity. The ionic and electrical conductivity limit how quickly a Li-ion battery can be charged and discharged or also referred to as power. Lastly, it should have a high specific and/or volumetric capacity to maximize the quantity of Li stored per unit mass or volume, respectively.

# 1.3.2.1 Graphite negative electrodes

Yazami *et al.*[18] was the first to propose the use of a graphite negative electrode in 1983. Today, graphite negative electrodes are almost exclusively used in state-of-the-art commercial Li-ion batteries owing to their relatively long cycle life, low discharge potential, low cost, and abundance of precursors [9,19-20]. Graphite exhibits sp<sup>2</sup>-hybridized bonding, and consists of stacked layers of graphene. The layers are bonded by weak Van der Waals force caused by the  $\pi$ -orbitals [21]. Since the  $\pi$  electrons can transport between the graphite layers relatively freely, graphite has a high electrical conductivity. During charging, Li-ions are electrochemically inserted between graphene planes at low potential ( $\leq 0.25 \text{ V } vs \text{ Li/Li}^+$ )(Figure 1-3a)[12,22].

Several Li-ion staging phenomena comprise distinct Li-C ordering when x varies between 0 and 1 in  $Li_xC_6$ , which has a theoretical specific capacity of 372 mAh g<sup>-1</sup> [19]. As shown in Figure 1-3b, the intercalation of Li-ions into graphite shows several plateau regimes (staging). This staging is a thermodynamic phenomenon, and indicates that graphite undergoes phase transition from ABAB stacking to AAAA stacking filled with Li-ion between every graphite layers (Figure 1-2b)[22-23]. The plateau regimes exhibit coexistence of two phases resulted from a difference in the energy required to expand the graphene layers and the repulsive force between Li-ions [22-23].

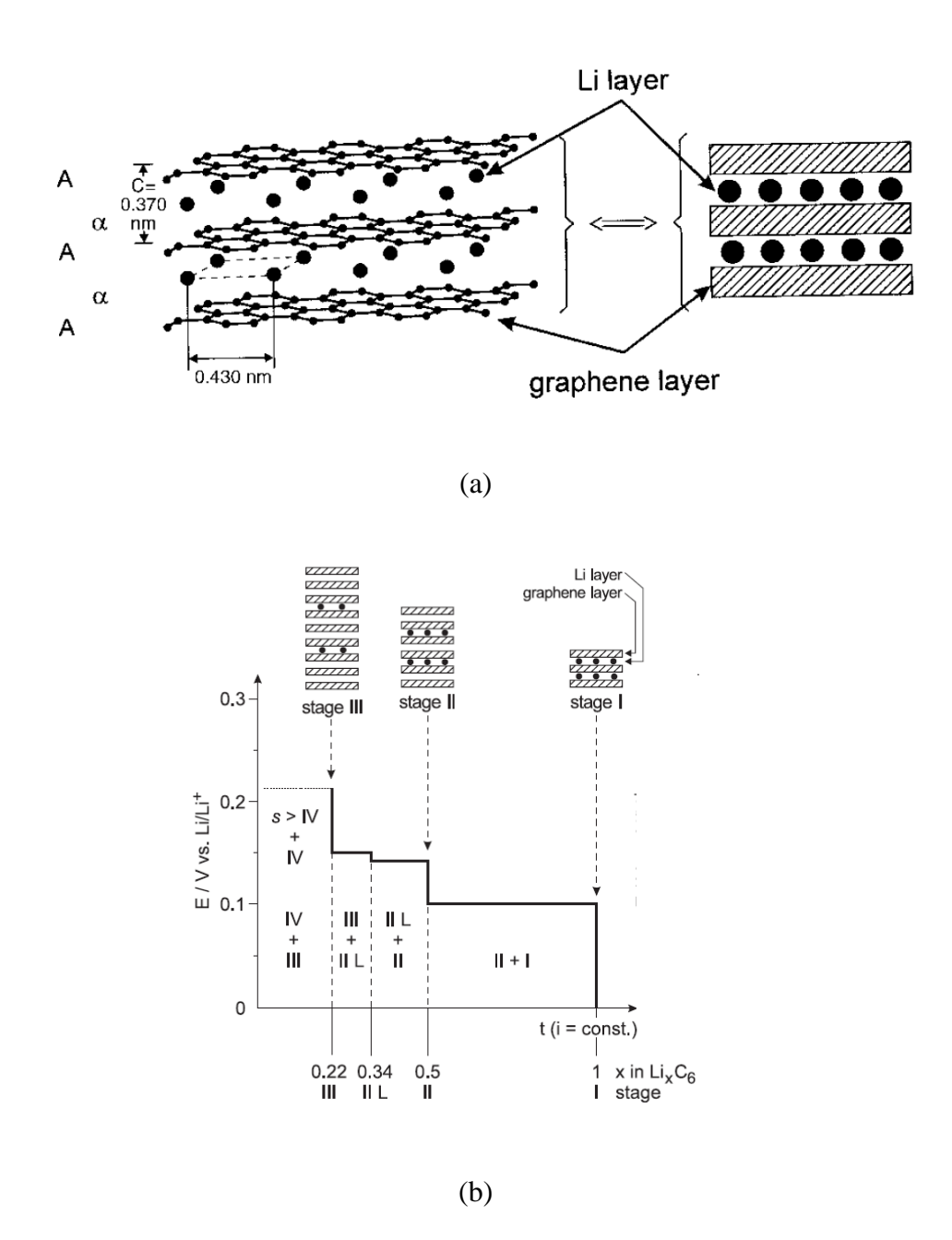


Figure 1-3: Schematic of (a) Li-ion intercalation process between graphene layers, (b) staging of graphite during Li intercalation process [22]. (Modified from [24])

# 1.3.2.2 Alloy negative electrodes

In recent years, Li-alloying materials, such as Si and Sn, have been considered as attractive negative electrode materials due to their significantly high theoretical energy capacities [25-27]. During charging, alloys store Li by forming Li compounds [12,25-27]. The Li-alloying process can be presented by the following reactions [12]:

$$M + xLi^{+} + xe^{-} \xrightarrow{Discharge} Li_{x}M$$

where M is Si, Sn, Pb, Sb, Al, and Bi. As a result, theoretical energy capacities of Si and Sn are 4200 mAh g<sup>-1</sup> and 992 mAh g<sup>-1</sup>, respectively [25-27]. Although the maximum energy capacity of these materials is 10 times higher than that of a conventional graphite electrode (372 mAh g<sup>-1</sup>), they have relatively high operating potentials resulting in lower cell potentials (Figure 1-4a)[28]. Also, alloys are notorious for undergoing severe volume change during cycling (Figure 1-4b)[8,26-27]. For example, the processes of alloying and dealloying cause a volume change up to 400 % in a Si negative electrode [25]. The mechanical stress related to expansion and contraction leads to decrepitation of the electrode and capacity rapidly fade (Figure 1-4b)[26-27]. To alleviate these problems, various approaches such as reducing particle size, designing stress-reducing structures, and selecting intermetallic alloys are suggested [8,25-27]. Despite these efforts to reduce volume expansion, the short cycle life of Si and/or Sn has still not been solved [8].

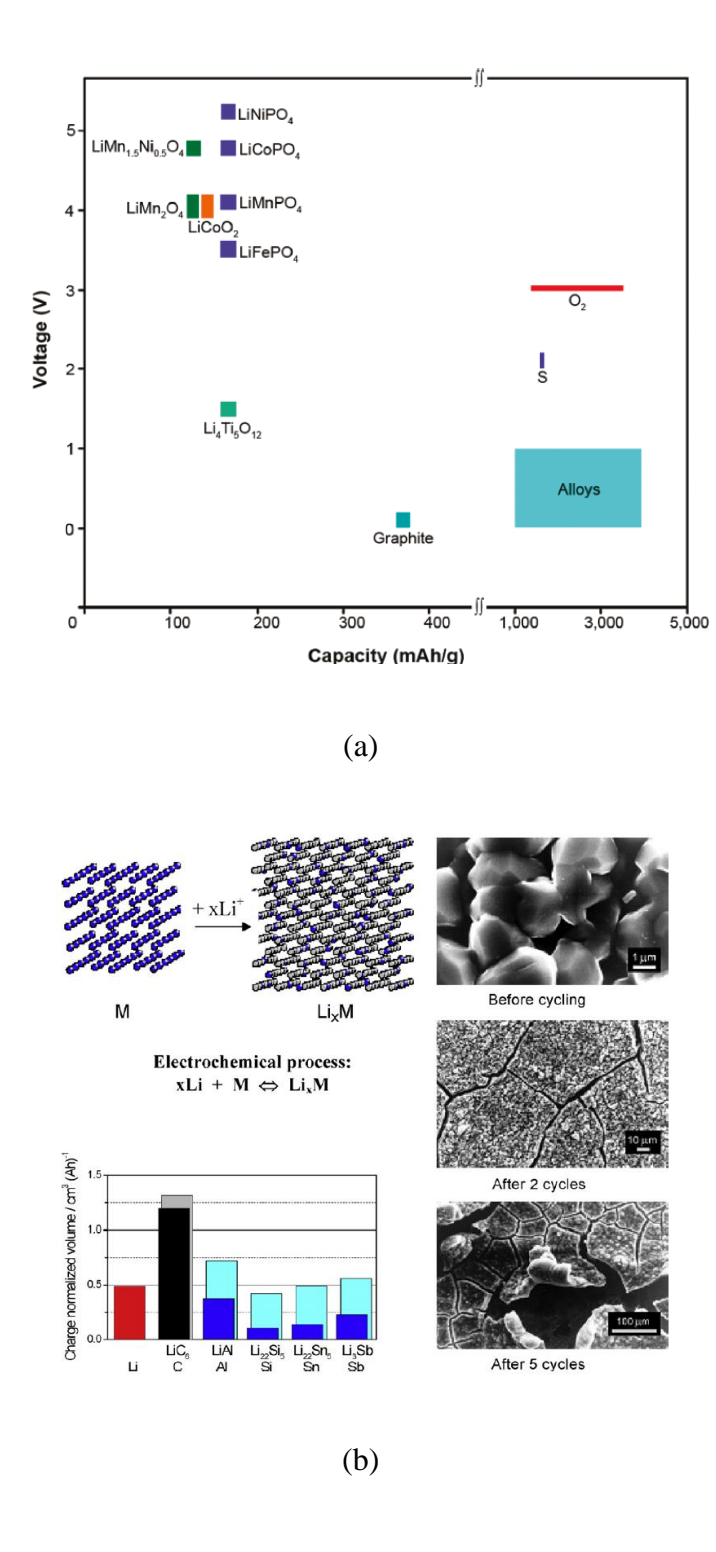


Figure 1-4: (a) Voltage *vs* capacity of various electrode materials [28], (b) Volume change effects associated to the charge and discharge processes of metal Li-alloying electrodes in Li-ion battery (left lower) [27]. SEM images of the discharged Sn at different cycle numbers [26].

#### 1.3.3 Positive electrodes (cathodes)

Based on convention, the positive electrode is the electrode where reduction occurs during discharge [15,17]. LiCoO<sub>2</sub> was the positive electrode material originally paired with graphite electrode [29]. LiCoO<sub>2</sub> is a good example of a positive electrode because it has relatively high redox potential, is a chemically and thermally stable structure, and is a good mixed conductor. In general, positive electrode materials can be classified based on their atomic structure such as layered, spinel, and olivine compounds [30]. Spinel and olivine refer to general mineral names for families of transition metal oxides. The requirements for positive electrode materials are high specific and volumetric capacity, power, cycle life, and safety [30]. To maximize the quantity of Li stored per unit mass or volume, a high specific and/or volumetric capacity is required, respectively. In addition, the irreversible phase transition should not occur for long cycle life, and the chemical and electrochemical stabilities are required for safety, respectively.

# 1.3.3.1 Layered positive electrode compounds

The layered structure compounds with LiMO<sub>2</sub> (M=Co, Ni, and Mn) consist of the oxygen anions forming a close-packed structure with cations located in the 6-fold coordinated octahedral sites. The LiMO<sub>2</sub> compounds exhibit the O-Li-O-M-O-Li-O-M-O (MO<sub>2</sub>-Li-MO<sub>2</sub>-Li) repeating structure. Since the MO<sub>2</sub> layer forms strong ionic bonds and there is Coulombic repulsion between MO<sub>2</sub> layers, Li-ions de/intercalation between MO<sub>2</sub> layers is possible [31].

 $LiCoO_2$  has been widely used as a positive electrode material for 20 years since  $LiCoO_2$  was firstly commercialized in the early 1990s [30]. However, only ~50 % of the theoretical capacity

of LiCoO<sub>2</sub> (274 mAh g<sup>-1</sup>) is available because LiCoO<sub>2</sub> is unstable and the phase transition occurs when more than 50 % of the Li-ions are extracted [32-33]. In addition, concerns regarding cost and environmental problems related to cobalt have driven research to focus on alternative transition metal positive electrodes which are more abundant and environmental friendly [30]. Subsequently other positive electrode material compounds, such as LiNiO<sub>2</sub> and LiMnO<sub>2</sub>, have been developed [30,34]. However, the capacity rapidly decreases as a function of cycles due to crystallographic instability. In the case of LiNiO<sub>2</sub>, Ni<sup>2+</sup> migrates into Li sites which can hinder Li diffusion [30,34]. LiMnO<sub>2</sub> can also be unstable due to Jahn-Teller distortions causing a sliding of the basal planes at higher deintercalation states [35]. These problems have limited the use alternative positive electrodes in a commercial Li-ion battery [35].

# 1.3.3.2 Spinel positive electrode compounds

The LiM<sub>2</sub>O<sub>4</sub> (M=Ti, V, and Mn) compounds have the spinel structure. The oxygen framework of LiM<sub>2</sub>O<sub>4</sub> is the same with that of the layered structure, but 1/4 of M ions are located in the Li layer results in leaving Li vacancies in transition metal layer [30]. These vacancies create empty octahedral sites that share faces with the tetrahedral sites occupied with Li in the Li layer. This three-dimensional (3D) Li diffusion path allows fast de/intercalation rates [36].

LiMn<sub>2</sub>O<sub>4</sub> [36] is a common cathode owing to the fact that Mn is abundant and eco-friendly. However, this positive electrode compound has a relatively low theoretical specific capacity (~148 mAh g<sup>-1</sup>) and undergoes capacity fade due to the following reasons [30]: 1) Since the surface of the positive electrode has the higher Li concentration at the beginning of

de/intercalation owing to concentration polarization, it undergoes phase transition from the cubic phase to the tetragonal phase that leads to micro-strain and results in severe capacity loss through Jahn-Teller distortion. The concentration polarization will be described in detail in Chapter 3. 2) Disproportionation of Mn ions during discharge process causes  $2Mn^{3+} = Mn^{2+} + Mn^{4+}$  reaction and  $Mn^{2+}$  is dissolved in the liquid electrolyte. Consequently, the amount of LiMn<sub>2</sub>O<sub>4</sub> active materials is reduced and the dissolved  $Mn^{2+}$  can be electrochemically deposited on a negative electrode which caused the decomposition of the liquid electrolyte by acting as catalyst [30].

# 1.3.3.3 Olivine positive electrode compounds

Iron has been commercially used in various industries due to its low cost, non-toxicity, and abundant characters. Therefore the positive electrode materials including iron have been investigated and the most attractive positive electrode compound is olivine structure of LiFePO<sub>4</sub> which was first developed by Padhi *et al.* in 1997 [37]. It has theoretical capacity of ~170 mAh g<sup>-1</sup> with ~3.4 V operating potential [37]. In addition, it is well known that LiFePO<sub>4</sub> has the high structural and chemical stability related with enhanced cycle performance. However, it suffers low electronic conductivity issue [34], and Nishimura *et al.*[38] experimentally demonstrated Li transport path is one dimensional channel along the (101) which slows Li diffusion. In spite of its drawbacks, it is widely adapted as positive electrode materials today by improving its limitations through nanodimensional processing/effects and/or doping methods [30].

## 1.3.4 Electrolytes

An electrolyte provides Li-ions transport, but not electron transport, between electrodes during charging and discharging (Figure 1-2). Since high ionic conductivity is required to obtain high or adequate power, the role of electrolyte is important in Li-ion batteries. The ideal electrolyte should have: i) high ionic conductivity, ii) high electrochemical and thermal stability, iii) low cost, and iv) negligible electronic conductivity.

# 1.3.4.1 Liquid electrolyte

Since the charge and discharge potential of Li-ion batteries (>3 V) are beyond the decomposition potential of an aqueous electrolyte (~1 V), the aqueous electrolyte cannot be utilized for Li-ion batteries. Hence, electrolytes consisting of inorganic salts (e.g. LiClO<sub>4</sub> and LiPF<sub>6</sub>) dissolved in a mixtures of alkyl carbonates (non-aqueous organic solvents) including ethylene carbonate (EC), dimethyl carbonate (DMC), diethyl carbonate (DEC), propylene carbonate (PC) and ethylmethyl carbonates (EMC) have been developed [39]. Alkyl carbonates are accepted as an electrolyte solvent owing to their stability for the 4 V positive electrodes. Also, the performance of liquid electrolytes significantly depends on the mixed solvent compositions. Since the operating temperature range of Li-ion batteries is between -20 and 60 °C, the electrolyte must be stable with high ionic conductivity in this temperature range. The ionic conductivity is proportional to mobility of solvent and the concentration of mobile ions [39]. In general, EC has a high dielectric constant, but its viscosity and melting point are high (~36.4 °C) [40-42]. On the other hand, linear carbonates such as DMC and DEC have low viscosity but relatively low

dielectric constant compared to EC [40-42]. Additionally, the electrolyte compositions affect the formation of the solid electrolyte interphase (SEI) layer on the surface of graphite electrode during the initial charge cycles due to its thermodynamically instability at 0.4-0.9 V *vs Li*<sup>+</sup>/*Li* [43]. The SEI formation will be discussed in Chapter 3. Due to the above stated reasons, the solvent compositions have been optimized and widely used in Li-ion batteries. However, the flammability of liquid electrolytes causes safety concerns such as fires and explosions [44-46].

# 1.3.4.2 Garnet-like solid electrolyte

Solid-state electrolytes are an alternative solution to mitigate the risk of combustion in Li-ion batteries [47]. Since liquid electrolytes are flammable, solid-state electrolytes have garnered significant attention as a next generation electrolyte due to 1) non-flammability, 2) possible simplified cell fabrication, 3) reduced packaging mass, and 4) low cost [47]. Therefore, various types of solid-state electrolytes have been investigated [48-50], but few simultaneously meet the selection criteria. To be used as an electrolyte in a Li-ion battery, a solid-state electrolyte should fulfill the following criteria[51]: 1) >0.2 mS cm<sup>-1</sup> at room temperature, 2) negligible electronic conductivity, 3) a wide potential window, 4) stability in air, 5) stability against Li, and 6) low grain boundary resistance. In this respect, Thangadurai *et al.*[52] reported that garnet-type compounds with chemical formulas of Li<sub>5</sub>La<sub>3</sub>M<sub>2</sub>O<sub>12</sub> (M=Ta, Nb) are promising candidates as a solid state electrolyte. These materials have high ionic conductivity of 0.04 mS cm<sup>-1</sup> and a wide potential window of >6 V vs Li/Li<sup>+</sup> [52]. In addition to Ta and Nb, Murugan *et al.*[53] discovered a higher conductivity formulation Li<sub>7</sub>La<sub>3</sub>Zr<sub>2</sub>O<sub>12</sub> (LLZO). The LLZO structure is composed of ZrO<sub>6</sub> octahedra and LaO<sub>8</sub> dodecahedra forming a rigid framework with Li located

in two types of site: 24d sites in tetrahedral and 96h sites in distorted octahedral (Figure 1-5). It is reported that LLZO has two polymorphs: cubic and tetragonal, where the former has a higher conductivity compared to the later [54]. In general, LLZO forms a tetragonal crystal structure with an ordered Li network at room temperature [55]. However, this crystal structure of LLZO can be changed by adding super valent dopants [54]. The dopants introduce some disordered Li arrangement by expelling Li-ions, and the disordered Li leads to a change in the crystal structure from tetragonal to cubic [54]. This cubic structure has approximately two orders of magnitude higher ionic conductivity (0.4-1 mS cm<sup>-1</sup>) compared to the tetragonal structure of LLZO (0.16 x 10<sup>-2</sup> mS cm<sup>-1</sup>)[54]. Since the ionic conductivity can be improved by optimizing the lattice parameter, which affects the energy barriers for Li-ion transport, and Li vacancies concentration, the effect of dopants on ionic conductivities of LLZO has been intensively studied [56]. Another important role of a LLZO ceramic electrolyte is to act as a physical barrier between electrodes. To utilize LLZO as an electrolyte and a separator simultaneously, the mechanical properties of LLZO are important. However, there are few studies that characterize the mechanical properties of LLZO ceramic electrolyte.

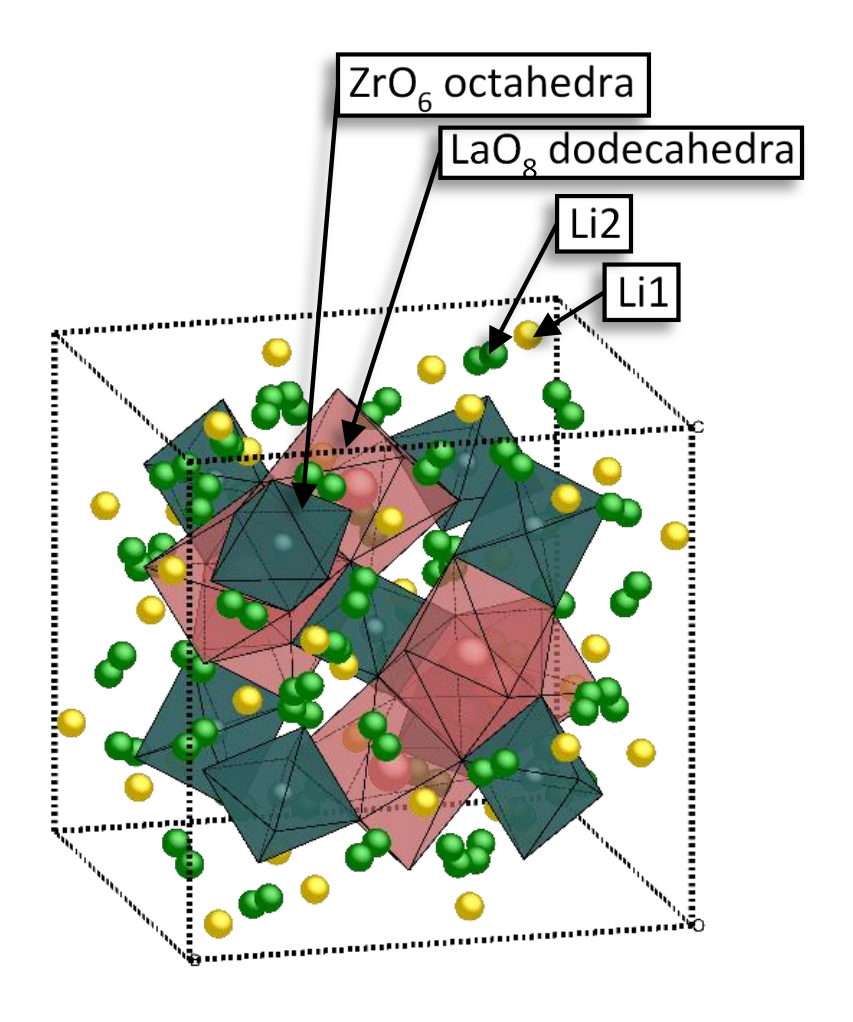


Figure 1-5: The crystal structure of cubic LLZO.

# 1.4 Challenges for electric vehicle systems

As discussed in previous sections, Li-ion batteries are appealing owing to their high energy and power compared to other types of batteries. However, using Li-ion batteries in transportation such as hybrid (HEV), plug-in hybrid electric (PHEV), and battery electric vehicles (BEV) requires higher energy density, faster charging and discharging, longer cycle life, and improved safety [1,9-12].

#### 1.4.1 Power and energy

The United States Advanced Battery Council (USABC) proposed specific requirements for high performance batteries (Table 1-1)[57]. A particular focus is on achieving high power density (600 W L<sup>-1</sup>) without compromising energy density. Energy density represents how much energy can be stored in a given mass and/or volume whereas power density indicates how fast the energy can be released from/to electrodes. Graphite electrodes are typically used in commercial Li-ion batteries as a negative electrode due to its long cycle life, low discharge potential, low cost, and moderate theoretical specific capacity (372 mA g<sup>-1</sup>)[8-9,19-20]. To improve energy density, while using the same electrodes and electrolyte, the challenge turns to the peripheral mass in a battery pack; in other words, minimize peripheral mass and volume to maximize performance.

Electrodes are composed of electro-active storage materials (such as graphite and LiCoO<sub>2</sub> particles), a metal current collector, and a binder (Figure 1-2)[58]. The current collectors offer the homogeneous distribution of electrons into and out of the electrode active materials as well as mechanical support. In general, Cu foil is used for a negative electrode due to its stability against Li at low potentials, and Al foil is used for a positive electrode owing to its low cost, low density, and stability results from the passive Al<sub>2</sub>O<sub>3</sub> layer [59]. A polymeric binder is used to help adhesion between active particles and current collector, and it can also help to maintain mechanical stability during charge and discharge processes [60]. In general, the total specific energy (Wh kg<sup>-1</sup>) of a Li-ion battery can be presented by the following equation [61]:

Total cell (mAh g<sup>-1</sup>) = 
$$\frac{1}{\left(\frac{1}{C_A}\right) + \left(\frac{1}{C_C}\right) + \left(\frac{1}{Q_M}\right)}$$
 (Eq. 1-2)

where  $C_A$  and  $C_C$  are the theoretical specific capacities of the negative and positive electrodes, respectively, and  $I/Q_M$  is the specific mass of other battery components such as current collectors, separator, and electrolyte in g mAh<sup>-1</sup>. Therefore, to increase energy storage per unit mass, the weight fraction of active mass (negative and positive electrode materials) should be maximized and the peripheral mass such as a metal foil current collector, an electrolyte, and a separator should be minimized. One approach is to design thick and low porosity electrodes, to minimize the mass fraction of metal foil current collectors and electrolyte, respectively. Based on the calculations to determine the individual battery component (active and inactive) mass fractions, Figure 1-6 shows that the specific energy is increased by increasing the active electrode mass/loading (thick electrode) and decreasing porosity (dense electrode). However, it is generally known that discharge and charge rates are inversely related to thicker and denser electrodes (Figure 1-7)[19,62]. In addition, less porosity in the electrode also reduced Li-ion transport resulting in low charge and discharge rates [19].

Table 1-1: USABC target of obtaining a high-energy storage and low-cost electric vehicle battery applications [57]. Depth of discharge (DOD), State of charge (SOC).

Parameter (Units) of fully	Minimum goals for long term	Long term goal
burdened system	commercialization	
Power density (W L <sup>-1</sup> )	460	600
Energy density (Wh L <sup>-1</sup> )	230 (C/3 discharge rate)	300 (C/3 discharge rate)
Cycle life (Cycles)	1,000 (80% DOD)	1,000 (80% DOD)
Operating environment (°C)	-40 to 50 (20% performance	-40 to 85
	loss)	
Normal recharge time (h)	6	3 to 6
High rate charge (min)	20-70% SOC in <30 min at 150	40-80% SOC in 15 min
	$W kg^{-1}$ )	
Total pack size (kWh)	40	40

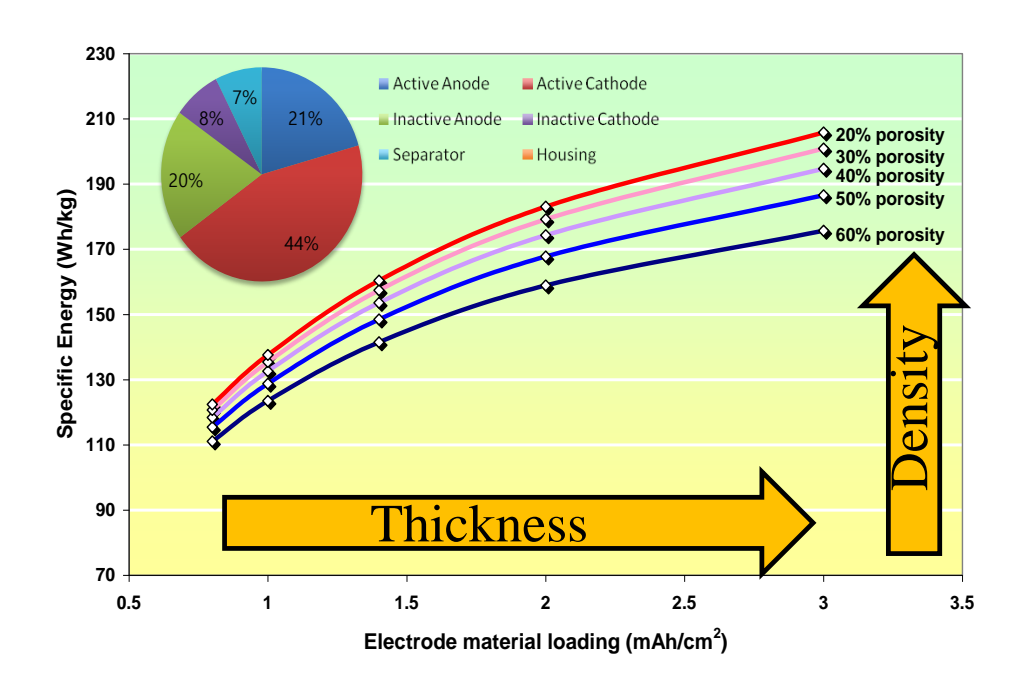


Figure 1-6: Correlation between specific energy, electrode loading, and open porosity assuming LiMO<sub>2</sub>, graphite, 10  $\mu$ m Cu foil, 19  $\mu$ m Al foil, and no packaging.

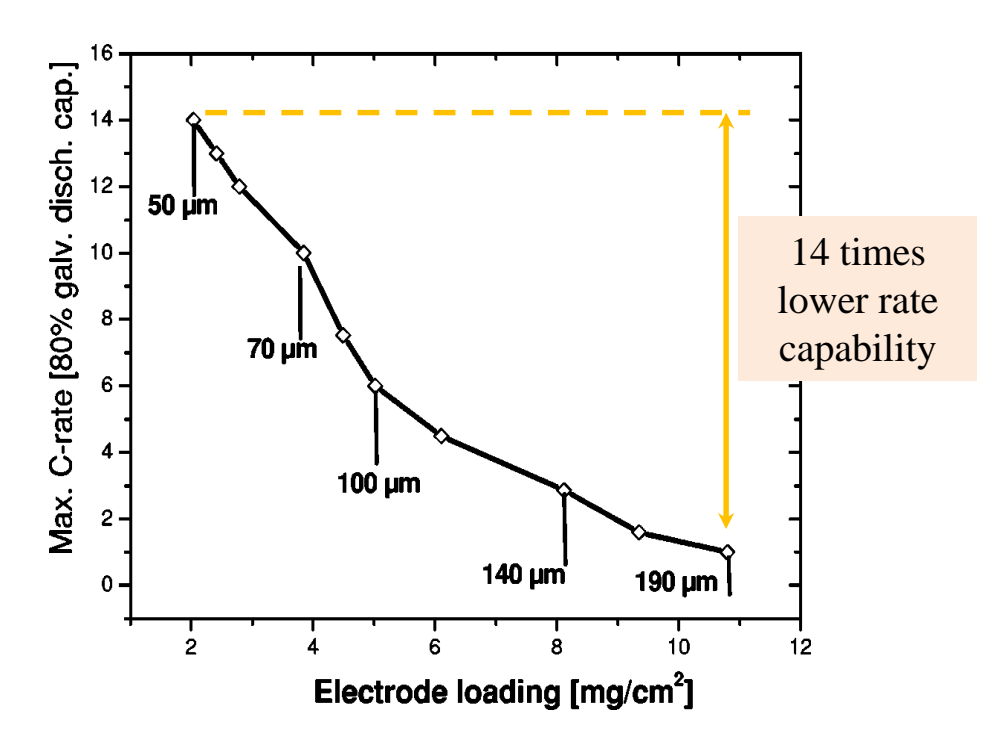


Figure 1-7: Dependence of the power capability of SFG44 graphite electrodes in the electrode loading [19].

## **1.4.2 Safety**

In addition to performance, the safety of Li-ion batteries is also important for vehicle applications [44-46,63-64]. There are two phenomena that can result in Li-ion battery fires. First, improper charging (too fast at <-20 °C) of a Li-ion battery could result in metallic Li deposition on the negative electrode causing Li dendrites to grow and short-circuit to the positive electrode causing instantaneous discharge [44-45]. The instantaneous discharge results in rapid Joule heating to the point that the organic solvent-based electrolyte ignites, causing combustion [1,44,46,64]. Second, the penetration of Li-ion batteries by a metallic object can cause short-circuiting resulting in a phenomenon similar to when Li dendrites cause short-circuiting. The Li-ion battery community has established a standard "nail penetration" test where a nail is driven through a Li-ion battery to cause short circuiting [65]. The nail penetration test is considered to simulate an internal short-circuit in a cell, and this test is important to demonstrate short-circuit is caused by a battery itself or other aspects like a manufacturing defects [65].

During charging, Li-ions diffuse through electrolyte-filled pores in a porous electrode. Since the Li diffusion rate is not uniform and relatively slow in the porous electrodes, the distribution of Li-ions is not uniform under severe charge and/or discharge conditions. This mechanism causes high Li-ion concentration gradients within the electrodes, which is called as concentration polarization, and results in Li dendrite formation and growth. This phenomenon occurs more frequently at fast charge rates due to higher concentration polarization [66]. In addition, a thick and dense electrode (high energy density) exacerbates concentration polarization because of the longer and more tortuous Li-ion diffusion paths [67]. Therefore, concentration polarization can

be mitigated by reducing the diffusion path length. Further, Li dendrite penetration into a positive electrode has to be prevented for safety.

## 1.5 Need for cell design

## 1.5.1 Electrode design approaches

Achieving high power without sacrificing high energy density in Li-ion batteries is most important for electric vehicle applications. Conventionally, microstructural features of an electrode, such as porosity and electrode thickness, were considered as important factors to minimize the cell-level power density limitations [19]. By improving electrode microstructural properties, advances in the Li-ion batteries have been made [14]. Nevertheless, technological challenges still remain such as relatively low power density and safety issues. In general, it was believed that the low power performances are caused by material limitations and slow kinetics [9,14]. In recent years, however, it has been demonstrated that significant power losses, which arise from slow transport of ions, can be improved by cell design and electrode architecture [19,68-70]. To facilitate Li-ion transport in electrodes, Sakamoto et al. [68] designed V<sub>2</sub>O<sub>5</sub> electrodes with hierarchical ordered pores. Due to the highly ordered pores, they obtained high rate performance compared to random porosity electrodes. Zhang et al.[69] also suggested novel electrode architectures by electroplating the positive electrode (MnO<sub>2</sub>) materials in an opal-like porous nickel framework. This group has demonstrated the high power performance of electrodes can be achieved by mesopores network (76 % reversible capacity at 185 C-rate in ~30 nm thick electrode). Bae et al. [70] developed improved kinetics in the positive electrode (LiCoO<sub>2</sub>) by providing homogeneous linear channels. This thick (~220 μm) and dual-scale

porosity electrode was created by a co-extrusion process. Through the increased thickness and by creating linear channels, they obtained both high energy density and power. Although previous works on electrode architecture demonstrated that the high performance of Li-ion batteries can be achieved by reducing internal resistances [68-70], those techniques have not been adopted by the commercial Li-ion battery industry owing to their complex and expensive manufacturing processes that limit scale-ability. In addition, those methods could not precisely control the porosity on electrodes to provide uniform patterning, therefore, uniform current density over relatively large electrode areas. In other words, it is desired that simple and fast patterning process on high energy density (thick) electrode and the ability to control precise patterned porosity for electric vehicle applications. Consequently, a laser patterning process was developed in this research. This technique not only enables a fast and simple patterning process on thick electrodes (high energy), but precisely controls the engineered porosity (uniform current density over a patterned electrode). The laser patterning technique and optimizing electrode design will be discussed in Chapter 4, and the electrochemical performance of patterned electrode will be compared with conventional electrodes in Chapter 5.

#### 1.5.2 Cell design with garnet-like solid electrolyte

As discussed previously, the safety issue is one of the most important requirements for electric vehicle applications. Although the electrode design approach can suppress the metallic Li deposition on the negative electrode by mitigating concentration polarization, it is not the ultimate solution to prevent cell explosion caused by Li dendrite growth. Hence, a new hybrid cell design is proposed in this study (Figure 1-8). Garnet-like ceramic electrolyte may be able to

provide both a physical barrier and Li-ion transport paths between electrodes [71]. Consequently, it is important to characterize and optimize the mechanical properties of the ceramic electrolyte membrane to effectively suppress Li dendrite growth on electrodes during fast charge and/or discharge processes. Since mechanical properties of ceramics are highly sensitive to microstructures, the mechanical properties of LLZO can be optimized by controlling features such as the grain size and relative density. Therefore, the mechanical properties of LLZO ceramic electrolyte were characterized in Chapter 6.

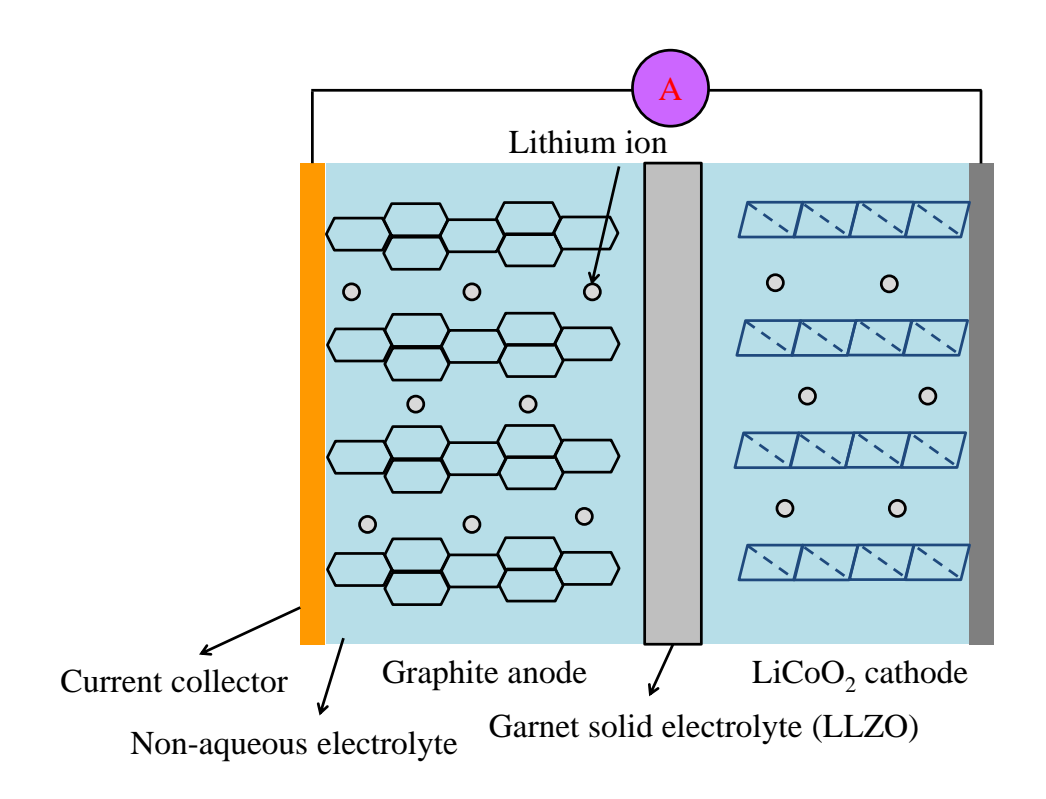


Figure 1-8: Schematic of hybrid cell design composed of graphite negative electrode, LiCoO<sub>2</sub> positive electrode, liquid electrolyte, and LLZO ceramic electrolyte where between electrodes.

## 1.6 Scope of present work

As discussed in section 1.2.2.1, a graphite electrode is one of the most widely used negative electrode materials due to its outstanding properties [9,19-20]. However, the low practical power remains a major disadvantage. It is known that the power capability of graphite electrodes is affected by microstructural properties such as its influence on the thickness, the porosity, the tortuosity, and the electronic conductivity of the graphite electrode network [19]. Hence, this study focuses on determining and understanding the main rate limiting process of a graphite electrode as well as the Li dendrite formation and growth related to safety concerns in Li-ion batteries. Based on the understanding the mechanisms, the power (rate capability) and safety of graphite electrode can be improved using cell design approaches. Furthermore, novel hybrid cell designs including a garnet-like ceramic electrolyte are proposed by optimizing the microstructure of LLZO ceramic electrolyte based on characterization of mechanical properties. The ultimate goal of this study is to enable safe and high performance batteries for electric vehicle applications (Figure 1-9).

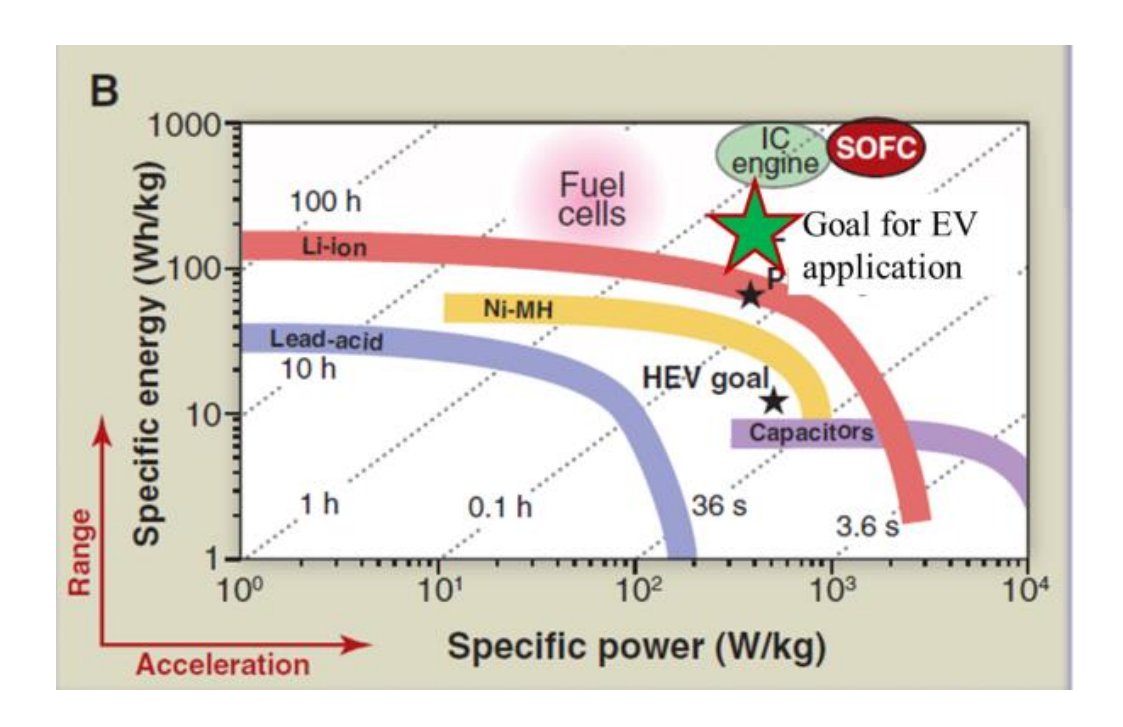


Figure 1-9: Ragone plot for various energy devices [72].

## 2 Experimental methodology

## 2.1 Electrode preparation

In this study, graphite electrodes (TIMREX SFG6: TIMCAL, Bodio, Swizerland) were prepared using a standard tape casting technique (Figure 2-1). The SFG6 graphite was mixed with 10 wt.% polyvinylidene difluoride (PVdF, Alfa Aesar, Johnson Matthey GmbH) binder and N-methyl-2-p yrrolidone solvent (NMP, Alfa Aesar, Johnson Matthey GmbH). The mixture was ball-milled us ing a planetary ball mill (PM 100, Retsch, Germany) to make a homogeneous slurry. An 80 ml a gate jar with 6 agate balls (10 mm diameter, Retsch, Germany) was used. The ball-milling was c onducted for 20 min using 350 rpm. The resulting graphite electrode slurry was cast on 10 µm th ick copper foil (MTI Corporation, USA) using a doctor blade (MTI Corporation, USA), travellin g at a 24 mm s<sup>-1</sup>. The graphite electrode loading (thickness or areal capacity in mAh cm<sup>-2</sup>) was c ontrolled by changing doctor blade height. Three areal loadings were studied: 1.15, 4.0, and 5.5 mAh cm<sup>-2</sup>. The cast electrode sheets were dried using a 250 W infrared light bulb (Philips, Neth erlands) approximately 25 cm from the electrode sheet overnight to evaporate solvent and residu al water. The desired porosity was controlled by calendaring (Mini F100, Durston, UK)(Figure 2-1). Afterwards, the electrode sheet was cut as circle shape using a 532 nm laser described in more detail in section 2.5.1.

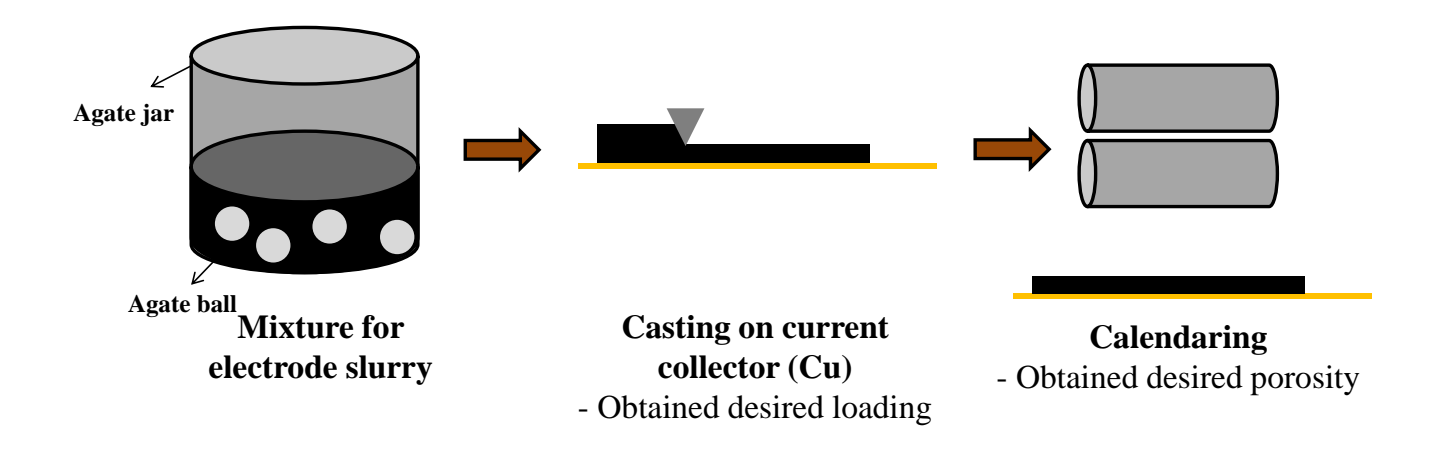


Figure 2-1: Processes flow diagram describing the graphite electrode fabrication process.

## 2.2 Ceramic electrolyte processing

## 2.2.1 Powder preparation

Cubic LLZO, with the nominal composition Li<sub>6.19</sub>Al<sub>0.27</sub>La<sub>3</sub>Zr<sub>2</sub>O<sub>12</sub>, was prepared using a solid-state synthesis method. Li<sub>2</sub>CO<sub>3</sub> (99.9% Alfa Aesar), La(OH)<sub>3</sub> (99.95% Alfa Aesar), ZrO<sub>2</sub> (99.9% Inframat Advanced Materials LLC) and Al<sub>2</sub>O<sub>3</sub> (50 nm Gamma "B" from Mager Scientific Inc.) precursors were mixed for 8 h at 400 rpm using a planetary ball mill (PM 100; Retsch, Germany) with an 500 mL agate jar and 45 agate balls of 10 mm diameter. Al<sub>2</sub>O<sub>3</sub> was added to stabilize the cubic polymorph at room temperature and 10 wt.% excess Li<sub>2</sub>CO<sub>3</sub> was added to compensate for Li loss during calcination. After mixing the precursors, the powder was coldpressed into pellets at 385 MPa in a 1.27 cm diameter stainless steel die. The cold-pressed pellets were placed on LLZO powder (mother powder) to prevent a reaction with the Al<sub>2</sub>O<sub>3</sub> crucible and then calcined at 1000 °C for 4 h in air. The heating rate was 100 °C per h. After calcination, the pellets were manually crushed with a agate mortar and pestle followed by

planetary ball milling for 15 min at 350 rpm using the same agate milling media described above.

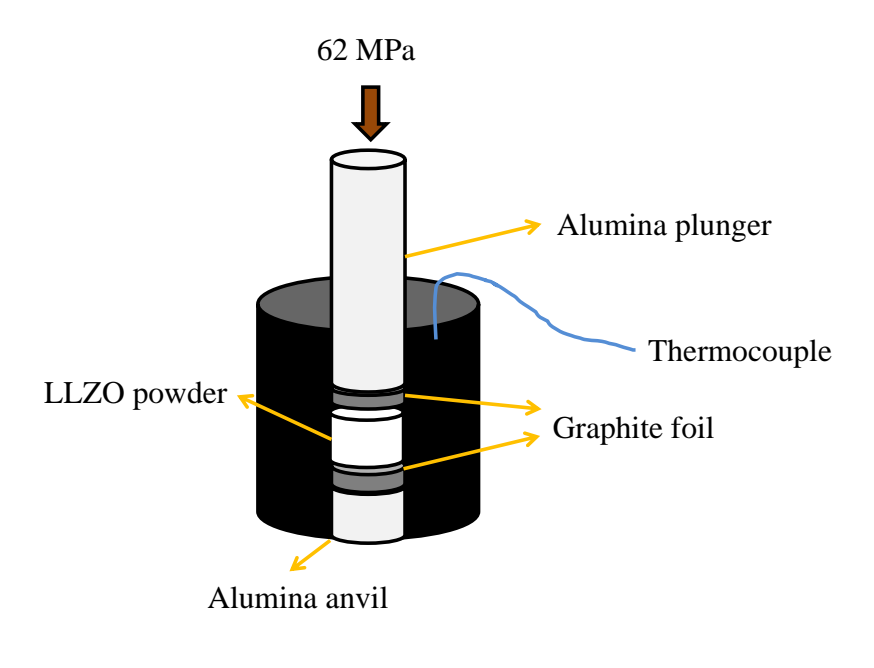
## 2.2.2 Consolidation

The LLZO powders were hot-pressed at 1050 °C under a constant pressure of 62 MPa using rapid induction hot-pressing (RIHP) in flowing argon, as described previously (Figure 2-2)[56,73]. The hot-pressing temperature of 1050 °C was selected to maximize density based on previous work [74].

The relative density was controlled by changing the hot-pressing time (30, 60, 90, and 240 min). The cooling rate was about 6 °C per min. After hot-pressing, each pellet was mounted in Crystalbond® wax and sliced into 3 discs using a diamond saw. The discs were ground on sand paper (Black ice; Norton Corporation, USA) from 400 to 1500 grit then polished using 1 and 0.5 µm diamond paste (Diamond polishing compound; LECO Corporation, USA) on a polishing pad (White technotron; LECO Corporation, USA) with a lapping fixture (Model 900; Southbay Technologies, San Clemente, CA) and an oil-based lubricant (Micro diamond compound extender; LECO Corporation, USA). The discs were stored in a glove box (<1 ppm O<sub>2</sub>, <1 ppm H<sub>2</sub>O) before testing to minimize surface contamination [75-76].



(a)



(b)

Figure 2-2: (a) An image of the rapid induction hot-pressing. (b) Schematic of the cross-section of a graphite die with LLZO power for hot-press.

#### 2.3 Electrochemical measurement methods

#### 2.3.1 Galvanostatic rate mapping test

Galvanostatic rate mapping tests measure the change in electrochemical potential during charging and discharging under uniform current density. The theoretical capacity of a Li-ion battery is determined by the mass of electrochemically active materials:

$$C_T = xF \qquad (Eq. \ 2-1)$$

where  $C_T$  is theoretical capacity, x is the electronic charge passed, and F is Faraday's constant. The C-rate is defined as the current to the charge or discharge capacity in 1 h. The xC-rate indicates that the current chosen will charge or discharge the system in 1/x h.

In the present study, the Galvanostatic rate mapping test was conducted using Swagelok®-type cells (perfluoroalkoxy, Swagelok®, USA)(Figure 2-3a). The Swagelok®-type cell boreholes were machined with a 12.827 mm diameter reamer to allow for the insertion of 12.70 mm diameter stainless 304 stepped pins. For the rate mapping tests, half-cell was constructed consisting of a 3/8 inch graphite electrode as the working electrode, 25 µm thick Celgard® 2400 (Celgard®, USA) separator, 0.75 mm thick Li counter electrode (Alfa Aesar, Johnson Matthey GmbH), and 1.0 M LiPF<sub>6</sub> in ethylene carbonate/propylene carbonate/ethyl-methyl carbonate (EC/PC/EMC, 2:1:7, in vol.%) electrolyte (Soulbrain, Korea)(Figure 2-3b). It is well known that SEI layer is strongly influenced by components of electrolyte [40-41,77-78]. EC is an essential component and widely used as a solvent of organic electrolyte, because it forms a stable SEI film on graphite electrodes [40-42]. However, due to its high melting point (~36.4 °C), poor miscibility with other carbonates, and high viscosity, EC can crystallize out in the liquid

electrolyte at low temperature [42]. To mitigate the crystallization at low temperature, PC was added due to its low melting point (-48.8 °C) and good miscibility with EC [41-42]. EMC, which has low viscosity, was mixed with EC to reduce viscosity and improve ionic conductivity [41]. Since Celgard® 2400 is relatively thin (~25  $\mu$ m), to prevent Li electrode from flowing around the edges of the separator and causing short-circuit, a stainless 304 stepped pin was designed and implemented (Figure 2-3b). The depth of the stepped region was 0.001 inches. To assure the Li surface was clean, Li ribbon was scraped with a stainless steel tool in the glovebox before cell assembly. To assure electrolyte permeation, the Celgard® 2400 separators were soaked in the electrolyte overnight. To assure consistent cell impedance, 45 N of force was applied to the cell, confirmed by a force gage (PS100, Imada, USA). The cell fabrication was conducted in an argon-filled glove box (<1 ppm  $O_2$ , <1 ppm  $H_2O$ ) to prevent moisture and air contamination.



(a)

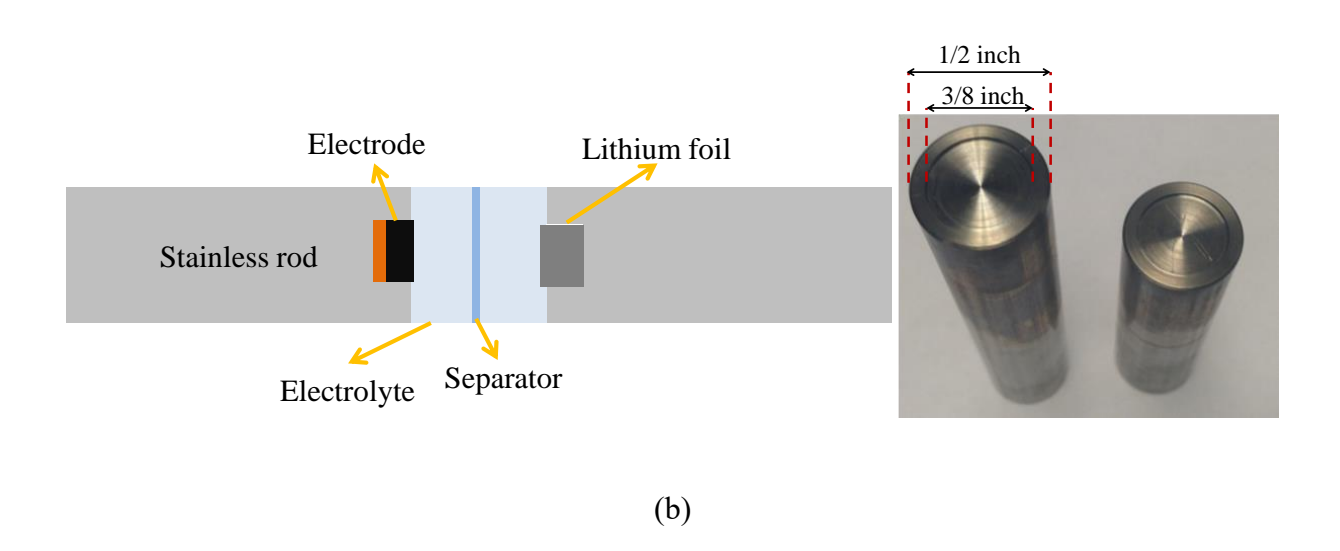


Figure 2-3: (a) An image of a Swagelok® cell with 1/2 inch diameter stainless steel 304 pins. (b) Schematic and the image of stepped stainless steel 304 pins (Outer diameter: 1/2 inch, inner diameter: 3/8 inch), and (c) Swagelok® cell under pressure (45 N) by a force gage.

Figure 2-3 (cont'd).



(c)

Galvanostatic rate mapping tests was conducted using a potentiostat (VMP300, Bio-Logic, Knoxville, TN) at room temperature. All the potential values reported are hereafter referenced to Li/Li<sup>+</sup>. Prior to the rate mapping test, preconditioning cycles were conducted to form a stable SEI layer. The preconditioning cycles were conducted for 3 cycles at 1/5 C-rate for 1.15 mA cm<sup>-1</sup> <sup>2</sup> and 1/10 C-rate for 4 and 5.5 mAh cm<sup>-2</sup> loadings of electrodes, respectively. In addition, since the SEI typically forms between the as-assembled open circuit voltage (~3) and 0.24 V, the first intercalation was conducted at 1/20 C-rate until 0.24 V [43]. The cycling potential window was fixed between 0 and 0.75 V. The SEI layer inhibits further electrolyte decomposition by blocking the electron transport through it while allowing Li-ions to pass through it during rate More detailed discussion about the SEI is discussed in Chapter 3. preconditioning, intercalation was carried out at 1/5, 1/3, 1/2, 1, 2, 3, 5, and 10 C-rates. To limit kinetic effects during Li extraction, deintercalation was conducted at 1/5 C-rate after each intercalation half cycle. To confirm that capacity decline with increasing intercalation C-rate was not a result of irreversible capacity loss, the last de/intercalation cycles were conducted at a relatively slow C-rate (1/5 C-rate). Four identical cells were cycled for each electrode loading. The results of these experiments are discussed in Chapter 5.

## 2.3.2 Intentional overcharge test

As was discussed, metallic Li deposition and Li dendrite growth can cause cell explosion. The intentional overcharge test simulates over charging at high charge rate where metallic Li deposition and Li dendrite growth occurs. In this work, intentional overcharging was conducted on 5.5 mAh cm<sup>-2</sup> with 37 % porosity conventional SFG6 electrodes. The electrodes were

charged at 1 C-rate for 1 h after 10 cycles rate mapping at 1 C-rate. Subsequently, cells were dissembled in an argon-filled glove box. The intercalated electrodes were examined using optical microscope in the glovebox. During this test, the current and potential were controlled and measured by a VMP 300 (Bio-Logic®, Knoxville, TN). The results of this test are discussed in Chapter 3.

## 2.3.3 Galvanostatic intermittent titration technique (GITT)

The GITT method [79] is used to determine the diffusion coefficient ( $D_{Li}$ ) in electrode active materials. This technique applies a series of current-pulses, each followed by a relaxation period for 4 h. During cycling, Li-ions are inserted or extracted into or from active particles, respectively. Thus, the concentration of the particle surface changes and creates a concentration gradient within each active particle. After current is removed, the Li distribution of each particle is homogenized by solid-state Li diffusion. During this process, the cell potential changes with time. Based on the potential vs time profile after current is removed, the Li diffusion coefficient can be determined (Figure 2-4). The Li diffusion coefficient can be calculated by [79]

$$D_{Li} = \frac{4}{\pi} \left(\frac{iV_M}{Z_A FS}\right)^2 \left(\frac{\frac{dE}{d\delta}}{\left(\frac{\Delta E}{d\sqrt{t}}\right)}\right)^2 \qquad (Eq. 2-2)$$

where I is current (A),  $V_M$  is molar volume of the electrode (cm<sup>3</sup>/mol),  $Z_A$  is charge number, F is Faraday's constant (96,485 C mol<sup>-1</sup>), S is electrode/ electrolyte contact area (cm<sup>2</sup>),  $dE/d\delta$  is the slope of the coulometric titration curve found by plotting the steady state potential (V),  $dE/d\sqrt{t}$  is

the slope of the linearized plot of the potential (V) during the current pulse of duration (s),  $m_B$  is weight of the electrode, and  $M_B$  is molar weight of the electrode.

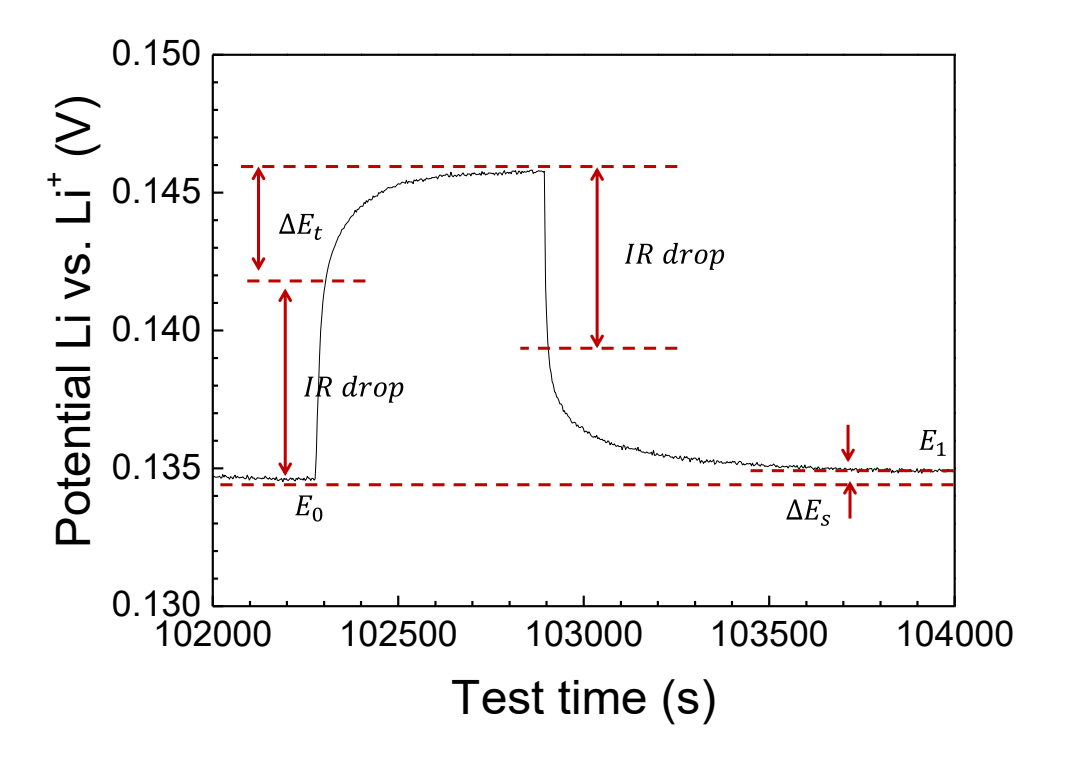


Figure 2-4: Typical GITT plot.

The GITT measurement was employed to determine the Li-ion diffusion coefficient in SFG6 grade graphite electrode in this study. For the GITT test, the relatively thin and high porosity SFG6 graphite electrode loading 1.2 mAh cm<sup>-2</sup> with 63 % porosity was selected such that the solid-state diffusion of Li is the primary source of polarization. Before the GITT test, the half cells (Figure 2-3b) were cycled 3 times at the 1/5 C-rate according to the preconditioning

protocol described above and then fully intercalated. A relaxation period for 10 h was used to allow Li to reach a uniform composition within each graphite particle. The current density (54 μA/cm²) was applied for 10 min followed by 4 h of relaxation time or less than 0.2 mV h<sup>-1</sup> potential change rate. This test was conducted until the cell was fully deintercalated. A VMP 300 potentiostat (Bio-Logic®, Knoxville, TN) was used to control the current and measure the potential. The specific surface area of the electrode is determined by Brunauer–Emmett–Teller (BET) method using the same porosity SFG6 graphite electrode. The Li diffusivity is calculated by *Eq.* 2-2. The experimental results are discussed in Chapter 5.

## 2.3.3.1 Polarization interrupt test

To characterize liquid-phase mass transport in porous electrodes and separators, Thorat *et al.*[80] proposed a polarization interrupt technique based on the GITT method. To characterize macroscopic transport properties, this method uses a symmetric cell (Figure 2-5) where a constant current is applied to produce a concentration gradient. The current is then stopped and the potential change is monitored as a function of time. Under current, ions (Li<sup>+</sup> and PF<sub>6</sub>) are not uniformly distributed, thus when the current is stopped, the ions re-organize, through diffusion, to return to a random or homogeneous distribution. The time required to re-distribute the ions is analyzed to determine macroscopic transport parameters such as tortuosity and the Brugemann coefficient.

For this study, the polarization interrupt tests were carried out on free standing electrodes between 2 layers of separator (Celgard® 2400) as shown in Figure 2.5. A constant current (0.5

mA cm<sup>-2</sup>) was applied for 2 min to create a concentration gradient, followed by a 10 min rest period, then passing current in the reverse direction. This result is discussed in Chapter 5.

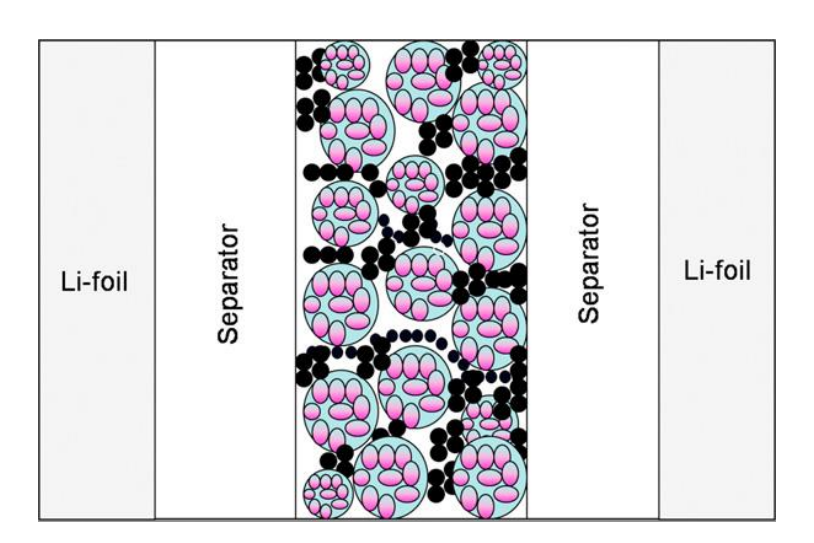


Figure 2-5: Schematic of a symmetric cell for a free-standing electrode [80].

## 2.3.4 Electrochemical impedance spectroscopy (EIS)

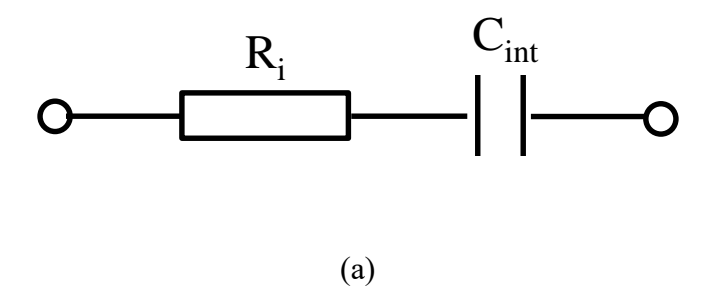
EIS measures the impedance of an electrochemical system over wide range of frequency based on the application of a sinusoidal alternating potential across an electrochemical system [81].

$$V(t) = V_m \times sin(\omega t)$$
 (Eq. 2-3)  
 $\omega = 2\pi v$  (Eq. 2-4)

where V(t) is alternating potential,  $V_M$  is the maximum potential,  $\omega$  is angular frequency, v is frequency, and t is time. The current response to an alternating potential difference, which is characterized by EIS technique, has the same frequency but phase difference  $(\theta)$  as follow

$$I(t) = I_M \times sin(\omega t - \theta)$$
 (Eq. 2-5)

where I(t) is current response to V(t),  $I_M$  is the maximum current. The frequency-dependent impedance is defined by the ratio between the alternating potential and the current response (Ohm's law). Typically, an electrical equivalent circuit is built from components such as resistors, capacitors, and inductors to describe the electrochemical behavior of the electrochemical system. The values of resistance and capacitance can be obtained through modeling of the EIS data using an equivalent circuit. Figure 2-6a shows a typical equivalent circuit for a solid electrolyte [81]. The solid electrolyte is placed between unreactive electrodes (blocking electrodes) to measure ionic conductivity (Figure 2-6b). The general assumption is electrical current within the solid electrolyte is transported only by ionic species, but they are blocked at the interface between electrolyte and blocking electrode unlike the transport of electrons [81-82]. Since the excess ionic charge at the ionically blocking interface is balanced by excess electronic charge in the nearby blocking electrode, the interface between a solid electrolyte and blocking electrode can represent as a parallel plate capacitor. Thus, the equivalent circuit of the solid electrolyte can be designed including a finite resistance  $(R_i)$ , which is caused by the charge passed from one electrolyte-electrode interface to the other. Utilizing a numerical model for the equivalent plot, the electrolyte properties are characterized. Similarly, the Li-ion transport properties in the porous electrode of a Li-ion battery can be characterized by EIS as well. The simple equivalent circuit of the porous electrode and its typical Nyquist plot are shown in Figure 2-7. The Nyquist plot is composed of semi-circle region at high frequency, relating to Li-ion conductivity, the 45° linear slopping line in the intermediate frequency range, relating to semi-infinite Li diffusion (Warburg impedance) in an electrode active material, and a straight tail at low frequencies due to charge saturation in the blocking electrodes (Figure 2-7b).



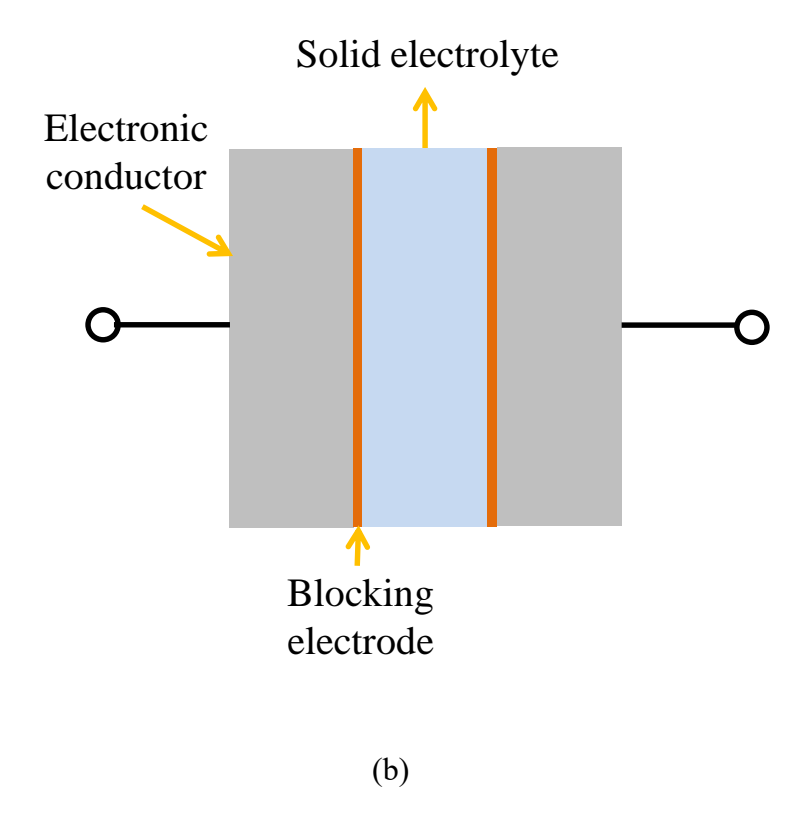
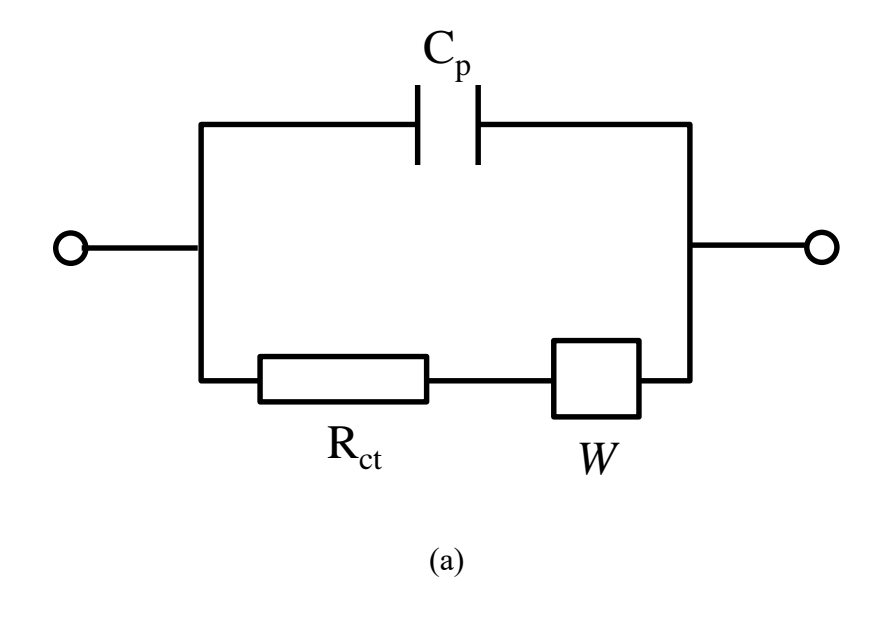


Figure 2-6: Schematics of (a) a typical equivalent circuit for a solid electrolyte and (b) a cell preparation with solid electrolyte between blocking electrodes for EIS.



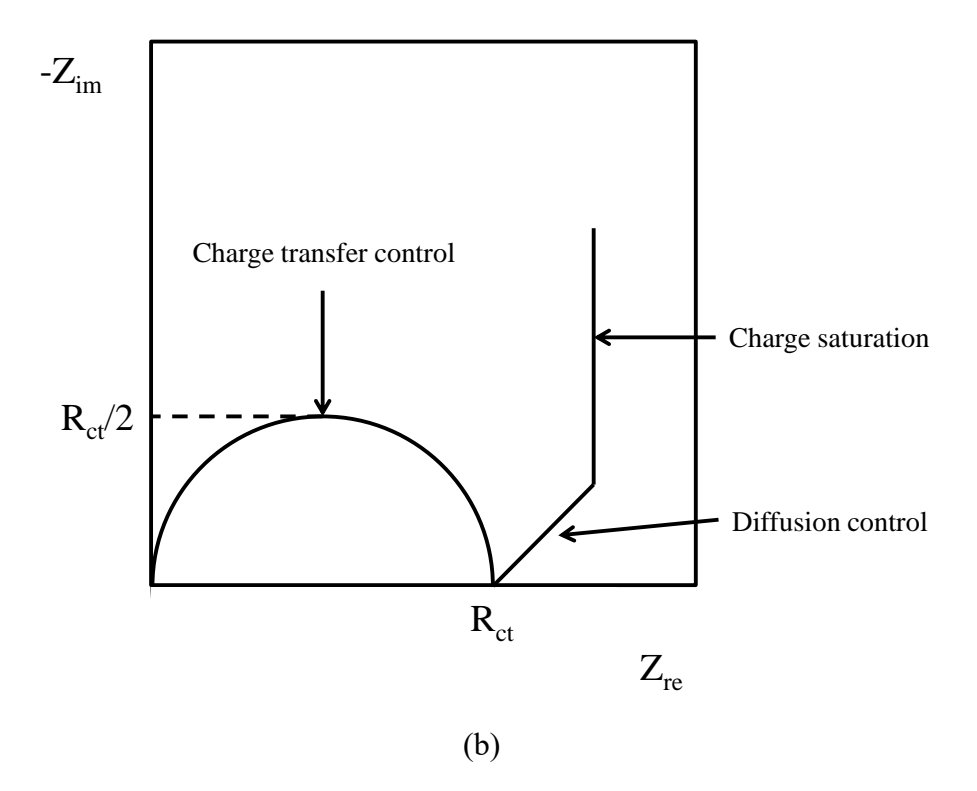


Figure 2-7: Schematics of (a) simple equivalent circuit model and (b) a typical Nyquist behavior for porous electrodes.

In this study, the EIS was performed at 20 °C from 1 Hz to 7 MHz with 100 mV perturbation amplitude (Potentiostat; Bio-Logic, Knoxville, TN, VMP300) to determine the resistance of each component in Li/graphite half-cells in the fully discharged state. The EIS data of the Li/graphite half-cell are discussed in Chapter 5. In addition, the total ionic conductivity of the hot-pressed LLZO samples was determined by the same EIS technique. To measure the ionic conductivity of the LLZO ceramic electrolytes, platinum electrodes were sputter coated on both sides of the hot-pressed discs. This is discussed in Chapter 6.

# 2.3.4.1 Transmission line model (TLM) and electrochemical impedance spectroscopy using symmetric electrode (EIS-SC)

Ogihara *et al.*[83] estimated the resistance of electrolyte-filled pore in a porous electrode by combination of a theory based on the TLM for cylindrical pores and an electrochemical impedance spectroscopy analysis technique using symmetric electrode (EIS-SC) to remove the effects of counter electrode such as Li. TLM has been widely utilized to isolate the individual contributions to cell resistance, and can be expressed by the following equations (*Eq.* 2-6 for non-faradaic, *Eq.* 2-7 for faradaic)[83-85].

$$Z_{\omega} = \sqrt{\frac{R_{ion,L}}{j\omega C_{dl,A} 2\pi r}} \coth \sqrt{R_{ion,L} j\omega C_{dl,A} 2\pi r} L \qquad (Eq. 2-6)$$

$$Z_{\omega} = \sqrt{\frac{R_{ion,L}R_{ct,A}}{(1+j\omega R_{ct,A}C_{dl,A})2\pi r}} coth \sqrt{\frac{R_{ion,L}(1+j\omega R_{ct,A}C_{dl,A})2\pi r}{R_{ct,A}}} L$$
 (Eq. 2-7)

where  $Z_{\omega}$  is the overall impedance,  $\omega$  is angular frequency  $(2\pi f)$ ,  $R_{ion,L}$  is the ionic resistance in the pores per unit pore length, r is pore radius,  $C_{dl,A}$  is electrical double layer capacitance per unit

surface area, and L is unit pore length [83]. Based on these equations, the resistance of electrolyte-filled pores in a porous electrode can be estimated using given values for each parameter. The calculated Nyquist plot behavior is similar to the experimental data (Figure 2-8)[83].

In the present work, the TLM and EIS-SC techniques were conducted to measure the internal resistances of graphite electrodes without the effects of Li electrodes. A symmetric cell was assembled after preconditioning cycles to form a firm SEI passive layer, which was followed by EIS testing. These results are discussed in Chapter 5.

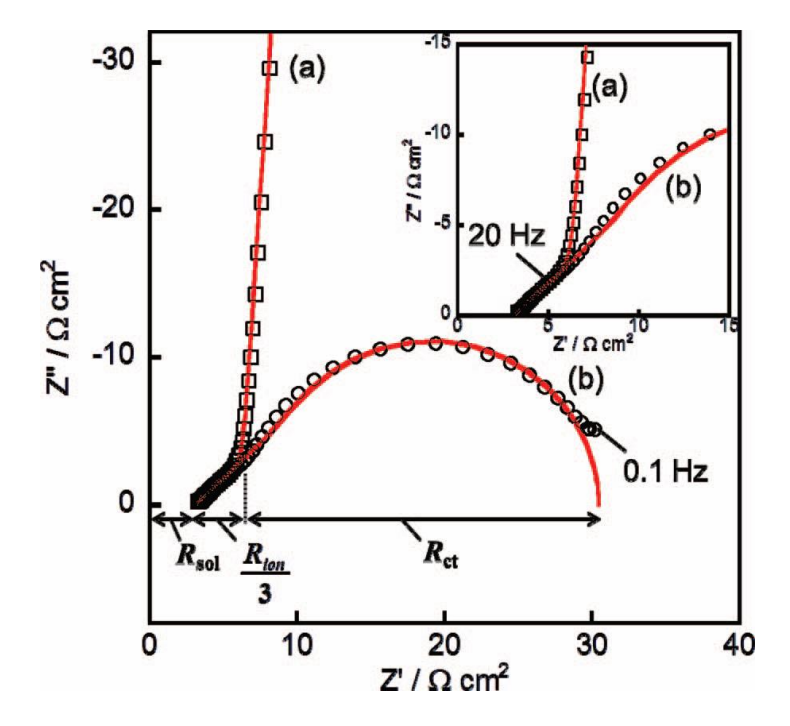


Figure 2-8: Nyquist plots for symmetric cells using two positive electrodes. (a) SOC = 0% (squares) and (b) SOC = 50% (circles). The solid lines are the best-fitted results with the equivalent circuits using Eq. 2-6 and Eq. 2-7 for (a) and (b), respectively [83].

#### 2.4 Mechanical property characterization

#### 2.4.1 Vickers hardness

The Vickers hardness test was developed by Smith *et al.*[86] in 1921. This method measures hardness of materials using micron sized diamond indentors. Hardness is defined as the resistance to plastic deformation from an applied load, and it is determined by measuring a permanent depth of the indentation. This value is related to friction and wear resistance of materials. Vickers hardness values ( $H_{\nu}$ ) are obtained based on the average length of the two diagonal of indentation impression using Eq. 2-8.

$$H_V = \frac{2P\sin(\emptyset/2)}{d^2} = \frac{1.854P}{d^2}$$
 (Eq. 2-8)

where P is applied load,  $\emptyset$  is the angle of the indenter (136°), and d is the length of the diagonal of the Vickers indentation impression.

The indentation technique is also considered as one of the simplest and fastest methods to measure fracture toughness [87]. In brittle materials, the fracture toughness is often a challenge to measure due to a number of specimens required to obtain statistical relevance. For this reason, estimating the fracture toughness by measuring the crack length of indentations has been investigated. Evans *et al.*[88] introduced the first relationship between on a dimensional analysis by experimental work to measure the fracture toughness by the double torsion technique and hardness with a Vickers diamond tip. Since the fracture toughness is ability of a material to resist fracture, the fracture toughness can be estimated by investigating the crack propagation properties such as: the applied load required to create a crack, the crack size, and Young's

modulus. The analytical equations used to estimate the fracture toughness list is shown in Table 2-1.

Table 2-1: Equations for fracture toughness based on Vickers hardness technique. (E is the Young's modulus,  $H_{\nu}$  is the Vickers hardness, c is the crack length, a is the length of half diagonal, and P is the applied load.)

2 <u> </u>	,	
References	$K_{IC}$ Equations	
Evans and Charles [88]	$K_{IC} = 0.0732 \left(\frac{E}{H_V}\right)^{0.4} H_V a^{\frac{1}{2}} \left(\frac{c}{a}\right)^{-\frac{3}{2}}$	(Eq. 2-9)
Lawn <i>et al</i> . [89]	$K_{IC} = 0.028 \left(\frac{E}{H_V}\right)^{0.5} H_V a^{\frac{1}{2}} \left(\frac{c}{a}\right)^{-\frac{3}{2}}$	(Eq. 2-10)
Antis et al. [90]	$K_{IC} = 0.016 \left(\frac{E}{H_V}\right)^{0.5} P(c)^{-\frac{3}{2}}$	(Eq. 2-11)
Bhat [91]	$K_{IC} = 1.59 \times 10^{-5} (E)^{0.4} P^{0.6} a^{-0.7} (\frac{c}{a})^{-1}$	0.36 (Eq. 2-12)

For this work, the  $H_{\nu}$  was determined using a Vickers hardness tester (Vickers/Knoop hardness tester; Mitutoyo Corporation, Japan, HM122 V/K series 810 micro). Before indentation, the Vickers hardness tester was calibrated using a steel hardness block (Vickers hardness test block; Mitutoyo Corporation, Japan, Hardness Test Block HMV 700HV). The Vickers hardness tests were conducted at a load of 0.294 N for an indentation time of 10 s. This load was chosen to minimize microcracking. For each hot-pressed sample, 10 hardness measurements at 150  $\mu$ m spacing were performed. The  $H_{\nu}$  was determined by Eq. 2-8.

The fracture toughness ( $K_{IC}$ ) was estimated using the indentation technique (Vickers indenter). For the samples with relative densities above 95 % the applied load was 0.686 N. For the sample with the lowest relative density of 85 % in this study, the load was increased to 4.9 N to produce measureable crack lengths. In all cases, the dwell time was 10 s. 10 indents were made per sample. Crack lengths were determined from SEM images. The  $K_{IC}$  of the hot-pressed samples was calculated by Eq. 2-11 [90]. The H value is from the  $H_{\nu}$ . For both the hardness and  $K_{IC}$ , the

indentation diagonal and crack length measurements were made immediately after testing to minimize the reaction with ambient air. The radius of the surface crack length was about 2-3 times larger than the half diagonal for all the measurements. The Vickers test is discussed in Chapter 6.

#### 2.4.2 Nano indentation

Nanoindentation was developed to measure the hardness of a sample of limited volume. The Berkovich three-sided pyramidal diamond tip is commonly used in indentation tests due to a sharp point which can precisely control the indentation depth. The face angle of the Berkovich indenter is designed as  $65.27^{\circ}$  to have the projected area-to-depth ratio as the Vickers indenter. Since it is difficult to measure the impression size due to its small size, the size of contact is determined using the known geometry of the indenter. The procedure also allows the Young's modulus of the material to be determined from a measurement of the stiffness of the contact, that is, the rate of change of load and depth. During the unloading stage, there is a little elastic recovery to some extent to its original shape. This initial portion of this elastic unloading is then related to the Young's modulus [92]. The indentation modulus  $(E^*)$  can be derived through the following Eq. 2-13 as function of dP/dh and the area of contact:

$$E^* = \frac{1}{2} \sqrt{\frac{\pi}{A}} \frac{dP}{dh}$$
 (Eq. 2-13)

where A is area of contact, dP is load increment and dh is the increment of the indentation depth of the maximum unloading load. The Young's modulus (E) of the material can be defined in the following relationship:

$$\frac{1}{E^*} = \frac{(1-v^2)}{E} + \frac{(1-v_i^2)}{E_i}$$
 (Eq. 2-14)

where  $E_i$  and  $v_i$  are the Young's modulus and the Poisson's ratio for the nanoindenter, and E and v are the Young's modulus and the Poisson's ratio of the material, respectively.

The nano hardness ( $H_n$ ) and Young's modulus (E) of the hot-pressed discs were determined using a nanoindenter (Nanoindenter; MTS system Corporation, G200) with a Berkovich three-sided pyramidal diamond tip employing a 20 nm radius. The test parameters were  $0.05 \, \text{s}^{-1}$  strain rate, 2 nm harmonic displacement, and a frequency of 45 Hz. The maximum depth limit was 1  $\mu$ m. The average maximum load value used for a total of four samples was  $124.9 \pm 8.3 \, \mu$ N. 10 hardness measurements were taken for each relative density. The Young's modulus was calculated from the load-displacement curve during unloading using the Oliver-Pharr method [93]. Fused silica (Corning 7980; MTS system Corporation, USA) was used as the standard reference material to calibrate the instrument. The nanoindentation is discussed in Chapter 6.

#### 2.5 Other methods

## 2.5.1 Laser patterning

The laser patterning apparatus was custom fabricated by combining a computer numerical control (CNC, Mach3, Newfangled solutions, USA) system, laser light source (IPG Corporation, USA), and optics. A 5 W green fiber laser (532 nm, 1 nm pulse length) focused from 5 mm down to a 20 µm diameter spot size (~1.59 MW cm<sup>-2</sup>) was chosen for electrode ablation. The laser patterning conditions were optimized for each electrode conditions such as loading and porosity. The power and frequency ranged between 80 and 87 % and between 80 and 87 kHz,

respectively. A close-packed hexagonal array of channels was made by synchronizing the CNC with the laser beam. Optimizing the laser patterning process is discussed in Chapter 4.

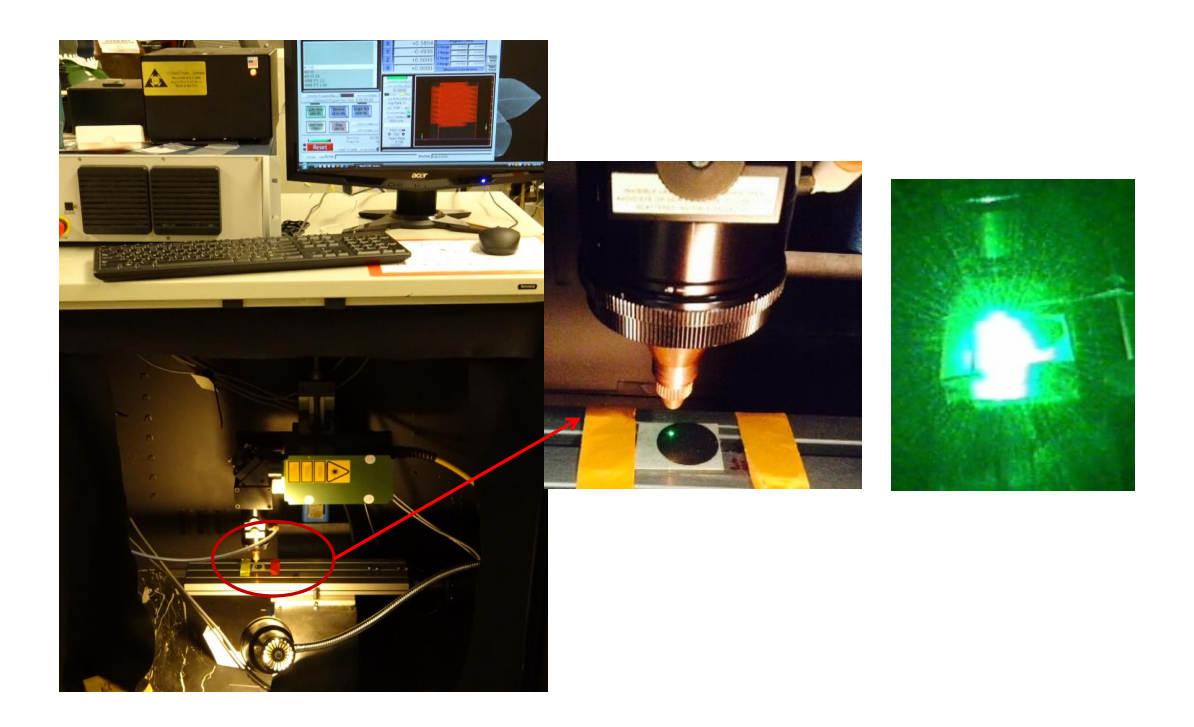


Figure 2-9: The laser patterning equipment fabricated by integrating a computer numerical control (CNC) 3D positioning system with the laser beam.

## 2.5.2 X-ray power diffraction (XRD)

To analyze the phase identification of materials, XRD was used in this work. Based on the Bragg equation (Eq. 2-15), the distance of crystallographic lattice planes can be extracted [94].

$$n\lambda = 2d \sin\theta$$
 (Eq. 2-15)

where n is a positive integer,  $\lambda$  is the wavelength of incident wave, d is the distance between the crystallographic planes and  $\theta$  is the angle of the incident beam. The Bragg relationship is valid

for any lattice structure. This equation is used to create an XRD pattern that plots the angles to find intensity.

In the present work, the phase purity and lattice parameter of the calcined LLZO powders and disks after hot-pressing were determined using XRD (XRD; Bruker, Madison, WI, D8 DaVinci diffractometer equipped with Cu*Ka* X-ray radiation operating at 40 kV and 40 mA) over 10 to 60 degrees 2 theta range and 1.6 seconds per point. The XRD results are discussed in Chapter 6.

## 2.5.3 Scanning electron microscope (SEM)

A SEM is an instrument which permits the observation and characterization of morphology of a material of interest with high resolution and depth of focus. A focused electron beam to scan the surface of the material. The electron beam interacts with electrons at the surface of the material and gives information about surface morphology. In state-of-the-art SEM machines, features in the 20 to 50 Å can be observed.

A SEM technique was utilized to characterize the morphology of electrodes and the microstructure of the hot-pressed LLZO samples in present study. The morphological analysis of graphite electrodes and LLZO membranes is discussed in Chapters 5 and 6, respectively.

#### 2.5.4 Raman

Raman spectroscopy is used to obtain chemical bonding information of materials. This technique involves a impinging a monochromatic light source on a specimen and characterizing

the scattered light. If monochromatic radiation of frequency  $(v_0)$  is allowed to interact with molecules, the scattered radiation contains not only the original frequency  $(v_0)$  but also pairs of new frequencies of the type  $(v_0 \pm v_M)$  [95]. When the surface molecules interact with the incident radiation, either an upward transition  $(v_0 - v_M)$  or a downward transition  $(v_0 + v_M)$  occurs between two molecular energy levels. These are called as Stoke Raman scattering and anti-Stoke Raman scattering shifts, respectively. Plotting the intensity of light shift against frequency results in the Raman spectrum of a sample. The concept of double-resonant Raman scattering has been used to identify  $sp^2$  bonds in carbon [95].

In the present study, the patterned electrodes were characterized by Raman spectroscopy (LabRAM, Horiba Scientific, Japan) to determine if laser ablation changed the graphite chemistry. Raman spectroscopy was conducted on the patterned electrodes using a 532 nm wave length green laser and 2400 lines per mm holographic grating to identify the phase characteristics. The Raman spectroscopy on graphite electrode is discussed in Chapter 5.

## 3 Determining power limiting process and understanding cell failure mechanisms

During the charging and discharging in Li-ion batteries, the charge transport rate is dependent on the battery components, such as electrolyte, separator, electrode active materials, and microstructure of electrodes. Consequently, charge transport rate is not uniform overall cell components. The relatively slow charge transport step can be a rate limiting process. Thus, it is important to characterize each source of resistance in a Li-ion battery cell to determine the rate limiting process. Based on the understanding the primary rate limiting process(es), the rate capability and safety of Li-ion batteries can be improved.

#### 3.1 Intercalation vs deintercalation rate

To determine the rate limiting step during charging *vs* discharging of graphite electrodes, rate mapping of graphite electrodes was conducted (Figure 3-1). To minimize the polarization potential drop, relatively low loading and high porosity (1.15 mAh cm<sup>-2</sup> with 50 % open porosity, respectively) electrodes were used. The percent capacity change as a function of C-rate was determined by measuring the full capacity at relatively low rate (1/5 C-rate). The results show that both intercalation and deintercalation capacity retention as a function of C-rate up to 10 C-rate. Prior to rate mapping at each C-rate, the electrode was fully intercalated or deintercalated using low current (1/5 C-rate)(Figure 3-1). The capacities are reduced as a function of de/intercalation rates in both tests due to polarization. In addition, these rate mapping results show the deintercalation rate capability is much faster than intercalation rate in the graphite electrodes. This capacity difference can be understood by the effects of concentration

polarization. During intercalation, Li-ions are oxidized from the Li counter electrode surface, diffuse through the separator then through the electrolyte-filled pores inside the graphite electrode. In this process, Li-ion transport can be impeded in the tortuous electrolyte-filled diffusion paths resulting in Li-ion accumulation at the electrode face. This results in a Li-ion concentration gradient, which causes concentration polarization. In contrast, during the deintercalation process, Li-ions are homogeneously extracted from each particles then simultaneously transport into counter electrode (Li metal). Consequently, Li-ions are less affected by tortuous Li-ion diffusion paths in the electrolyte-filled graphite electrode during the deintercalation step. This trend is in agreement with previous studies [19]. Therefore, the intercalation (charge) rate capability was intensively studied in the present work.

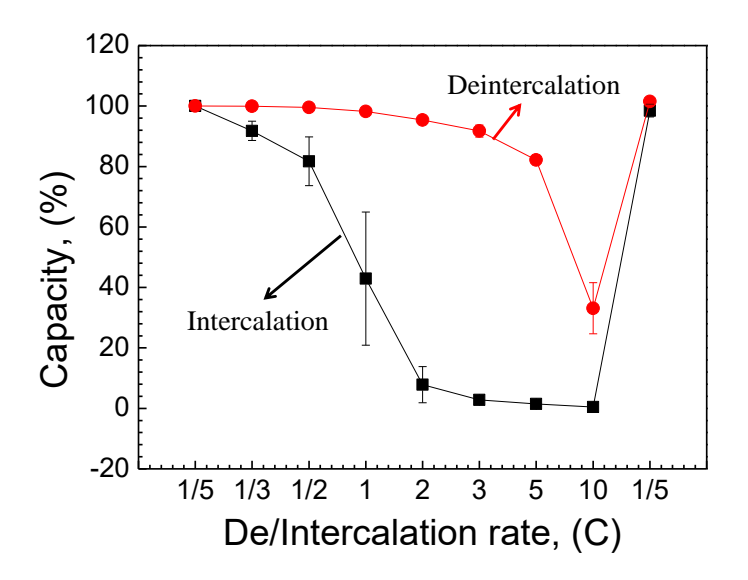
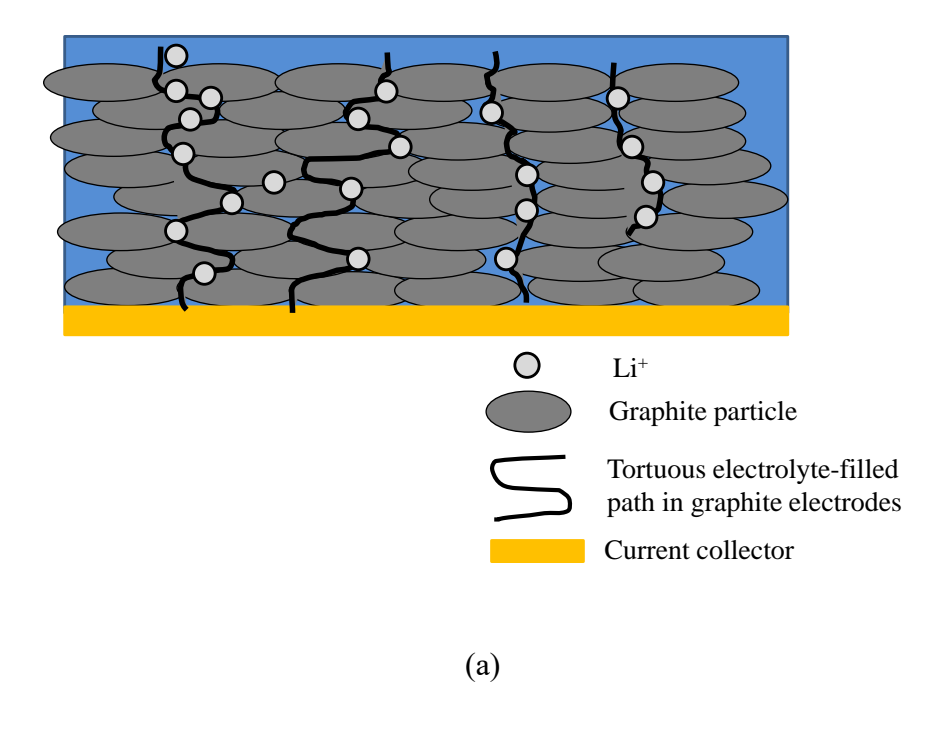


Figure 3-1: Charge and discharge rate mapping of the low loading (1.15 mAh cm<sup>-2</sup> and 50 % total open porosity) graphite electrodes. Black data: Intercalation (charge) rate capability, Red data: deintercalation (discharge) rate capability.

# 3.2 Rate limiting processes

The power (P) of a battery is defined by  $P = V^2/R$ , where V is cell potential and R is internal resistance [96]. Therefore, to maximize power in Li-ion batteries, internal resistances should be minimized [68-70,96-97]. Li-ion batteries involve several transport phenomena, when summed, contribute to a cell's total impedance. In the intercalation process, Li-ions are transported from a Li electrode to a graphite electrode through an electrolyte-permeated separator then diffuse through electrolyte-filled pores in the graphite electrode (Figure 3-2a). At the electrolyteelectrode interface, Li-ions are desolvated and intercalated into a graphite particle (Figure 3-2b)[97-98]. Subsequently, a charge transfer reaction involving Li-ions and electrons occurs, followed by the diffusion of Li-ions within the graphite particles [97-98]. It is difficult to separate the effect(s) of each phenomenon because they occur at similar timescales. In principle, however, the phenomena that contribute to cell impedance consist of: 1) electron injection and extraction at the interface between the current collector and the electro-active materials, 2) ion insertion and extraction at the interfaces between the electrolyte and the electrode including tortuosity, SEI resistances, and charge transfer resistance, and 3) solid state diffusion inside an electro-active material [97].



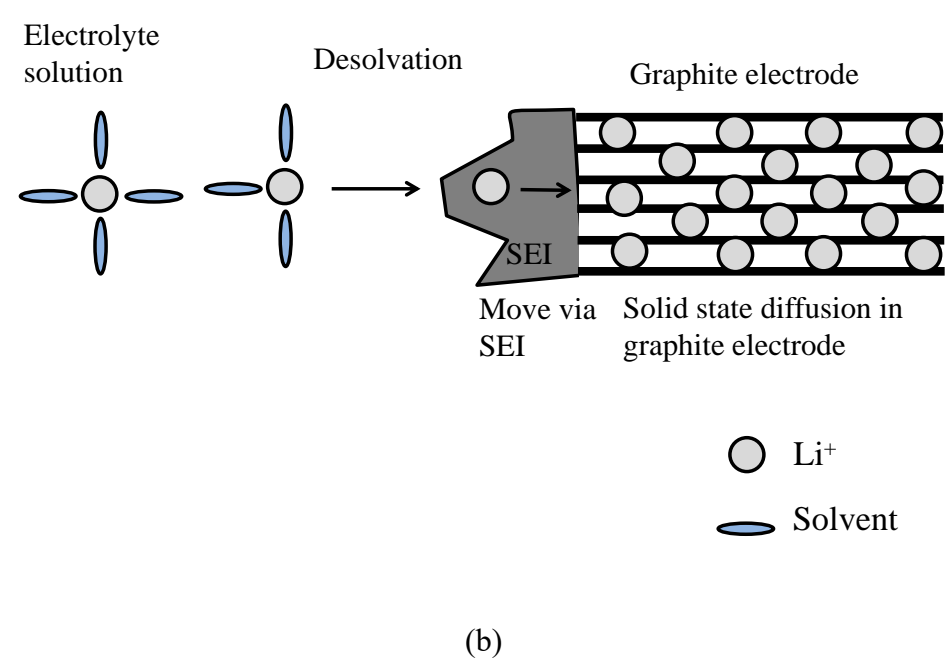


Figure 3-2: (a) Schematic representation of possible Li-ion diffusion paths in electrolyte-filled pores in a graphite electrode, (b) Li intercalation process at a particle scale.

# 3.2.1 Electron injection and extraction resistances

Graphite has intrinsically high electrical conductivity ( $\sim 10^3$  Scm<sup>-1</sup>)[99], thus the resistance induced from electron transport is not the rate limiting factor in the graphite electrode.

# 3.2.2 Ion insertion and extraction resistances at the interface between electrode and electrolyte

# 3.2.2.1 SEI and charge transport resistances

Resistances at the interface between a graphite electrode and an electrolyte are composed of SEI and charge transfer resistance including geometric effects (tortuosity)[83,97]. A SEI layer plays an important role in controlling cycle life, safety, and the irreversible capacity loss in Li-ion batteries [43,77-78]. A SEI is formed on graphite electrode during first few cycles by a reductive decomposition reaction of the electrolyte constituents such as organic solvents and Li salt at 0.4-0.9 V vs. Li<sup>+</sup>/Li [43]. Based on the various spectroscopic analyses two SEI formation mechanisms have been proposed (Figure 3-3)[100]. As shown in Figure 3-3, the first mechanism generates gaseous byproducts by reduction of electrolyte solvents resulting in an SEI that is composed of mainly Li<sub>2</sub>CO<sub>3</sub>. The generation of gaseous byproducts is believed to reduce the mechanical integrity of the SEI compared to a dense SEI [100]. On the other hand, the second mechanism creates less gaseous and insoluble by products. Consequently, the SEI formation includes both mechanisms. Furthermore, a dynamic EIS study demonstrated that the SEI formation processes can be divided in two potential regions. The first step occurs above the

intercalation potential where the reduction of carbonate solvents creates a more porous SEI layer. The second step takes place during intercalation of Li-ions into a graphite electrode. The SEI layer resulting from the second mechanism is more compact and stable due to the formation of a network between organic compounds via the coordination of Li-ions and organic carbonate anions [43]. From these mechanisms, it has been determined that the SEI is composed of many insoluble compounds including Li<sub>2</sub>O, LiF, Li<sub>2</sub>CO<sub>3</sub>, RCO<sub>2</sub>Li, and alkoxides etc., and their Li-ions are originated from electrolyte or electrode [43]. Because Li is irreversibly consumed to form these compounds, the SEI formation causes permanent capacity loss in Li-ion batteries. Unlike the passive films in primary Li cells, the SEI film on a graphite electrode has moderate ionic conductivity, thus this passive film allows Li-ions to transport to/from the graphite particles [43,77-78]. Therefore, once the stable SEI film is formed, this passive film inhibits further decomposition of the electrolyte [43,77-78]. In addition, the SEI layer prevents solvent cointercalation resulted in exfoliation of graphite [24,34]. The exfoliation of graphite is caused by the co-intercalation of solvent along with Li-ions between graphene layers [24,34]. Subsequently, the co-intercalated solvent compounds can split the graphene layer of the graphite, which reduces cycle life.

Figure 3-3: Two mechanisms for the electrochemically induced reduction of carbonate-based solvents. RA is an abbreviation for "radical anion" [100].

Figure 3-4 shows a Nyquist plot of a graphite/Li half-cell measured using EIS. The cell consisted of a SFG6 graphite electrode with a 5.5 mAh cm<sup>-2</sup> loading and 50 % porosity. In general, Nyquist plots for a typical graphite/Li half-cell consists of semicircle at high (1 MHz to 40 kHz) and medium frequency (40 kHz to 10 Hz), and a straight slopping tale (<10 Hz), which is related to semi-infinite Li diffusion in a graphite [78]. Normally, the  $R_b$  is bulk resistance of the electrolyte and cell components;  $R_{SEI}$  and  $C_{SEI}$  represent resistance and capacitance of SEI formed on the surface of the graphite electrode;  $R_p$  represents the charge-transfer resistance and  $C_p$  is the capacitance corresponding to  $R_p$ .  $R_p$  is in series with the Warburg impedance (W); W is related to diffusional effects of Li on the interface between the graphite particles and electrolyte [78]. Figure 3-4 shows the SEI resistance is much smaller (1.3  $\Omega$ ) than the charge transfer resistance (9.1  $\Omega$ ) at SOC 0 %. However, since the SEI resistance is changed by SOC, it is possible that it becomes a power limiting process. However, it is well known that the SEI resistance can be suppressed by engineering the electrolyte for optimal solvent, salt and additive formulation [43,78,100]. For example, vynylene carbonate (VC), which is one of the additives, has a higher reduction potential compared to carbonate-based solvents. Thus VC is reduced prior

to electrochemical reduction of the solvent to form an insoluble SEI. As a result, this layer, which is composed by VC reduction products, suppresses further electrolyte solution and salt reduction, which can cause irreversible capacity and the exfoliation of graphite [101].

On the other hand, faradaic charge transfer resistance is ~7 times higher than the resistance of SEI, thus this resistance can be a rate limiting step (Figure 3-4). However, when charge transfer resistance is measured, it includes the resistance of Li-ions transport within the pores of porous electrode (tortuosity)[83]. Therefore, these resistances should be divided into discrete resistances to identify the exact power limiting process during the intercalation process.

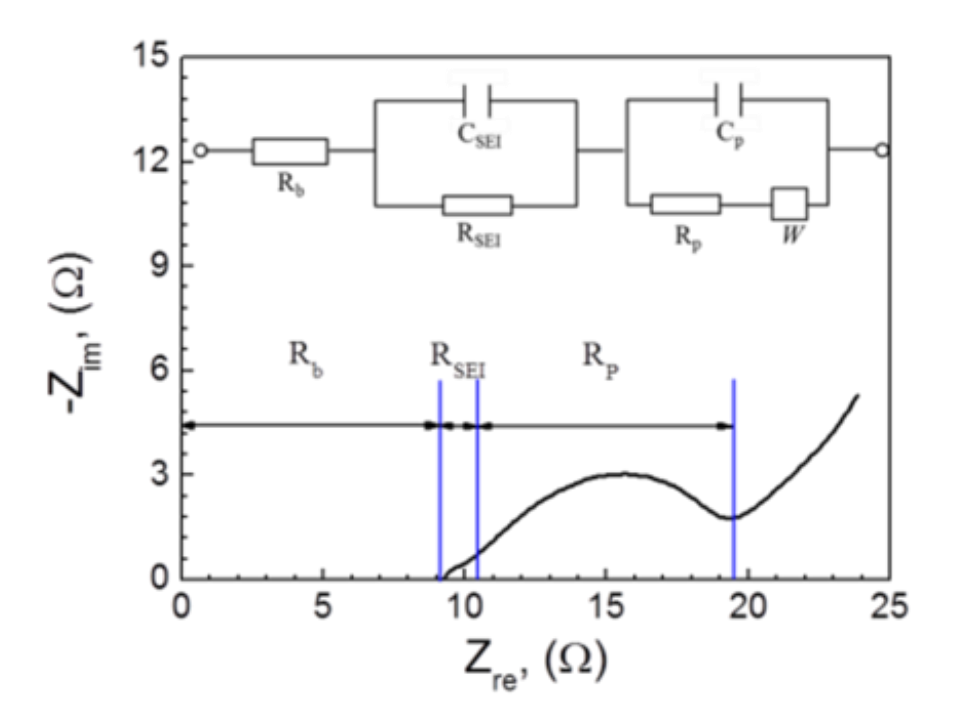


Figure 3-4: Complex impedance plot of Li/graphite half-cell in the delithiated state (SOC=0%).

## 3.2.2.2 Tortuosity

Porous electrodes are typically comprised of interconnected and irregular pores. Since it is difficult to set up the model to measure mass transport properties through electrolyte-filled pore network due to their random nature, the mass transport in the pore network has been interpreted using an effective geometric parameter; tortuosity [80]. Tortuosity is a characteristic of a porous medium through which mass is transported. In general, tortuosity ( $\tau$ ) is geometrically defined as  $\tau = \ell/L$ , where  $\ell$  is the length of actual Li-ions diffusion paths in a porous electrode and L is the electrode thickness [102-105]. It is assumed that the tortuosity is related to the micro structure of a porous electrode, transport properties, and conductivity [80]. Since there are efforts to increase the energy density of Li-ion batteries by making thicker and denser electrodes [19,70], the effects of tortuosity become a more significant parameter to determine the power limiting step. Under normal operation, depleted ion regions in a porous electrode can arise result from non-uniform Li-ions transport due to irregular pore networks [13,68,80]. The regions with high tortuosity can lead to slow net Li-ion flow [106] and the depletion regions can result in IR polarization, which limits rate capability [68,103]. According to Abraham et al. [92], the ohmic loss ( $\Delta E_{ir}$ ) can be described by

$$\Delta E_{ir} = \frac{i\tau^2 l}{\sigma \varepsilon A} \qquad (Eq. 3-1)$$

where  $\sigma$  is the electrolyte conductivity,  $\varepsilon$  is porosity, i is current,  $\tau$  is tortuosity, and i is membrane thickness. This relation shows that the higher tortuosity more significant impacts on cell performance, especially at high current density with thick electrodes. Therefore, it is necessary to mitigate the effects of tortuosity to increase the charge rate of Li-ion batteries. However, there are few methods to characterize tortuosity. Tortuosity is dependent on

complicated microstructural features such as porosity, average particle size, particle sizedistribution, and shape of active materials [68,80]. Due to these complexities, tortuosity is examined by the well-known Bruggeman relationship [80,96,105-106]:

$$\tau = \varepsilon^{1-\alpha} \qquad (Eq. 3-2)$$

where  $\tau$  is the tortuosity,  $\varepsilon$  is amount of open porosity, and  $\alpha$  indicates the Bruggman exponent. Generally, in battery simulations, it is assumed that the electrode is composed of a liquid electrolyte with spherical electrochemically active particles, and a value 1.5 is usually used as a Bruggman exponent ( $\alpha$ ) in battery modeling to quantify tortuosity without experimental demonstration [80,106-107]. Therefore, in the Li-ion battery community, the relevance of these models is debated [80].

To characterize the microstructural properties of an electrode, a 3D model reconstruction of an electrode technique was suggested by Shearing *et al.*[104] using X-ray computed tomography (CT) in 2010. Although, X-ray CT and focused ion beam (FIB) milling techniques have been used in Li-ion battery electrodes, no one had constructed 3D model of an electrode of Li-ion battery [104]. The 3D model reconstruction technique can provide the opportunity to precisely analyze the microstructure of porous electrodes. However, the low resolution issue of X-ray CT limits the accurate 3D model reconstruction of the electrodes. The coarse spatial resolution (~480 nm) of the X-ray tomography technique cannot identify nano-scale pores and particles [108]. In present work, therefore, a 3D model was constructed by scanning electron microscope and focused ion beam (SEM/FIB)(Figure 3-5). By using SEM and FIB gallium ion source, layers of graphite were removed in 150 nm slices and imaged. A total 61 images of the electrode which is 2.8 mAh cm<sup>-2</sup> loading and 40 % open porosity were compiled and MIMICS® software

was used to generate the 3D model of the graphite electrode microstructure. Despite the much higher resolution (~10 nm) of the SEM/FIB technique compared to X-ray tomography [109], the model showed less than half open porosity (~19 %) compared to the experimentally calculated porosity (~40 %). This error could be attributed to the limit of MIMICS® modeling software. The principle of the MIMICS® program is to make the binary color image system (i.e. white region: particle, black region: porosity) by setting a contrast threshold value. Therefore, MIMICS® software can interpret a particle placed on subsurface as a particle on surface (Figure 3-5b). In summary, the 3D model reconstruction method can allow significant access to microstructural information of a porous electrode, but the advanced combination of tomography and computer modeling techniques are necessary to build and analyze an accurate microstructural electrode model.

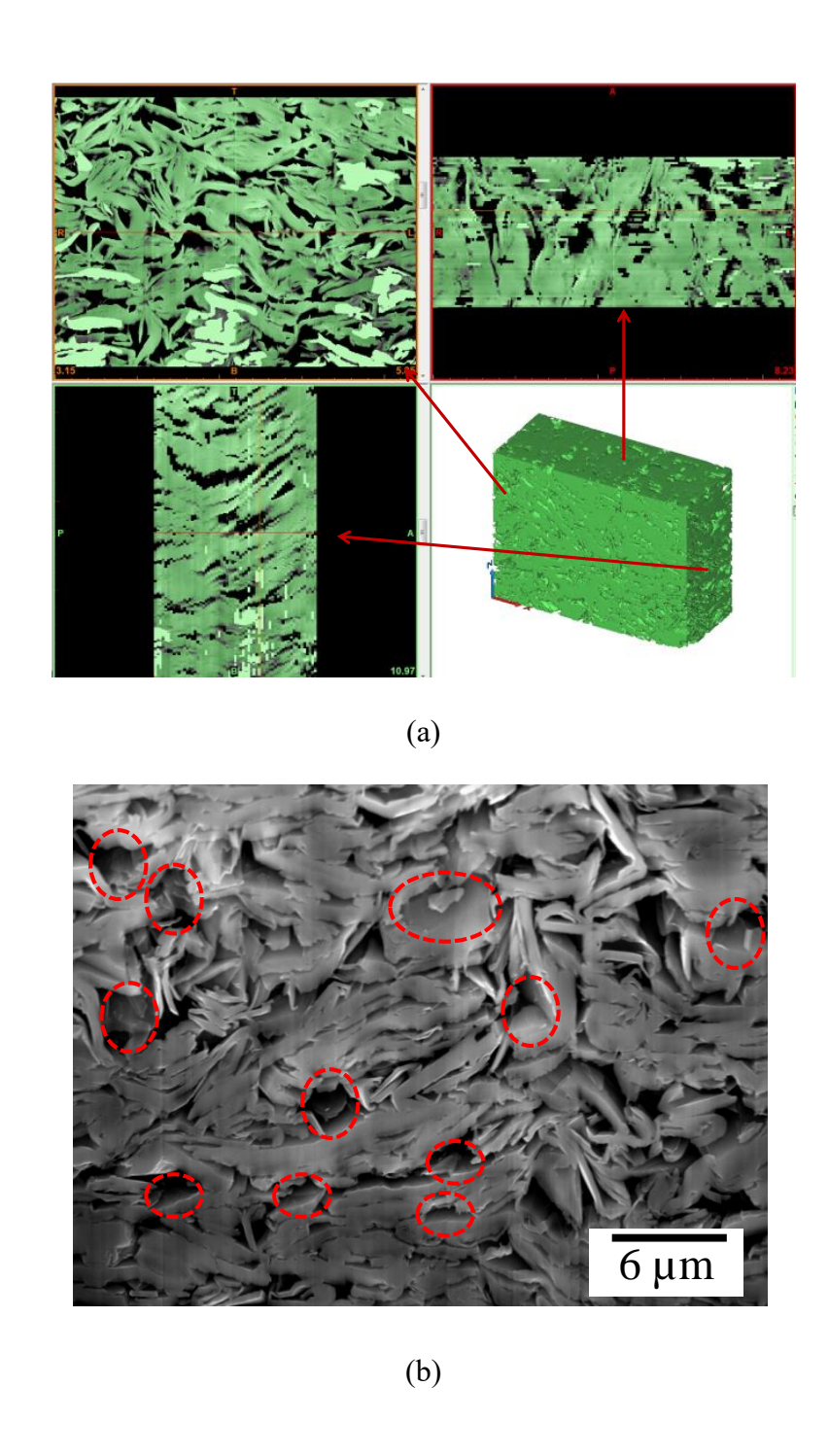


Figure 3-5: (a) 3D reconstruction of a graphite electrode (2.8 mAh cm<sup>-1</sup> and 40 %) by FIB-SEM technique using MIMICS® software. (b) SEM image of a graphite electrode by FIB-SEM.

In 2009 Wheeler *et al.*[80] suggested the experimental method to measure tortuosity of positive electrodes (LiFePO<sub>4</sub> and LiCoO<sub>2</sub>) and porous separators (Celgard® 2400) by polarization interrupt technique. To characterize macroscopic transport properties, this method involves the use of a symmetric cell (Figure 2-5). A constant current is applied to produce a concentration gradient then the current is stopped to analyze the potential change with time, which relates to the transportation of ions recovering to the equilibrium distribution state. Through this method, they found that, although, the Bruggman relationship can estimate the relation between porosity and tortuosity, the real tortuosities of the separator and positive electrode are much higher than the values from the Bruggman relationship with a Bruggman exponent ( $\alpha$ ) = 1.5.

As discussed in Chapter 2, Ogihara *et al.*[83] proposed the combination of TLM model and EIS technique using a symmetric electrodes cell to measure the mass transport resistance of electrolyte-filled pores inside porous electrode. Electrochemical characteristics of porous electrodes are unlike those of bulk properties because the resistance of electrolyte-filled pores becomes larger with smaller pore opening and long pore depth (higher aspect ratio). Thus, TLM has been developed to interpret the each resistance of porous electrodes. Based on the calculation using TLM model (*Eq.* 2-6 and *Eq.* 2-7) and EIS-SC experimental results, Ogihara *et al.*[83] asserted the internal resistances in porous electrodes can be distinguishable, and the resistance of electrolyte-filled pores is important in a thick electrode.

# 3.2.2.3 Solid-state diffusion in graphite electrode

In general, Li-ion diffusion rate is lower (~10<sup>-7</sup> - 10<sup>-10</sup> cm<sup>2</sup> s<sup>-1</sup>) than electron transport inside carbonaceous electro-active materials [110-111]. However, solid-state Li-ion diffusion takes place in a single particle, and the Li-ion diffusion length in active materials can be shortened by reducing the particle diameter [70,112]. Most of intercalation reaction occurs below 0.25 V vs. Li<sup>+</sup>/Li potential in graphite electrodes [43]. Once Li-ions are intercalated into a layer of graphene, the spacing between graphene layers is changed. Due to entropic effects, subsequent Li-ion intercalation occurs at a lower potential and is governed by the Nernst equation and Gibbs Phase Rule [15]. In this case, Li-ions can occupy an ordered array of sites centered in C-C hexagonal rings. This Li staging phenomenon induces the potential plateau region during cycling, and each plateau regions indicates that two phases/stages coexist (Figure 1-3)[15]. What's more important is that the Li diffusion coefficient is affected by the SOC (degree of staging in a graphite electrode). The plot for the Li diffusion coefficient vs SOC in a graphite electrode was obtained by Takami et al.[111], and their diffusion coefficient range was between 10<sup>-7</sup> and 10<sup>-9.5</sup> cm<sup>2</sup> s<sup>-1</sup>. Based on these coefficients, the time required to diffuse through a particle can be estimated by following equation [96],

$$L = \sqrt{Dt} \qquad (Eq. \ 3-3)$$

where L is diffusion length, t is time for Li diffusion, and D is Li diffusion coefficient. Assuming the graphite electrode is spherical, the diffusion time can be expressed as  $t = L^2/D$ . According to Takami *et al.*[111], Li diffusion coefficients (D) are  $10^{-7.5}$  cm<sup>2</sup> s<sup>-1</sup> (SOC 20%),  $10^{-8.5}$  cm<sup>2</sup> s<sup>-1</sup> (SOC 50%), and  $10^{-9.5}$  cm<sup>2</sup> s<sup>-1</sup> (SOC 100%) in a graphite electrode, respectively, and diffusion time can be estimated as a function of SOC (Figure 3-6). Consequently, the time to diffuse from the

outside to the core of a graphite particle should be  $\sim$ 74 s.

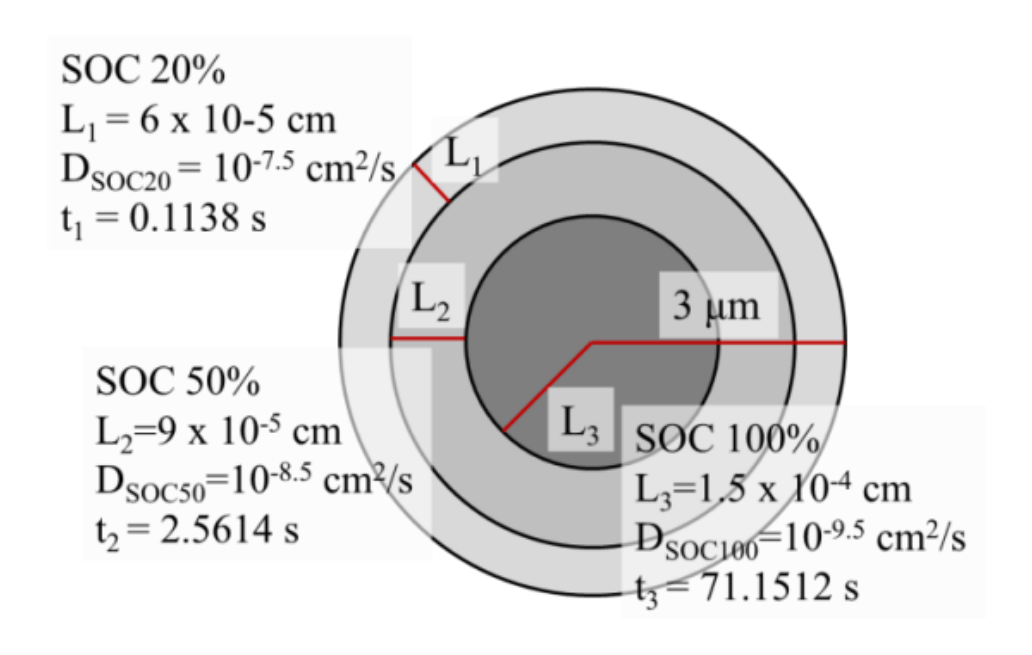


Figure 3-6: Schematic of spherical graphite particle. This figure shows solid state diffusion time according to SOC level. L is diffusion length, t is time for Li diffusion, and D is Li diffusion coefficient.

## 3.3 Understanding cell failure mechanisms

As well as increasing power performance, improved safety is an important requirement for high performance Li-ion batteries [46,65]. The liquid electrolyte is a mixture of organic carbonates including Li salt such as LiPF<sub>6</sub>, LiAsF<sub>6</sub>, LiBF<sub>4</sub>, and LiClO<sub>4</sub> [59]. Since organic electrolytes are flammable [44-46], thermal runaway, that can cause fire and explosion, should be prevented. Improper charging can cause thermal runaway in Li-ion batteries [44-45]. Under high rate charge conditions, Li can deposited on the surface of a graphite electrode due to high

concentration polarization, and grow Li dendrite between electrode/separator interface can penetrate the thin polymer separators (~25 µm) owing to their poor mechanical properties and/or open pores then contact the positive electrode (short-circuit)(Figure 3-7)[8,110]. Consequently, the short-circuiting induces rapid Joule-heating (Figure 3-7)[1,113-114]. Joule heating (Q) can be expressed as below:

$$Q = I^2 Rt \qquad (Eq. 3-4)$$

where I is electric current, R is resistance, and t is time. The temperature of a cell is determined by the heat balance between the amount of heat generated and that dissipated by the cell. Since Joule heating is proportional to square of electric current, it increases the temperature inside a cell when under high current densities. Since the SEI layers on the graphite electrode are decomposed at high temperature (>70 °C), organic solvents used in the electrolyte react with an electrode and Li at ~70 °C [1]. As this exothermic reaction accelerates, the temperature increases and flammable hydrocarbon gases such as ethane and methane are released (Figure 3-7)[1,113-114]. In this stage, the cell can swell due to gas evolution.

$$2Li + C_3H_4O_3$$
 (EC) --->  $Li_2CO_3 + C_2H_4$ 

However, fire does not occur even when the temperature inside the cell is above the ignition point because there is no oxygen [115]. By further increasing the temperature of the cell, the electrolyte reacts with the oxygen gas released by the oxide positive electrode above 150 °C [116], according to the following reactions:

$$\text{Li}_{x}\text{CoO}_{2} \rightarrow \text{xLiCoO}_{2} + 1/3(1-x)\text{Co}_{3}\text{O}_{4} + 1/3(1-x)\text{O}_{2}$$

$$\text{Co}_{3}\text{O}_{4} \rightarrow 3\text{CoO} + 1/2\text{O}_{2}$$

$$\text{CoO} \rightarrow \text{Co} + 1/2\text{O}_{2}$$

Consequently, the Li-ion battery can ignite (Figure 3-7). Since 2006, tens of thousands of mobile phone fires or explosions have occurred due to short circuit and improper charging [1,115].

Therefore, it is important to improve intrinsic safety properties of electrodes such as suppressing the Li deposition and Li dendrite growth into positive electrode direction.

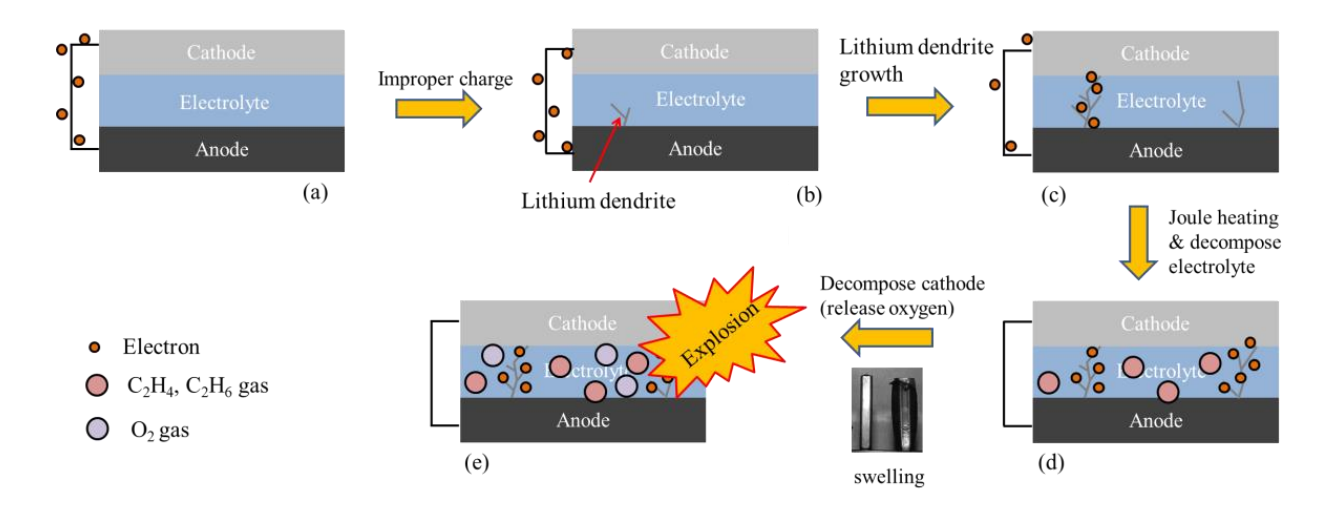
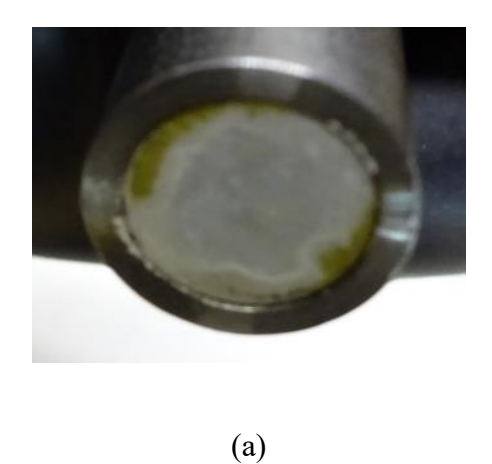
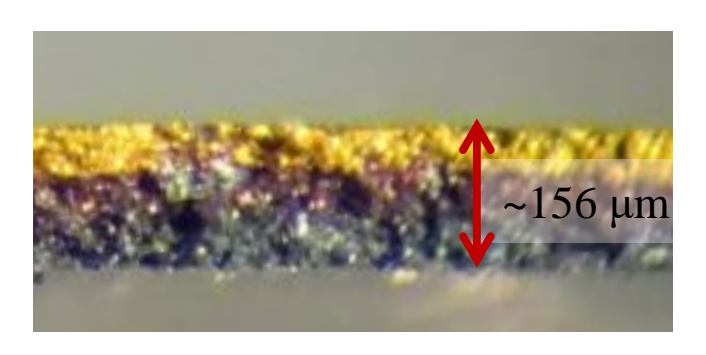


Figure 3-7: A schematic of thermal runaway causes fires by improper charging in Li-ion batteries. (a) normal state battery, (b) Li dendrite formation due to improper charge such as fast charging, (c) short-circuiting by Li dendrite growth and short circuit on the positive electrode causing instantaneous discharge, (d) cell temperature goes up (>70 °C) by Joule heating and electrolyte start to decompose, then flammable hydrocarbon gases are released, (e) Joule heating and exothermic reactions further increase temperature, and the metal oxide positive electrode starts to decompose (>150 °C), then releasing oxygen. These steps can cause cell failure and explosion. (Cell swelling figure [65]).

Figure 3-8 shows the optical microscopic top view and cross-section of SFG6 graphite electrode with 5.5 mAh cm<sup>-2</sup> loading and 50 % porosity after intentional overcharge test at 1 C-rate (2.78 mA cm<sup>-2</sup>) for 1h. After intentional overcharging, Li was deposited on the graphite electrode (Figure 3-8a), and the cross-section image shows color degradation from gold to black (Figure 3-8b). According to Qi *et al.*[117], the different color indicates different SOC. The gold, red, and black color regions indicate: SOC 100 %, SOC 50 %, and less than SOC 20 %, respectively [117]. It has been shown by optical microscopy after charging at low rate (1/5 C-rate)(Figure 3-8c). The SOC was controlled by changing a charging time. Subsequently, it is clear that the Li deposition is caused by concentration polarization at high C-rate, thus the reducing the effects of tortuosity can be one of the solutions to improve the intrinsic safety properties of electrodes by suppressing the Li plating issue.





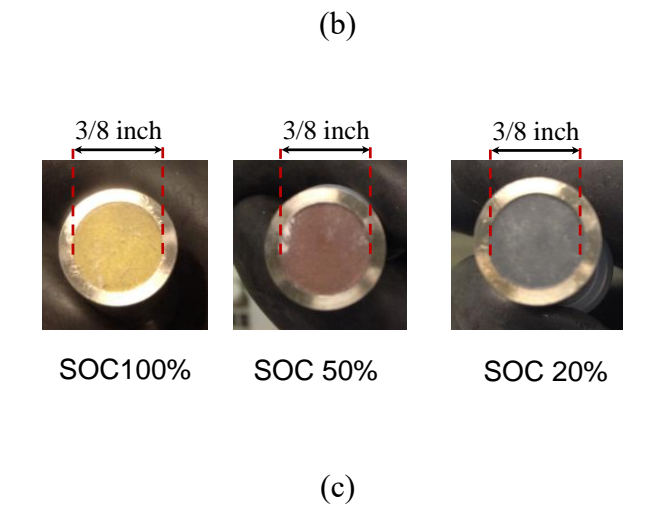


Figure 3-8: (a) Optical image of the surface and (b) fracture surface of over charged SFG6 graphite electrode at 1 C-rate for 1 h, and (c) optical images represent color change in SFG6 graphite electrode by SOC.

## 3.4 Summary

In this Chapter, the rate limiting process and cell failure mechanisms were discussed. Since the intercalation process showed slower rate capability compared to deintercalation, intercalation was determined as a rate limiting step. Based on our estimation of each parameter causing internal resistances during intercalation process, it might be true that a significant factor for rate performance in a Li-ion battery is the resistances at the interface between the electrode and electrolyte. As was discussed, either faradic charge transfer or Li transport through tortuous electrolyte-filled Li-ion diffusion paths in a graphite electrode is more likely to be a rate limiting step. Although it is difficult to distinguish each effect, it is apparent that resistance of Li-ions transportation in pores inside porous active materials increases by making a thicker electrode with less porosity. In addition, Bae et al. [70] asserted Li-ion transportation in active materials is the rate limiting step, not charge transfer resistance at the high current density. Thus, it is important to understand and reduce the effects of tortuosity in an electrode to obtain advanced rate capability with high energy density that can be used in power-critical applications such as electric vehicles. Besides, the reduced tortuosity can improve the intrinsic safety properties of a graphite electrode by reducing the concentration polarization, which is related to Li deposition and growth.

### 4 Laser patterned electrodes

In principle the current Li-ion batteries can achieve higher specific energy than what is found in state-of-the-art technology [118]. The general approach to achieve higher specific energy, while using the same electrode materials, is to maximize electrochemical active mass per unit mass of the cell and battery pack. One specific approach is to increase the mass of electrode material (graphite and metal oxide positive electrodes) per unit area, thus reducing the relative contribution of the metal foil current collectors. The negative electrode, in particular, can benefit significantly from this approach since Cu foil (density = 8.96 g cm<sup>-3</sup>) is used as the metal foil current collector. While this approach is viable in theory, increasing the loading per unit area result in thicker electrodes that hinder rate performance. In other words, from a thermodynamic perspective, Li-ions batteries can deliver higher specific energy, but the approach to employ thicker electrodes is not practical due to kinetic limitations. The goal of this work is to engineer thick electrodes to decouple the relationship between thermodynamics and kinetics, thus enabling higher specific energy Li-ion batteries. As will be discussed, the same approach can also suppress Li dendrite deposition, which arises as a result of kinetic limitations during high rate charging.

## 4.1 Background: three dimensional (3D) electrode designs

The electrode kinetics and mass transport are the most important factors in the performance of electrochemical energy storage technology. The simplest solution for these limitations can be to reduce the electron and ion diffusion distances during the charge and discharge process. The

electron diffusion length can be reduced by reducing the particle size. This can also reduce solid-state Li-ion diffusion distance in the same manner. Regarding ionic transport in the electrolyte, the ion diffusion distance is related to the open porosity and pore size distribution. For example, although electrodes have the same total open porosity, if relatively small pores are present, the small pores can act as "bottlenecks" that govern the net Li-ion transport in the electrode. Therefore, achieving uniform Li-ion transport in the pores of the electrode requires control overall the pore size, morphology and orientation. One strategy is to design and manufacture 3D electrode architectures.

In 2002, Sakamoto et al. [68] fabricated a hierarchically ordered electrode with the inverted opal structure (Figure 4-1a). They used a self-assembled templating method with V<sub>2</sub>O<sub>5</sub> as the positive electrode. Since this structure allows homogeneous Li-ion transport, they observed improved performance compared to conventional V<sub>2</sub>O<sub>5</sub> electrode. Zhang et al. [69] constructed 3D MnO<sub>2</sub> positive electrode by electrodeposition on Ni foam (Figure 4-1b). The Ni foam was prepared by electrodeposition on self-assembled opal template from polystyrene spheres. Prior to electrochemical active material plating on the Ni foam, the porosity of the resulting Ni foam was increased using electro-polishing technique to prevent pore closing by deposition of active materials. Subsequently, a MnO<sub>2</sub> positive electrode with 150-200 nm thick was obtained, and its capacity remained 60 % at 62 C-rate due to its uniform pores. Ji et al.[119] also investigated 3D LiFePO<sub>4</sub> positive electrodes using a template-based technique. Since graphite is not only lightweight compared with metals but also has acceptable electrical conductivity, this group proposed to use a hollow graphite as a current collector for positive electrode instead of metals to reduce mass portion of inactive components in electrodes. The graphite foam current collector was fabricated by depositing graphite on Ni foam followed by the removal of Ni foam as a selective etching technique. LiFePO<sub>4</sub> was then deposited on the hollow graphite foam. These positive electrodes showed high power capabilities delivering capacities of 158 mAh g<sup>-1</sup>, 70 mAh g<sup>-1</sup>, and 36 mAh g<sup>-1</sup> at current densities of 15 mA g<sup>-1</sup>, 1280 mA g<sup>-1</sup>, and 2560 mA g<sup>-1</sup>, respectively. The theoretical capacity of LiFePO<sub>4</sub> is 170 mAh g<sup>-1</sup>. While these are examples that demonstrate the efficacy of 3D structure electrodes, template-based techniques not only require repeating complex energy consuming processes, but it is also difficult to scale-up.

Another example of engineered electrodes involved 3D printing [120] to fabricate 3D electrodes for Zn-Ag alkaline micro-batteries. These electrodes consisted of pillar-like structures that were 40 µm of height and 10 µm in diameter spaced 100 µm apart (Figure 4-1c). This approach achieved a ~60 % increase in areal capacity compared to conventional planar batteries. While these achievements are promising, at present it is not known if 3D printed electrodes can be scaled to meet the capacity and cost constraints for electric vehicle batteries.

Bae *et al.*[70], designed LiCoO<sub>2</sub> electrodes with periodic linear channels made by co-extrusion (Figure 4-1d). A feedrod was used and composed of a mixture of LiCoO<sub>2</sub> powder and polymeric binder (Figure 4-1d). The mixture was consolidated with carbon mandril or rod that would eventually be removed through oxidation to create linear channels. After co-extrusion, the resulting fibers were assembled into arrays, followed by a binder and graphite burnout to form linear channels by heat treatment (Figure 4-1d). 220 μm thick LiCoO<sub>2</sub> positive electrodes were made with pores in ~5 μm diameter range (Figure 4-1d). Since the linear channels permeated the thickness of the electrode, to some degree, the Li-ion diffusion path length was decreased. As a result, the relatively thick LiCoO<sub>2</sub> electrode exhibited ~2 times higher specific capacity at 1 C-rate compared to that of state-of-the-art LiCoO<sub>2</sub> electrodes. Despite this improvement in power

capability, the co-extrusion technique using sacrificial graphite porogen may not be amenable to large-scale fabrication (Figure 4-1d).

Essentially, the aforementioned examples of 3D electrode architectures have demonstrated that the slow kinetics of Li-ion batteries can be improved through electrode design and engineering. However, not all of these examples meet processing criteria such as low cost, rapid fabrication, precise pore position control, and scale up.

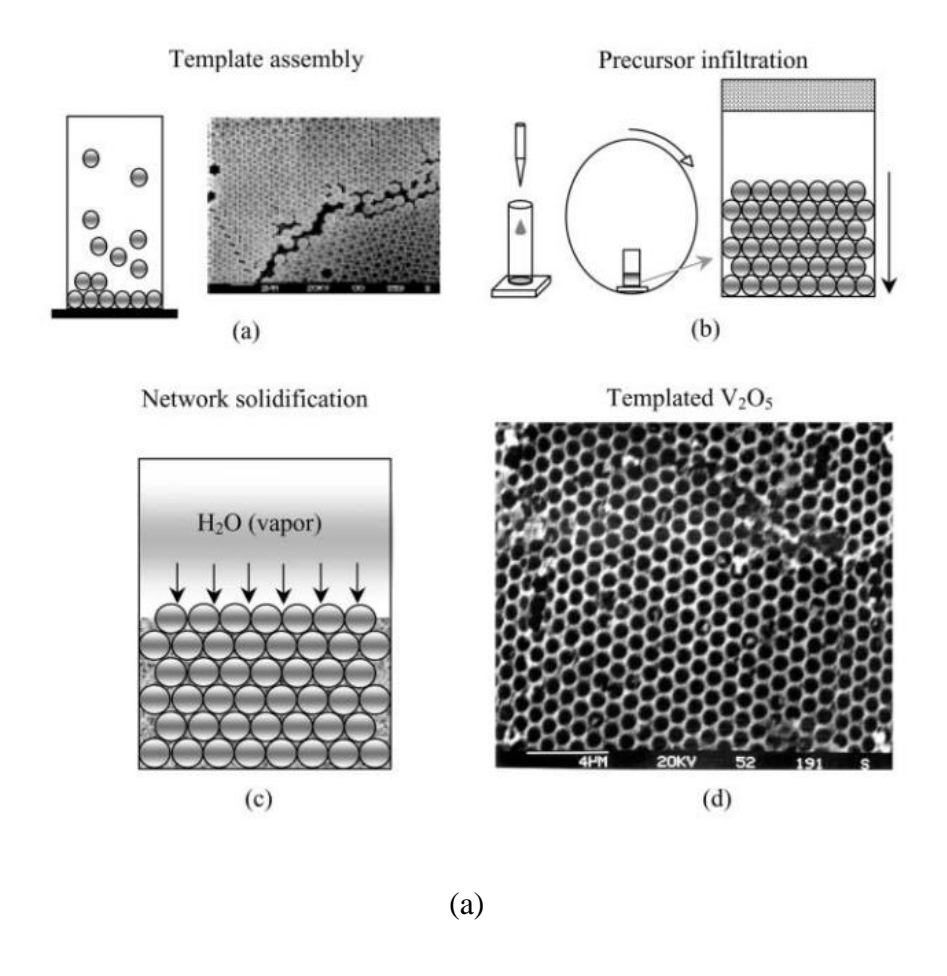
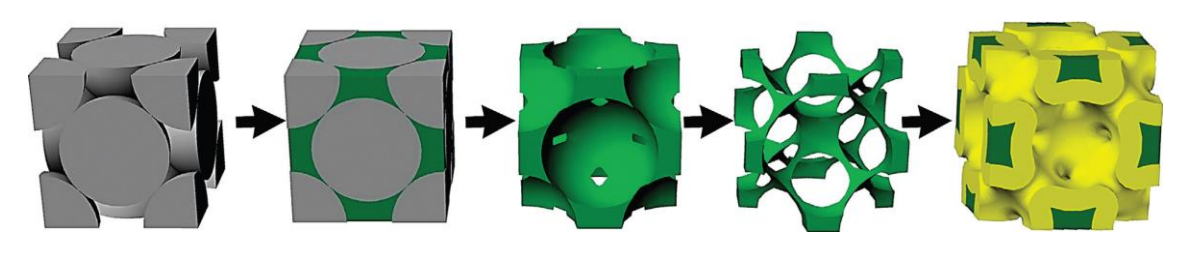
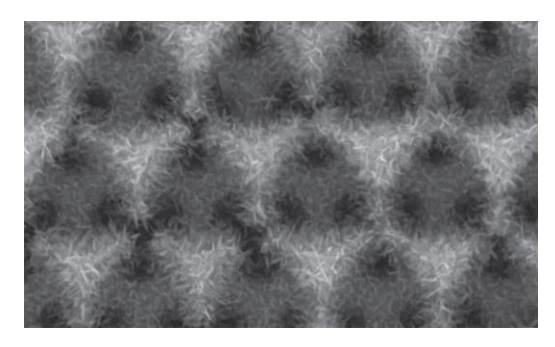


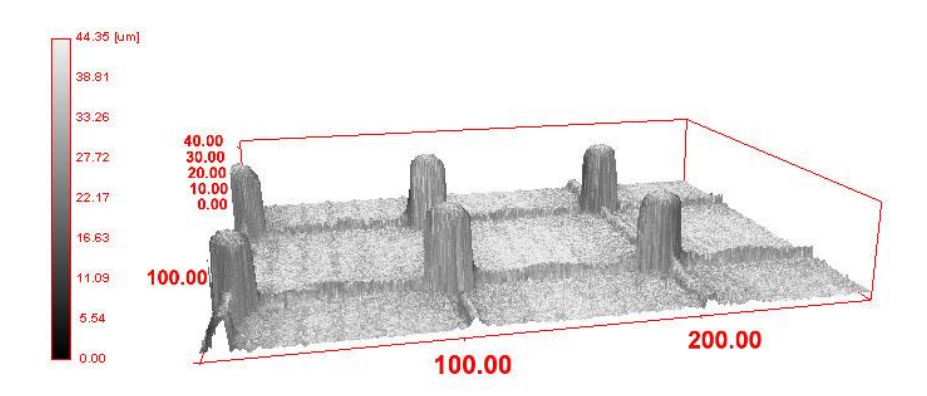
Figure 4-1: Previously reported 3D architecture electrode designs and fabrication methods. (a) Process for fabricating the hierarchical  $V_2O_5$  electrode [68]. (b) Outline of the Ni foam fabrication by template based method. Lower image is  $MnO_2$  electrode fabricated by electrodeposition on Ni foam [69]. (c) A schematic of 3D image of pillars by Super ink jet printing [120]. (d) Outline of the electrode fabrication process. Left lower shows the surface of a patterned electrode and right lower shows cross-section of a patterned electrode [70].

Figure 4-1 (cont'd).



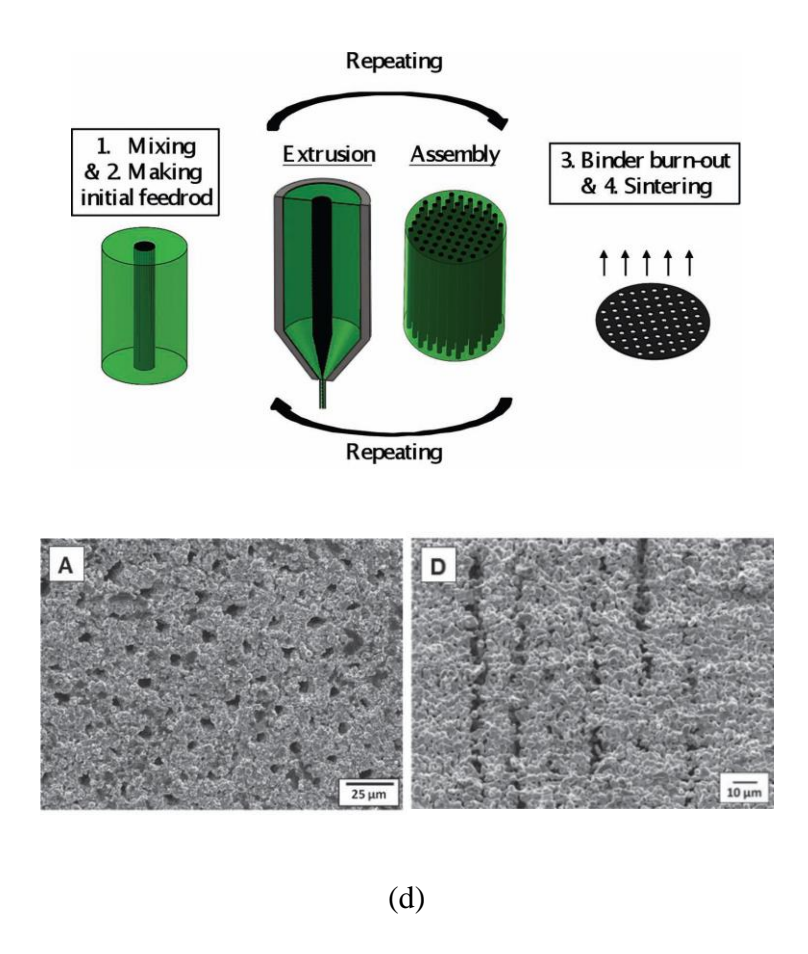


(b)



(c)

Figure 4-1 (cont'd)



# 4.2 Highly ordered hierarchical (HOH) graphite electrode

In the present work, a highly-ordered and hierarchical (HOH) graphite electrode is proposed to achieve high specific energy and power density. Based on our experimental results, the intercalation process was intensively focused.

## 4.2.1 Laser patterning technique

Keeping in mind the desired electrode design and scale-able processing, laser patterning investigated as a technique to fabricate HOH electrodes. The basic principle is to introduce cylindrically-shaped and through-thickness pores by laser ablation. The laser ablation provides several advantages: 1) Laser patterning is a post calendaring process, thus the laser ablated porosity will not be affected by further electrode fabrication; 2) Laser patterning enables precise control over the cylindrical pore position and geometry; 3) Laser patterning is a non-toxic process. Unlike previous template-based techniques, no chemicals required for laser patterning. CO<sub>2</sub> is the product of graphite ablation/oxidation; 4) Because state-of-the-art lasers can achieve adequate intensity, the ability to penetrate several hundred microns thick graphite electrodes is expected; 5) The laser patterning process can be fast if commercial galvo-focusing heads or equivalent are employed. It takes a few seconds to make a pattern on electrode by laser. In addition, solid-state lasers typically do not require extensive maintenance.

## 4.2.2 HOH electrode design

As discussed in Chapter 3, the internal resistance of electrolyte-filled pores inside a porous electrode can be a rate limiting process in a thick electrode (Figure 4-2a). Thus, the electrode design must facilitate Li-ion transport through the electrode thickness to provide a homogeneous ionic current, especially at high charge rates. In this regard, the HOH electrode was designed. The HOH electrode is the electrode consisting of an array of highly ordered or close-packed linear channels that direct transport of Li-ions into smaller intrinsic pores (Figure 4-2b). First,

macro-scale linear channels are produced in a conventional graphite electrode (Figure 4-2b) to allow for uniform Li-ion transport. Second, close-packed hexagonal patterning was employed to improve enable a uniform Li-ion current through the entire electrode (Figure 4-2b). Since macro-scale linear channels can facilitate Li-ions diffusion, Li-ions will transport through the larger and linear channels first then diffuse from the walls of the channels to the intrinsic pores between active particles. Thus, the spacing between channels should be minimized to reduce the diffusion length in micro-scale intrinsic pores. The close-packed hexagonal patterning provides not only the shortest spacing between channels, but the same spacing between channels, which contributes homogeneous Li-ions distribution in a porous electrode by offering the same diffusion length. Though it seems that the lateral distance between linear channels should be minimized, the cumulative electrode porosity should be less than ~50 % to maximize energy density. Thus, the optimum engineered porosity should be determined to maximize energy and power density simultaneously. In addition, the patterning process should be able to make sufficiently small features (~ tens of μm). For example, cylinders 50 μm in diameter would provide approximately half diffusion distance between channels compared to 100 µm diameter channels, assuming the total volume fraction of patterned porosity is fixed. However, the linear channel size is typically proportional to the laser power. Therefore, it is required to optimize a HOH patterning conditions for the electrode with high energy and power density. In the next section, the HOH fabrication conditions were optimized.



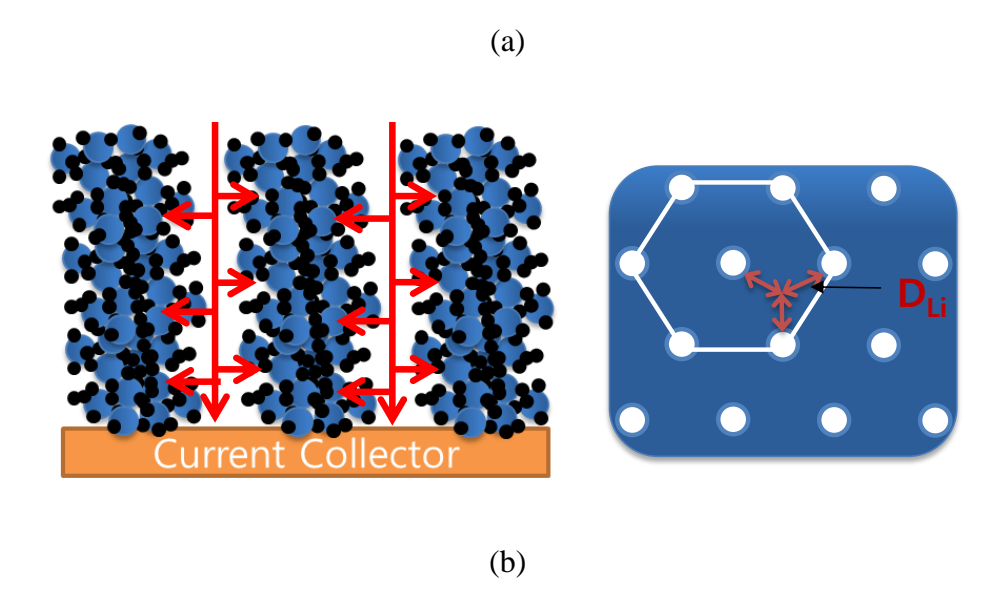


Figure 4-2: Schematic representation of possible Li-ion diffusion paths (a) in a conventional porous electrode, (b) in a HOH electrode, and schematic of top view of HOH electrode and short Li-ion diffusion length induced by hexagonal close-packed linear channels.

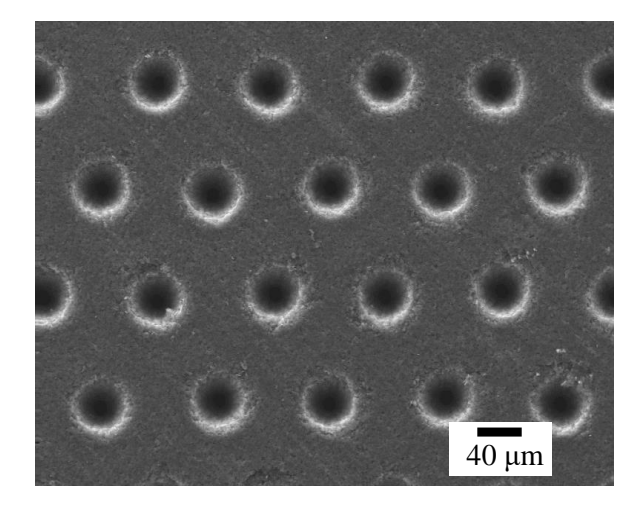
# 4.2.3 HOH electrode design optimization

To demonstrate the feasibility of the laser patterning process on thick graphite electrodes, the introduction of 10 % laser patterned porosity was attempted on conventional graphite electrodes consisting of 4 mAh cm<sup>-2</sup> loading and 40 % intrinsic porosity (thickness:  $\sim$ 100  $\mu$ m). According

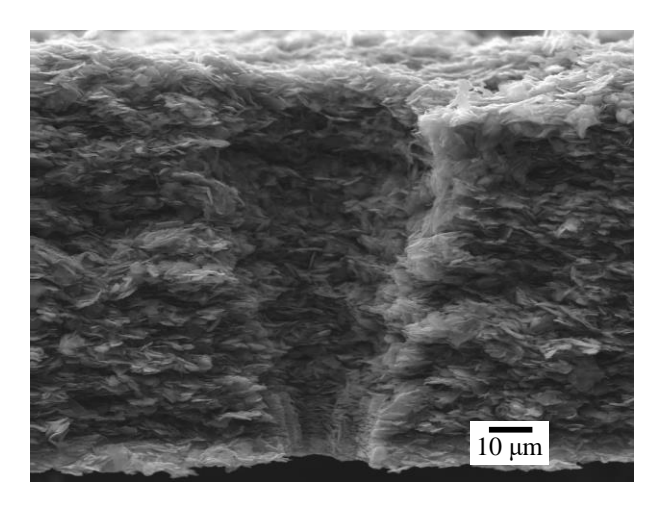
to Zheng et al.[121], relationships between areal capacity and maximum C-rate with variable electrode thickness up to 100 µm was mainly attributed to the impedance related to the Li-ion transport in the electrolyte in the pores of the electrode. Therefore, a 100 µm thick electrode was selected for laser patterning. The HOH electrode was successfully fabricated as intended (Figure 4-3a). It indicates that the laser technique enables precise patterning on a thick electrode. The minimum linear channel size was approximately  $\sim 53 \pm 1.2 \,\mu m$  (Figure 4-3a), but in the initial stages of this investigation, the holes were clearly tapered (Figure 4-3b). Since the laser is designed to focus from 5 mm down to 20 µm diameter, the nature of the laser patterning causes conical shaped holes resulting in approximately 60 % less ablated porosity compared to if perfect cylinders were made. In addition, there was evidence of channels collapse likely due to inadequate spacing (Figure 4-3c). This indicated that the electrode walls between channels could be collapsing during the laser patterning process when the laser patterned porosity exceeds a critical volume fraction. The maximum laser patterned porosity in the graphite electrode with 4 mAh cm<sup>-2</sup> and 40 % intrinsic porosity was approximately 9 %. It is assumed that overlapping heat affected zones caused the channels collapse. Thus, total volume fraction of linear channels was reduced to 5 % for the thicker 5.5 mAh cm<sup>-2</sup> electrodes (~143 µm at 45 % porosity). To meet the accurate target volume fraction of linear channels in a HOH electrode, the total number of channels was increased by about 60 % to compensate for the effect of conical shaped channels (i.e. conical:  $1.1 \times 10^5 \ \mu m^3$ , cylindrical  $2.9 \times 10^5 \ \mu m^3$  in HOH electrode with  $5.5 \ mAh \ cm^{-2}$ loading and total 50 % open porosity).

In HOH electrodes, the sum of the Li-ion transport resistance consists of the transport resistance in the laser ablated linear patterned channels (macro-scale;  $\varepsilon_M$ ) and in the intrinsic pores (micro-scale;  $\varepsilon_m$ ). Macro-scale laser ablated linear channels ideally reduce the total mass transport

resistance by offering wide, shorter and line-of-site Li-ion diffusion paths. However, incorporating macro-scale linear channels into graphite electrodes causes the lower intrinsic micro-scale open porosity ( $\varepsilon_{total} = \varepsilon_M + \varepsilon_m$ ) compared to the average intrinsic open porosity of a conventional graphite electrode ( $\varepsilon_{total} = \varepsilon_m$ ) of the same total open porosity. Thus the cumulative open porosity ( $\varepsilon_{total}$ ) was fixed at 50% in all cases to minimize the impedance associated with Li-ion mass transport caused by the intrinsic porosity. It was determined that the effects of intrinsic porosity are negligible between 40 % and 50 %. The rate capability of the electrodes with 5.5 mAh cm<sup>-2</sup> showed similar values at various C-rates, regardless of the open porosity between 40 % and 50 %. After the laser patterning, a precise circular shape electrode was obtained by laser cutting without a mechanical damage generated by cutting tools (Figure 4-3d).



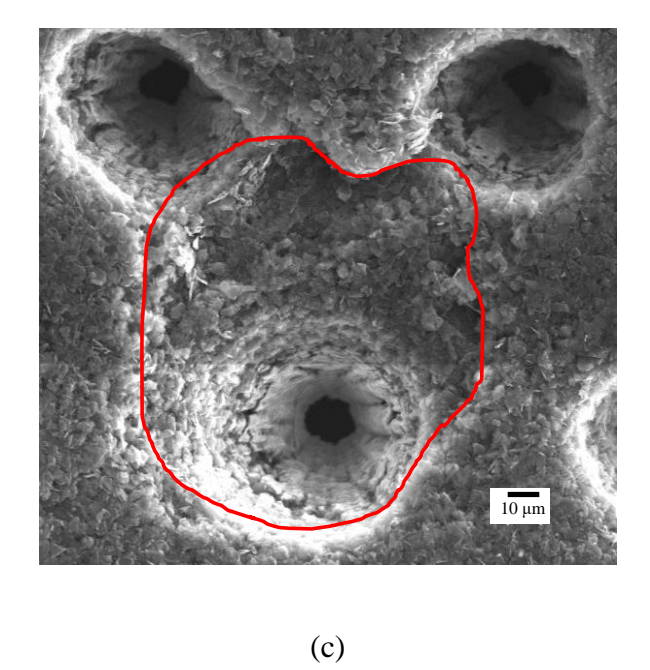
(a)

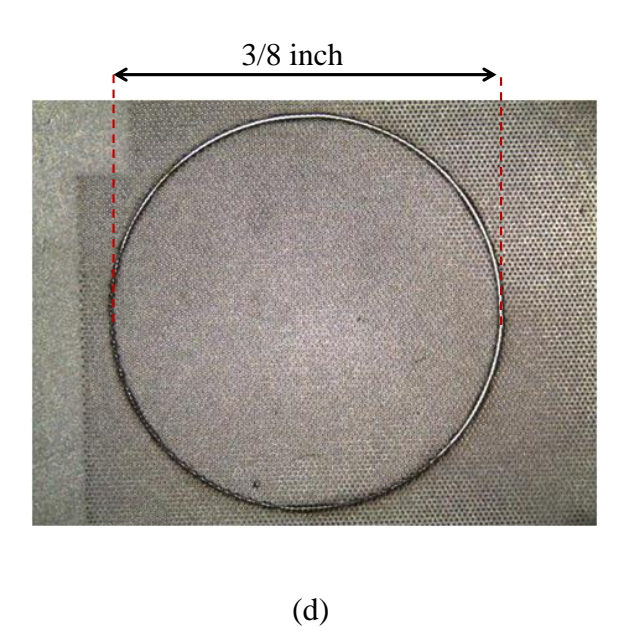


(b)

Figure 4-3: Secondary SEM images of laser patterned electrode (Timcal, SFG6, 4.0 mAh cm<sup>-2</sup>, 50 % porosity) (a) top view of fabricated HOH electrode, (b) cross-section of a conical shaped pattern, (c) collapsed walls between laser-ablated channels, and (d) a laser cut HOH electrode after laser patterning (3/8 inch diameter).

Figure 4-3 (cont'd).

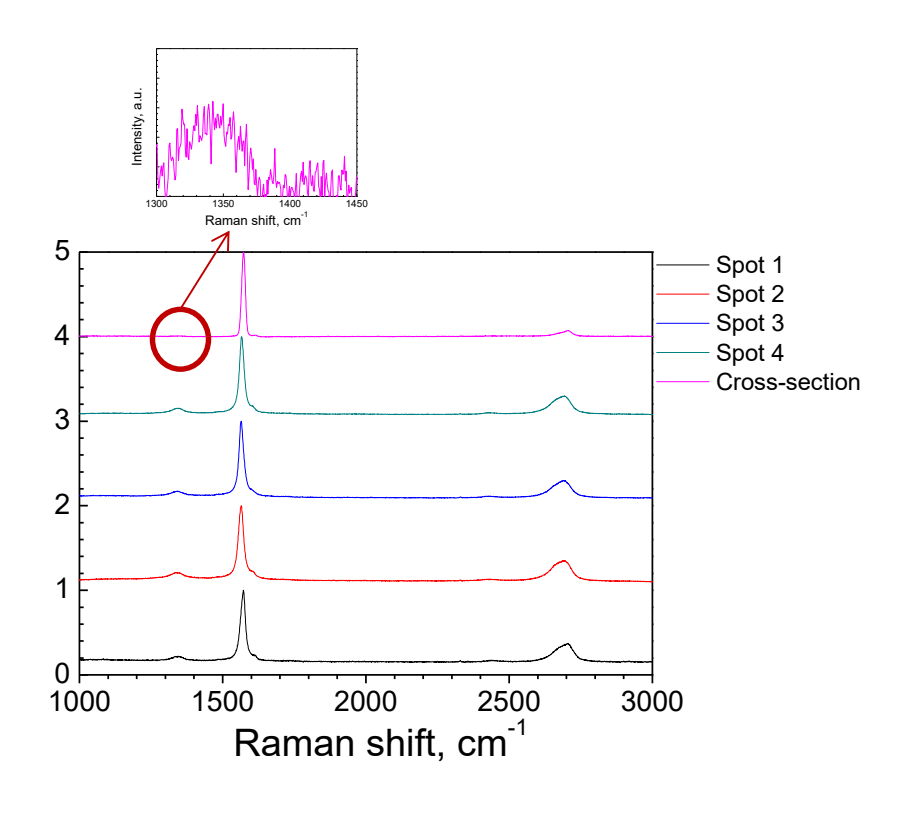




## 4.2.4 HOH electrode characterization

# 4.2.4.1 Phase characterization by Raman spectroscopy

Since laser patterning produces intense heat, it was possible that the graphite could have been affected. Thus graphite in an HOH electrode was characterized using Raman spectroscopy. Raman spectroscopy was conducted from spot 1 to 4 (Figure 4-4) on surface and on fractured HOH graphite electrode surface. Although the Raman spectrum of the cross-section showed a weak peak at ~1340 cm<sup>-1</sup>, all Raman spectrum peaks of the HOH electrode are consistent with the graphite in non-laser ablated electrodes. In addition, there is no observable secondary phase peaks. The resulting Raman spectrum is in agreement with typical Raman spectrum of graphite [95], and it indicates that laser patterning does not cause any phase changes in a graphite electrode.



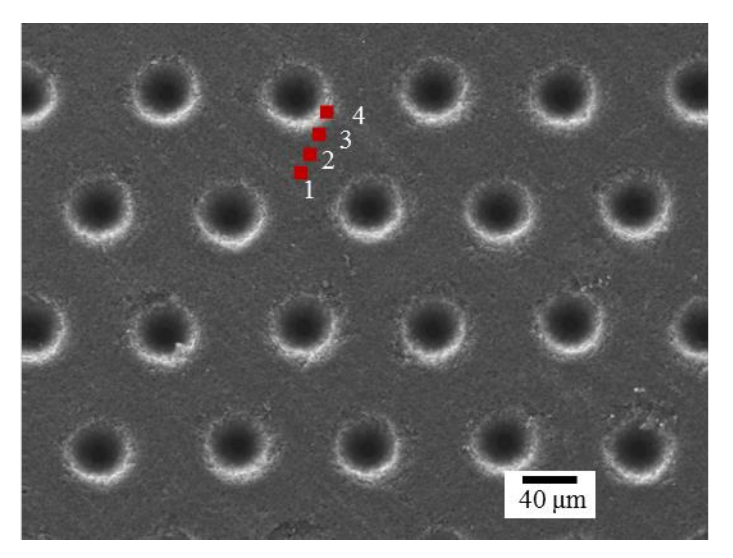
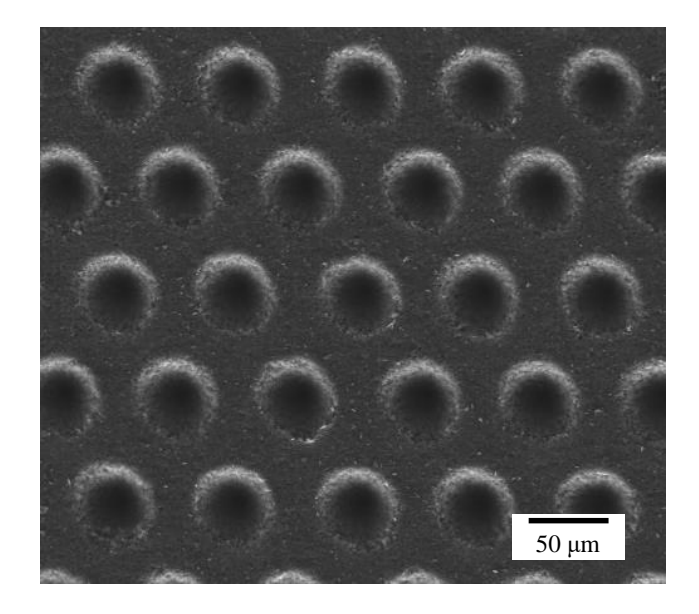


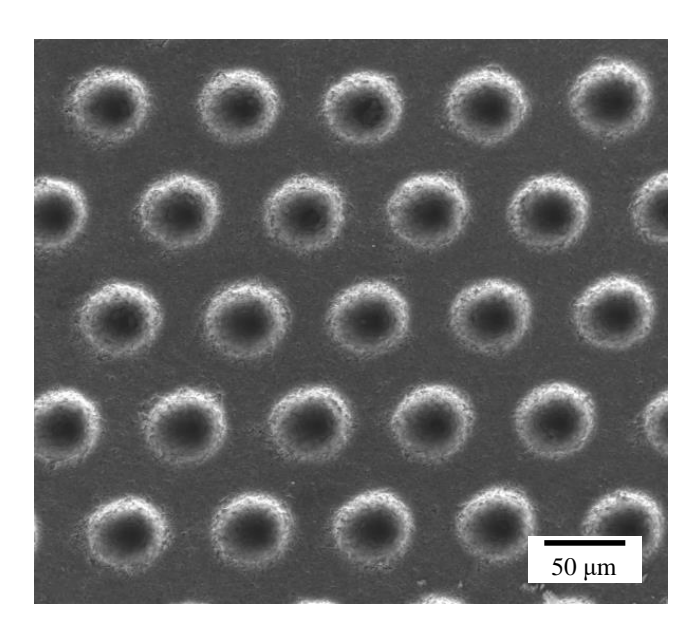
Figure 4-4: Raman spot analysis of an HOH graphite electrode at various spots (1 to 4 and cross-section).

## 4.2.4.2 Morphological analysis

After rate mapping tests, SEM morphological analysis of HOH electrodes was conducted to compare HOH electrodes before and after rate mapping (Figure 4-5). The purpose of the test was to determine if the mechanical integrity of the HOH electrode was compromised by introducing the laser ablated channels. Since there is volume change in the graphite electrode that occurs during charge and discharge processes, it is possible that the laser ablated channels could cause particle erosion. For the SEM analysis, the cycled HOH electrodes were rinsed in dimethyl carbonate (DMC) to remove the Li salt (LiPF<sub>6</sub>) that precipitate on the surface thereby covering the electrode topography. Based on the SEM analysis (Figure 4-5), there was no observable morphological change before and after rate mapping. This indicated that HOH electrodes maintained their integrity during cycling. It is in good agreement with the results of Raman spectroscopy analysis



(a)



(b)

Figure 4-5: SEM images of laser patterned graphite electrode (SFG6 graphite electrode with 5.5 mAh cm<sup>-2</sup> and 50 % total open porosity). (a) Top view of HOH electrode before and (b) after rate mapping.

## 4.3 Summary

In this Chapter, the novel HOH graphite electrode design and fabrication were presented, which include linear laser ablated channels in closed-packed hexagonal arrays, to improve the rate capability in thick graphite electrodes. Previous electrode architecture approaches have demonstrated that controlling the electrode microstructure can enhance the rate capability of Li-However, it is still a challenge to use these techniques for practical cell ion batteries. manufacturing due to their complexity and high production cost. Therefore, the laser patterning technique was employed due to its ease of integration with state-of-the-art production and potentially low production cost. The thick HOH electrode (>100 µm) including laser ablated linear-macro channels was successfully obtained by laser patterning. The minimum pattern pore size was ~53 μm in diameter. The laser-ablated porosity was fixed as 5 % to avoid the effects of heat affected zone by laser beam. The Raman spectroscopy and SEM analysis have proved that there is no phase change and mechanical degradation during rate mapping tests after laser patterning. To date, this is the first report of the homogeneous patterning of an electrode with a thick electrode (>100 µm) with a technique that could be integrated into a conventional roll-toroll process.

#### 5 Electrochemical characterization of HOH electrodes

# 5.1 Solid-state Li diffusivity in graphite electrode

The rate capability of Li-ion batteries can be significantly influenced by the diffusivity of Li inside active materials. Therefore, solid-state Li diffusivity  $(D_{Li})$  has to be accurately measured to determine the rate limiting step. There are different electrochemical techniques for measuring  $D_{Li}$  such as the galvanostatic intermittent titration technique (GITT)[79], potential intermittent titration technique (PITT)[122], electrochemical impedance spectroscopy (EIS)[123], and cyclic voltammetry (CV)[124]. However, in the literature, there is discrepancy of  $D_{Li}$  values for the same materials. For example, orders of magnitude differences in  $D_{Li}$  values were reported in the previous study by Shen et al.[125]. This inconsistency can be attributed to the different electrode preparation and construction such as phase, porosity, size, and shape of electrochemical active materials. It is well known that the solid-state diffusion rate is strongly dependent on the SOC, which causes phase transitions during charging and discharging. Figure 5-1 shows the potential of the graphite electrode with a 1.2 mAh cm<sup>-2</sup> loading and 63 % porosity as function of x in Li<sub>x</sub>C<sub>6</sub>. A sequence of constant potential plateaus is clearly observed in the potential vs composition plot. This phenomenon is called staging whereby a constant potential plateau indicates that two distinct Li<sub>x</sub>C<sub>6</sub> phases are in thermodynamic equilibrium. According to Gibbs phase rule, when two phases are in equilibrium, there are two degrees of freedom necessitating a constant potential, assuming pressure and temperature are fixed [15]. A stage refers to Li occupying a specific stacking configuration. For example, in stage 4, Li-ions are intercalated in every forth basal layer in a stack of basal planes found in graphite. Subsequently, Li-ions are intercalated in every third and second basal plane in stages 3 and 2, respectively. When a graphite electrode is fully charged (x=1 in  $Li_xC_6$ ), each graphite layer is filled with Li.

This staging is a thermodynamic phenomenon, thus distinct voltages are associated with each stage transition. Moreover, the solid-state Li-ions diffusion rate is affected by the SOC. Originally, GITT and PITT methods were developed for dense planar electrodes such as single crystal highly-oriented pyrolytic graphite (HOPG)[15]. However, conventional graphite electrodes are porous and composed of an assembly of graphite particles bound together by a polymer binder. Thus, the actual interface area is dependent on the electrode preparation and construction such as materials (size and shape), inactive components (binder), and porosity.

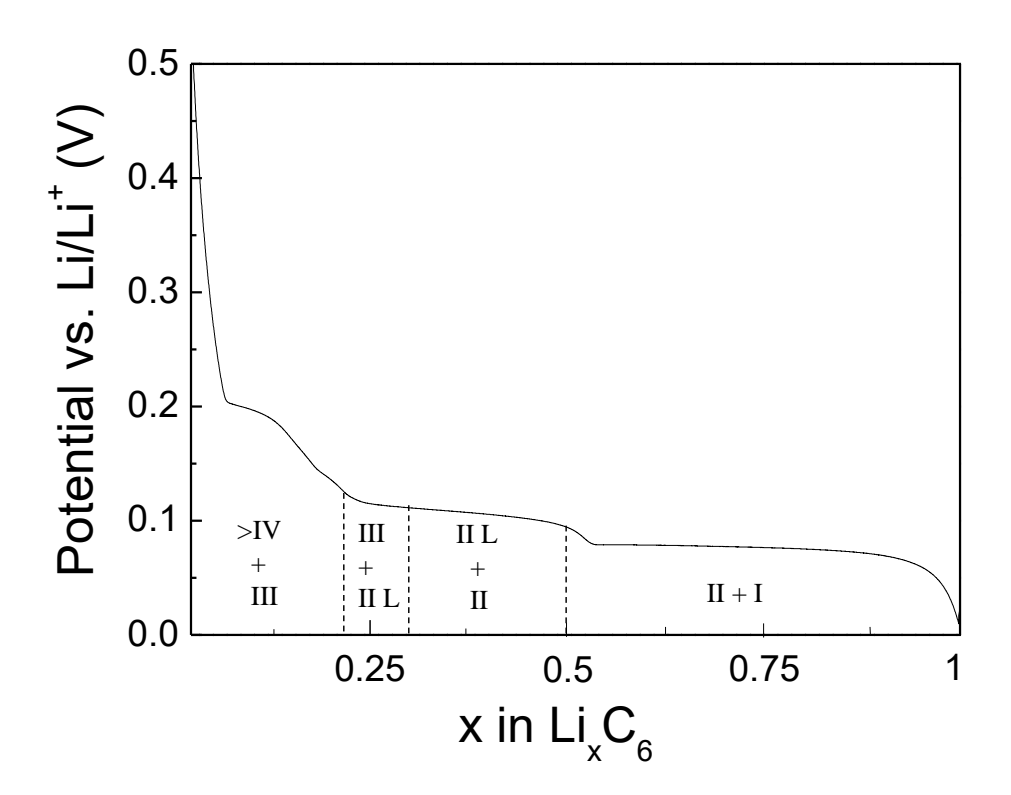


Figure 5-1: Typical potential vs x in  $Li_xC_6$  plot with 1.2 mAh cm<sup>-2</sup> and 63 % SFG6 graphite electrode.

In the present work, the GITT technique was used to determine  $D_{Li}$  of the graphite electrodes. For GITT, the conventional graphite electrodes with 1.2 mAh cm<sup>-2</sup> and 63 % were fabricated. SFG6 graphite (TIMCAL, Bodio, Swizerland) was used for all experiments. The surface area of SFG6 particles is reported as approximately 17.1 m<sup>2</sup> g<sup>-1</sup>. However, as was discussed, the surface area can be reduced by the electrode conditions. Since the conventional graphite electrode was composed of 90 % SFG6 and 10 % PVdF binder, BET analysis was conducted to obtain the actual surface area of the same composition and open porosity (63 %) of the graphite electrode. As a result, the measured surface area was 6.9 m<sup>2</sup> g<sup>-1</sup>. This value is approximately 60 % lower than the sum of the surface area of particles. This difference can result from occluded porosity between particles resulting from the presence of the PVdF binder. Additional experimental details are described in Chapter 2.

Figure 5-2 presents the GITT plot of the graphite electrode with 1.2 mAh cm<sup>-2</sup> and 63 % porosity. The measured potential range was 80 mV to 0.75 V and the staging phenomena are clearly observable (Figure 5-2). The  $D_{Li}$  values of the graphite electrode were calculated by Eq. 2-2 based on the GITT plot. Essentially, the  $D_{Li}$  values increasing as the SOC decreased, as expected [111]. The  $D_{Li}$  values were 1.8 x 10<sup>-8</sup> cm<sup>2</sup> s<sup>-1</sup> at SOC 60 %, 3.8 x 10<sup>-8</sup> cm<sup>2</sup> s<sup>-1</sup> at SOC 40 %, and 1.1 x 10<sup>-7</sup> cm<sup>2</sup> s<sup>-1</sup> at SOC 20 %, respectively. These values are consistent with the  $D_{Li}$  range (10<sup>-7.5</sup>-10<sup>-9.5</sup> cm<sup>2</sup> s<sup>-1</sup>) of artificial graphite electrode, which is calculated by Takami *et al.*[111].

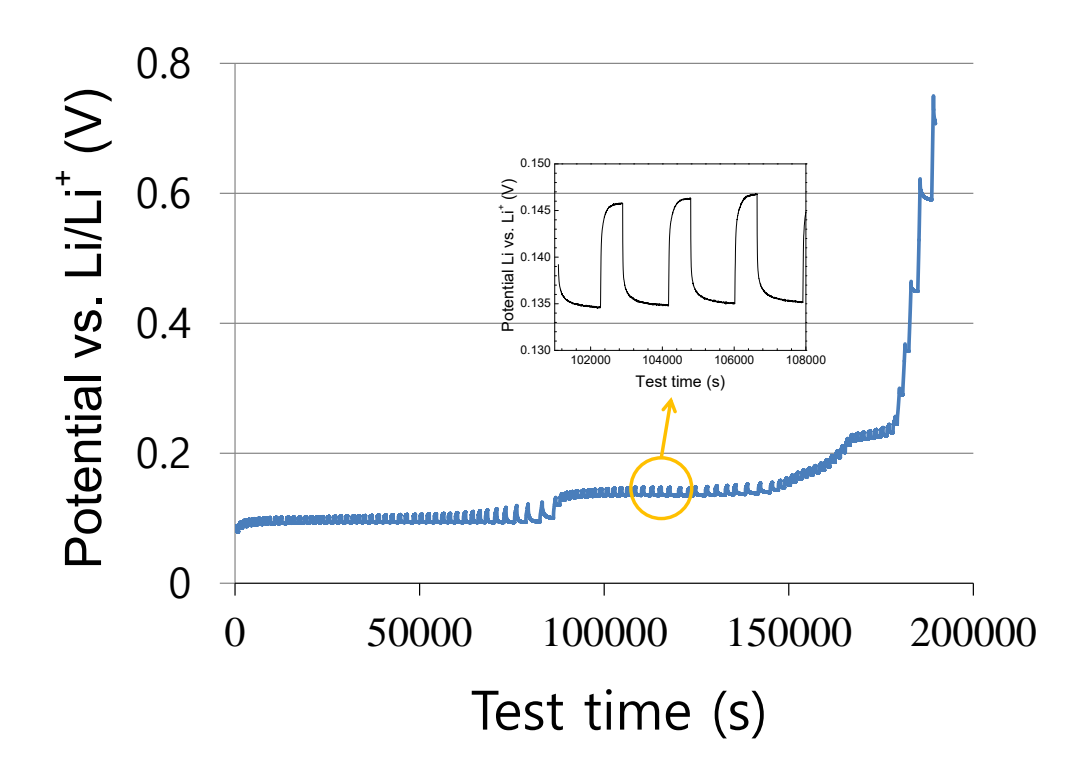


Figure 5-2: The GITT plot of the graphite electrode with  $1.2~\text{mAh}~\text{cm}^{-2}$  and 63~% porosity. The measured potential range was 80~mV to 0.75~V.

# 5.2 Rate mapping

## **5.2.1** Effects of loading

To understand the effects of electrode loading on rate performance, rate mapping was conducted with three different loadings (1.15 mAh cm<sup>-2</sup>, 4 mAh cm<sup>-2</sup>, and 5.5 mAh cm<sup>-2</sup> with 50 % open porosity) of conventional graphite electrodes as a function of intercalation rate from 1/5 to 10 C-rate after conditioning cycles (Figure 5-3). From Figure 5-3, several important points are noted. First, SFG6 graphite electrodes, the active material mainly used in this study, satisfies the high reversible capacity and stable cycleability demands in Li-ion batteries. In general, graphite electrodes undergo irreversible capacity loss during de/intercalation cycles due to side reactions

such as a SEI formation by a reductive decomposition reaction of the electrolyte composed of organic solvents and Li salt [43]. Thus, it is important for active materials to have low irreversible capacity loss for the higher practical reversible capacity. In this regard, 1.15 mAh cm<sup>-2</sup> graphite electrode showed high reversible specific capacity of 353±8 mAh g<sup>-1</sup> (theoretical capacity (372 mAh g<sup>-1</sup>)) at 1/5 C-rate, and there was no observable irreversible capacity loss during rate mapping up to 10 C-rate (Figure 5). This behavior is in good agreement with previous work [19]. It indicates that a stable SEI layer is formed during the preconditioning protocol, thus preventing additional irreversible capacity loss by inhibiting further electrolyte decomposition. In addition, the capacity retention of the electrodes reached approximately 99±1 % of the capacity in the first cycle capacity at the same 1/5 C-rate after extreme cycles regardless of the loadings. It confirms that the performance of SFG6 graphite electrode is not degenerated by drastic cycling conditions and the capacity diminishes with increasing intercalation rate is not a result of irreversible capacity loss. Second, the capacity retention decreases as a function of increasing electrode loading. This correlation between loading and capacity retention is comparable to previous studies [19,62]. The 4 and 5.5 mAh cm<sup>-2</sup> graphite electrodes achieved approximately 30 % and 70 % lower capacity retention at 1/3 C-rate, and 60 % and 87 % lower capacity retention at 1/2 C-rate compared to those of 1.15 mAh cm<sup>-2</sup>. This behavior can be attributed to IR polarization potential. 5.5 mAh cm<sup>-2</sup> electrodes require approximately 5 times higher current density compared to that of 1.15 mAh cm<sup>-2</sup> electrodes to charge at the same C-rate. Since, consequently, the IR resistance is proportional to current density, the 5.5 mAh cm<sup>-2</sup> electrode undergoes about 5 times higher IR polarization which can cause premature potential cut-off. To support these assumptions, rate mapping was conducted with a high loading of 5.5 mAh cm<sup>-2</sup> electrode at slow intercalation rate (1/10 C-rate) and, as expected, showed reasonable

specific capacity (336 mAh g<sup>-1</sup>)(Figure 5-3). Third, the specific capacity retention diminished as increase the intercalation rate regardless of the electrode loadings (Figure 5-3). It can be attributed to the polarization in the same manner with the correlation between capacity retentions and loadings of electrodes because the current related polarization potential drop increases as a function of the intercalation rate.

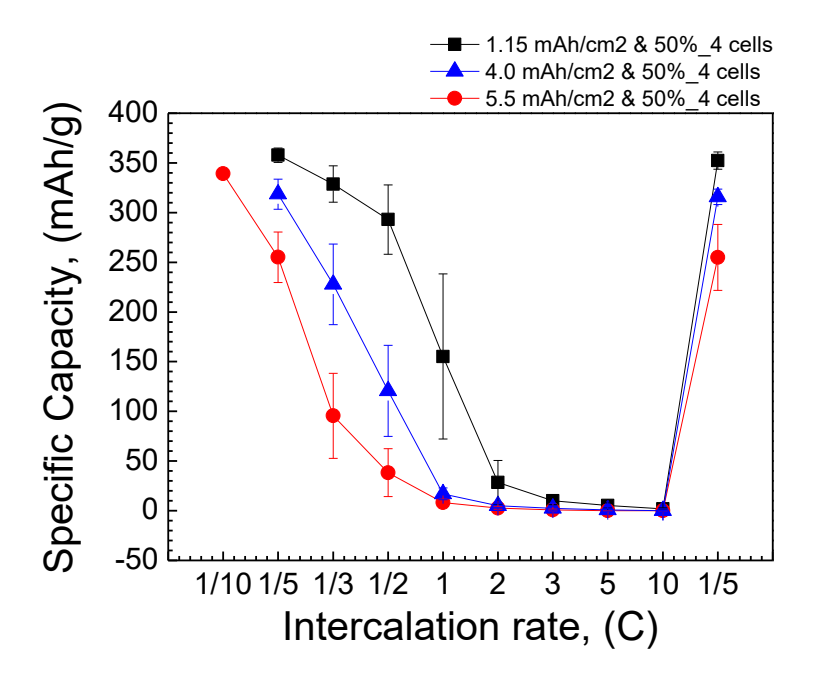


Figure 5-3: Results of rate mapping as a function of graphite electrodes with various loading from 1.15 mAh cm<sup>-2</sup> to 5.5 mAh cm<sup>-2</sup> with the same total open porosity (50 %). N=4.

### 5.2.2 HOH graphite electrode vs conventional graphite electrode

The rate performance of conventional electrodes and HOH electrodes were compared at various C-rates (Figure 5-4). The percent capacity retention *vs* intercalation C-rate is shown in Figure 5-4ab. The percent capacity is calculated assuming the capacity at relatively low rate (1/5 C-rate) is 100 %. Both types of electrodes were prepared with 1.15 mAh cm<sup>-2</sup>, 4.0 mAh cm<sup>-2</sup>, and 5.5

mAh cm<sup>-2</sup> loadings, respectively, and their total open porosity was fixed as 50 % as discussed in Chapter 4. Unlike conventional electrodes, HOH electrodes consist of 5 % laser ablated linear porosity and 45 % intrinsic open porosity. It is seen that the average capacity retention as a function of increasing rate for each types of electrode is similar up to the 4 mAh cm<sup>-2</sup> loading (Figure 5-4a). On the other hand, the HOH electrodes, which have a 5.5 mAh cm<sup>-2</sup> loading, exhibited 65 % and 120 % higher capability in percentage compared to those of a conventional graphite electrode at 1/3 C and 1/2 C-rate, respectively (Figure 5-4b). In addition, it is interesting to note that the specific capacity retention also improved despite the fact that laser ablated channels decreasing the amount of electrochemical active material per unit area (capacity)(Figure 5-4c). Typically, it is believed that the relatively high loading (thick) electrode has a more tortuous and longer Li-ion transport paths compared to those of the lower loading electrodes. The longer and more tortuous Li-ion diffusion paths cause more likely concentration polarization. This can result in higher local IR resistance in electrolyte-filled pores inside a porous electrode by the non-uniform current density inside of a porous electrode [68]. Since only the 5.5 mAh cm<sup>-2</sup> loading HOH electrodes showed significant improvement in rate capabilities compared to conventional electrodes, the local resistance of electrolyte-filled pores inside a porous electrodes seems to rapidly increase between 4.0 mAh cm<sup>-2</sup> (~100 µm) and 5.5 mAh cm<sup>-2</sup> (~157 μm) electrode loadings with 50 % open porosity. These results indicate that mass transport resistance, which results in concentration polarization, inside the porous electrode can be dominant when the electrode is sufficiently thick (>100 µm), and it is believed that the HOH electrodes can reduce the mass transport resistance. As predicted, the uniformly patterned macro-scale linear channels can provide improved Li-ion diffusion paths through the linear channels and reduced diffusion distance in micro-scale intrinsic pores. The improved mass

transport properties enable more uniform Li-ion distribution at high C-rate, which leads higher capacity retention by suppressing concentration polarization. Concentration polarization leads to significant cell polarization potential drop and also causing Li deposition. Therefore, the design of linear channels can mitigate safety concerns by suppressing the Li deposition possibility. Additionally, there are no advantages observed in HOH electrodes at high C-rates (>1 C-rate) regardless of electrode loadings. This can be attributed to solid-state diffusivity limitations, which leads to particle scale concentration polarization resulting in a rapid reduction in cell potential (Figure 5-5)[126]. Since a number of Li-ions simultaneously intercalated into a graphite particle in short time scale under fast charge rate, the Li concentration at the edge of the particle is alike SOC 100 % even the center of the particle is empty (concentration polarization). As a result, the capacity retention significantly drops because the concentration polarization leads to reach the premature cell cut-off potential before each particle is saturated by Li [126]. Consequently, the solid-state diffusivity can dominate the rate capability above 1 C-rate instead of the resistance of Li-ion diffusion through electrolyte-filled pores inside a porous electrode (tortuosity).

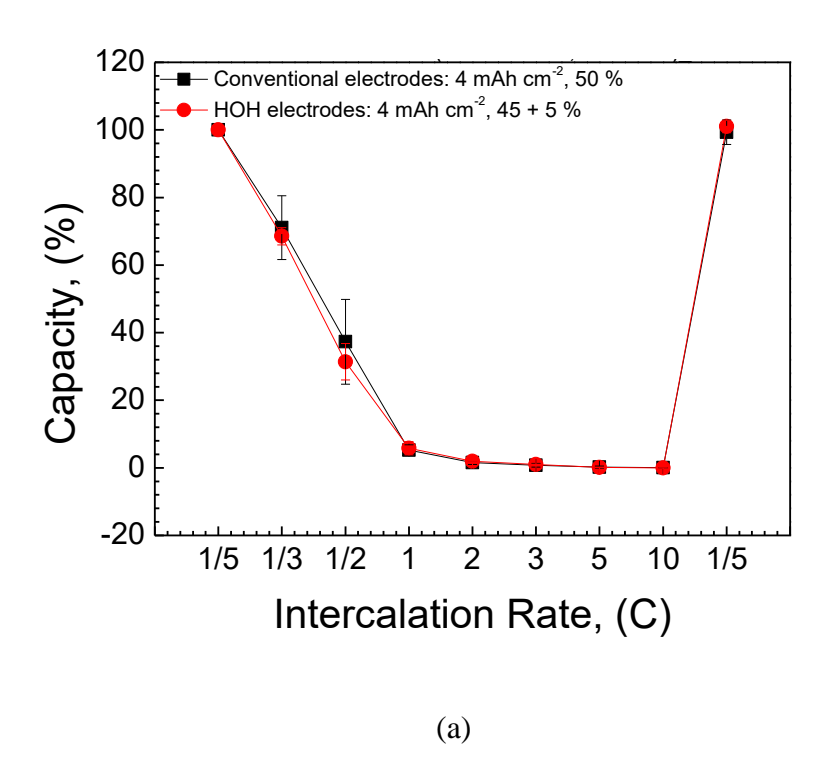
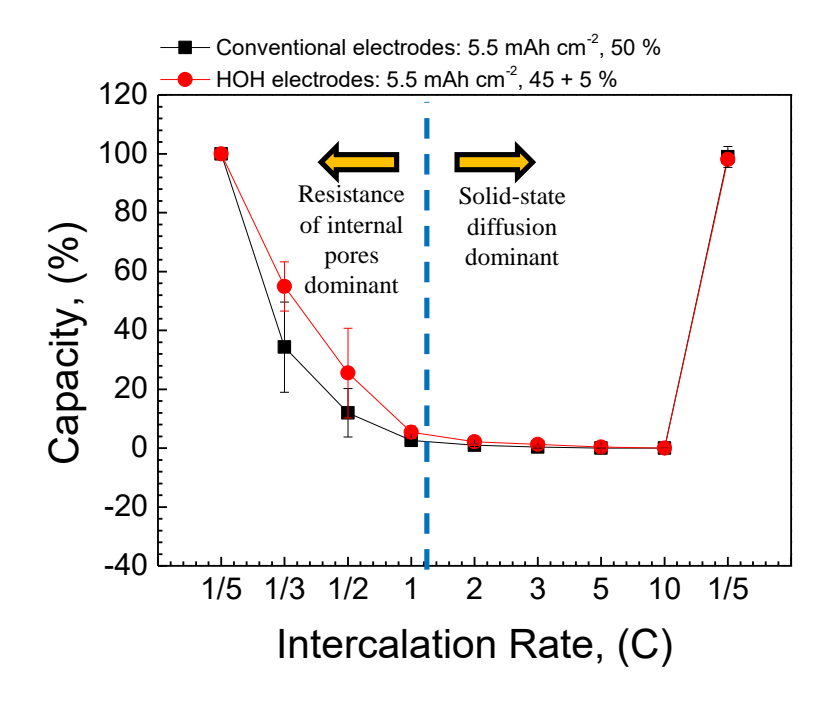
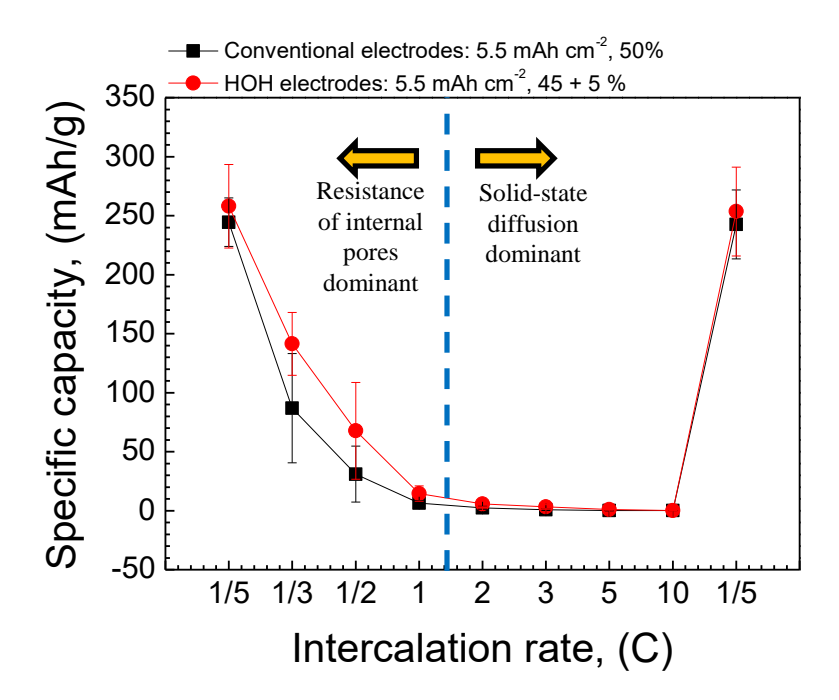


Figure 5-4: Charge rate mapping as a function of SFG6 graphite electrodes with conventional and HOH electrodes with 50 % total open porosity. (a) Capacity (%) *vs* intercalation rate with 4 mAh cm<sup>-2</sup>, (b) with 5.5 mAh cm<sup>-2</sup>, and (c) specific capacity (mAh g<sup>-1</sup>) *vs* intercalation rate with 5.5 mAh cm<sup>-2</sup>. N=4.

Figure 5-4 (cont'd).



(b)



(c)

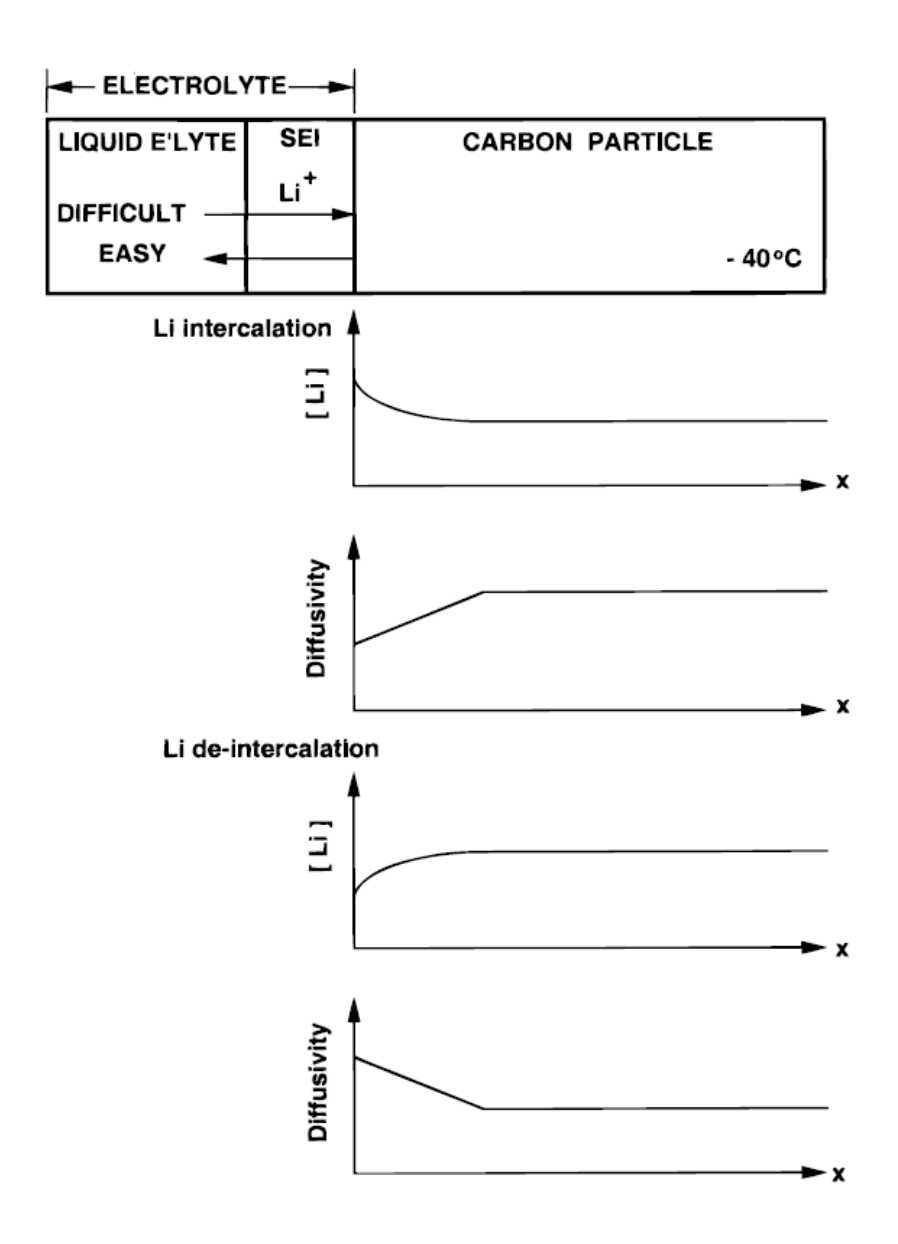


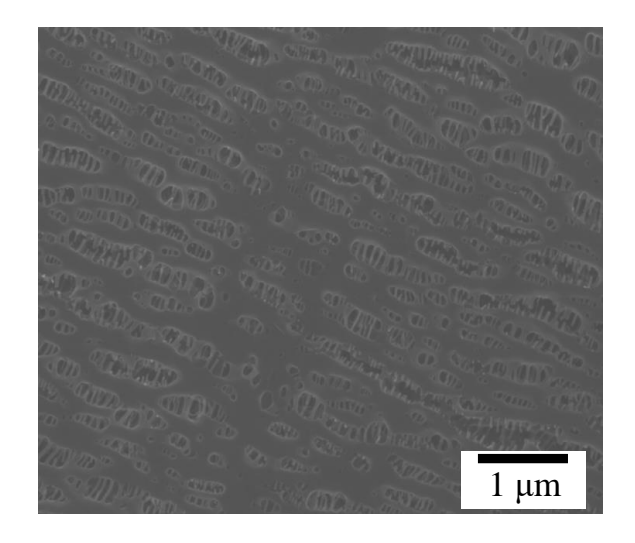
Figure 5-5: Schematic diagram showing the Li concentration and diffusivity profiles in a graphite electrode [126].

#### **5.2.2.1** Effects of separators

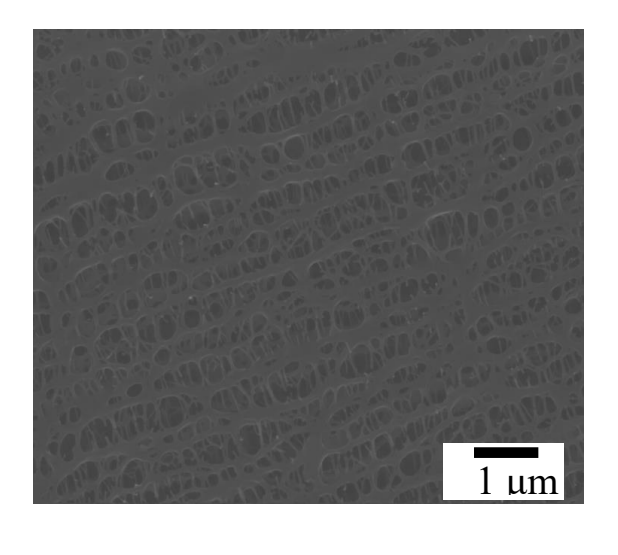
The main role of the separator is to prevent physical contact of the electrodes while providing an ionic transport path and preventing electronic transport. Ideally, separators should have sufficient porosity (>40 %) to allow for the facile diffusion of ionic species, while the pore size should be small (<1 µm) to prevent electrode active materials and the conducting additives penetration [127]. Furthermore, in the event of Li dendrite formation and exfoliation, the separator should block the exfoliated Li (also referred to as Li moss) transport, which can cause cell failure. In addition, the separator should be thin enough to minimize the diffusion distance between electrodes. Therefore, the structure of a porous separator is typically highly tortuous to meet the required properties. This tortuous structure of separator can induce high *IR* resistance at high current densities to the degree that power density is affected.

To demonstrate the effects of separator on rate capability of electrodes, a highly porous separator (Zeus®) was employed to compare with the most common separator; Celgard® 2400. In the present work, Celgard® 2400 was used in the most experiments. Celgard® 2400 consists of ~40 % porosity and is 25 μm thick. The pore size was determined to be ~ 200 nm by SEM analysis (Figure 5-6a). On the other hand, the Zeus® separator was ~20 μm thick and the porosity was >50 %. The average pore size is ~400 nm based on SEM observation (Figure 5-6b). It was believed that the different separator structural characteristics would affect cycling behavior, especially at high C-rate. However, the cells employing Zeus® separators frequently failed during cycling tests, especially at high current densities. The Figure 5-7 shows the typical conditioning cycles with Zeus® separators and with different electrode loadings, which were 1.2 mAh cm<sup>-2</sup> and 5.5 mAh cm<sup>-2</sup>, respectively. The highly porous Zeus® separator works well with

1.2 mAh cm<sup>-2</sup> electrode while it causes cell failure during the conditioning cycles with the 5.5 mAh cm<sup>-2</sup> electrodes, especially when current density was increased (>0.139 mA cm<sup>-2</sup>). This may indicate that the Zeus® separator could not block the Li moss when the current density was higher than ~0.139 mA cm<sup>-2</sup>. Consequently, it might be true that an alternative separator with superior mechanical properties and high ionic conductivity, such as a ceramic electrolyte, is ultimately necessary to endure high current flow for long cycle life. The ceramic electrolyte, LLZO, is discussed in Chapter 6.

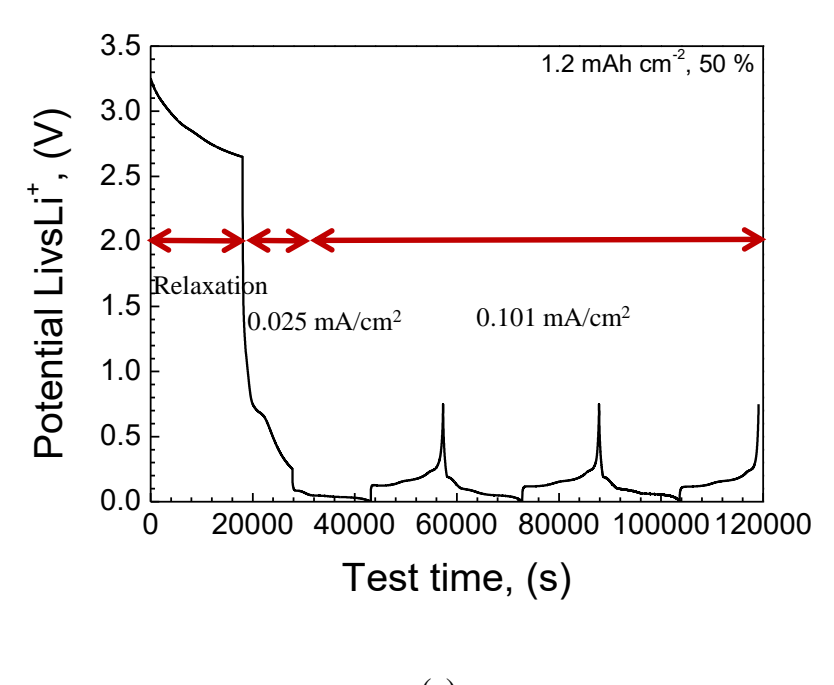


(a)



(b)

Figure 5-6: SEM images of (a) Celgard 2400® and (b) Zeus® separators.



(a)

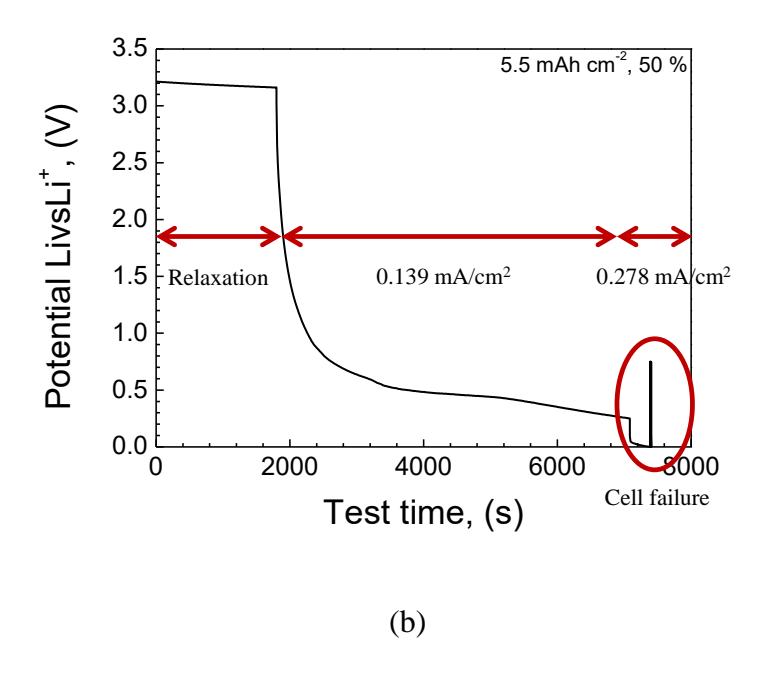


Figure 5-7: Typical preconditioning cycles with Zeus® separators and with different graphite electrode loadings, which were (a) 1.2 mAh cm<sup>-2</sup> and (b) 5.5 mAh cm<sup>-2</sup>, respectively

### 5.3 Cell impedance characterization

# **5.3.1 Polarization interrupt test**

To characterize the effects of tortuosity on graphite electrodes, the polarization interrupt tests [80] was conducted with conventional graphite electrodes (5.5 mAh cm<sup>-2</sup>, 50 % intrinsic open porosity) and HOH graphite electrodes (5.5 mAh cm<sup>-2</sup>, 45 % intrinsic open porosity and 5 % laser ablated porosity). The polarization interrupt tests were carried out on a free standing both conventional and HOH electrodes between 2 layers of Celgard® 2400 using a symmetric cell (Figure 5-8). The concentration gradient was produced by applying a constant current. Subsequently, the current was stopped, and the potential change was recorded. This potential change is produced by a redistribution of Li<sup>+</sup> and PF<sub>6</sub><sup>-</sup> through the porous electrodes and separators. The results of both cells with 5.5 mAh cm<sup>-2</sup> loading showed a linear slope line after stopping the applied current, and the potential slope (~-1.57 x 10<sup>-4</sup> V s<sup>-1</sup>) of HOH electrode was lower than that of the conventional electrode (~-1.24 x 10<sup>-4</sup> V s<sup>-1</sup>)(Figure 5-8). Since the slope depends on the transportation of ions back to the equilibrium state via porous medium, these data indicate that the internal resistance of the HOH electrode is lower than conventional electrode.

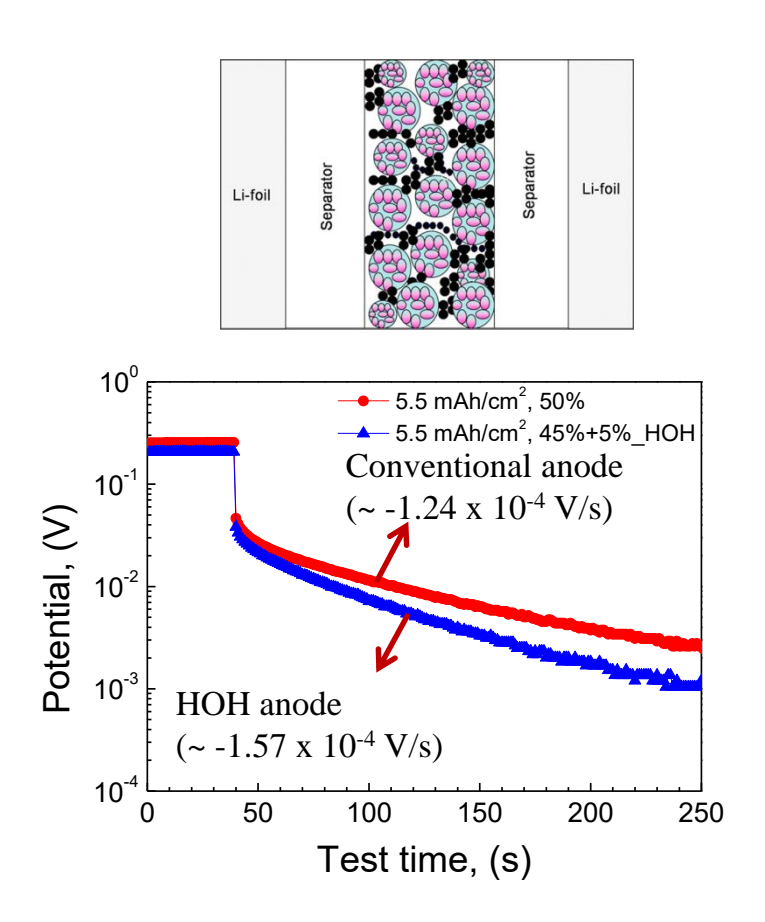


Figure 5-8: Galvanostatic polarization, followed by interrupt and relaxation test (HOH *vs* Conventional electrode with 5.5 mAh cm<sup>-2</sup> and 50 %), and the schematic of symmetric cells for polarization interrupt [80].

# 5.3.2 Transmission line method (TLM) and EIS characterization

Ogihara *et al.*[83] estimated the resistance of Li-ion inside the porous electrodes using the TLM based EIS-symmetric cell (SC) technique. Based on TLM model for cylindrical pores, the overall impedance is expressed in *Eq.* 2-6 for a non-faradaic and *Eq.* 2-7 for faradaic process [83]. When each numerical parameter is provided, the Nyquist plots exhibit linear behavior in the high frequency range, regardless of faradaic and non-faradaic models (Figure 5-9). Thus, the

linear slope region can be interpreted as a mass transport resistance without the effects of charge transfer resistance. Mass transport resistance values can be calculated based on the TLM model. According to the non-faradaic (Eq. 2-6) and faradaic (Eq. 2-7) TLM models, the impedance of the real part ( $Z_{re}$ ) and impedance of the imaginary parts ( $Z_{im}$ ) can be shown with the following relationships when  $\omega$  go to 0 in a non-faradaic process (Eq. 5-1 and 5-2), and in faradaic process (Eq. 5-3 and 5-4) [79,83].

$$Z_{re} = \frac{R_{ion}}{3} \qquad (Eq. 5-1)$$

$$Z_{im} = \frac{1}{\omega c_{dl}} \qquad (Eq. 5-2)$$

where  $R_{ion}$  is resistance of electrolyte-filled pores in porous electrode (mobility of Li-ion),  $C_{dl}$  is total electric double layer capacitance.

$$Z_{re} = \frac{R_{ion}}{3} + R_{ct} \qquad (Eq. 5-3)$$

$$Z_{im} = 0$$
 (Eq. 5-4)

where  $R_{ct}$  is charge transfer resistance.

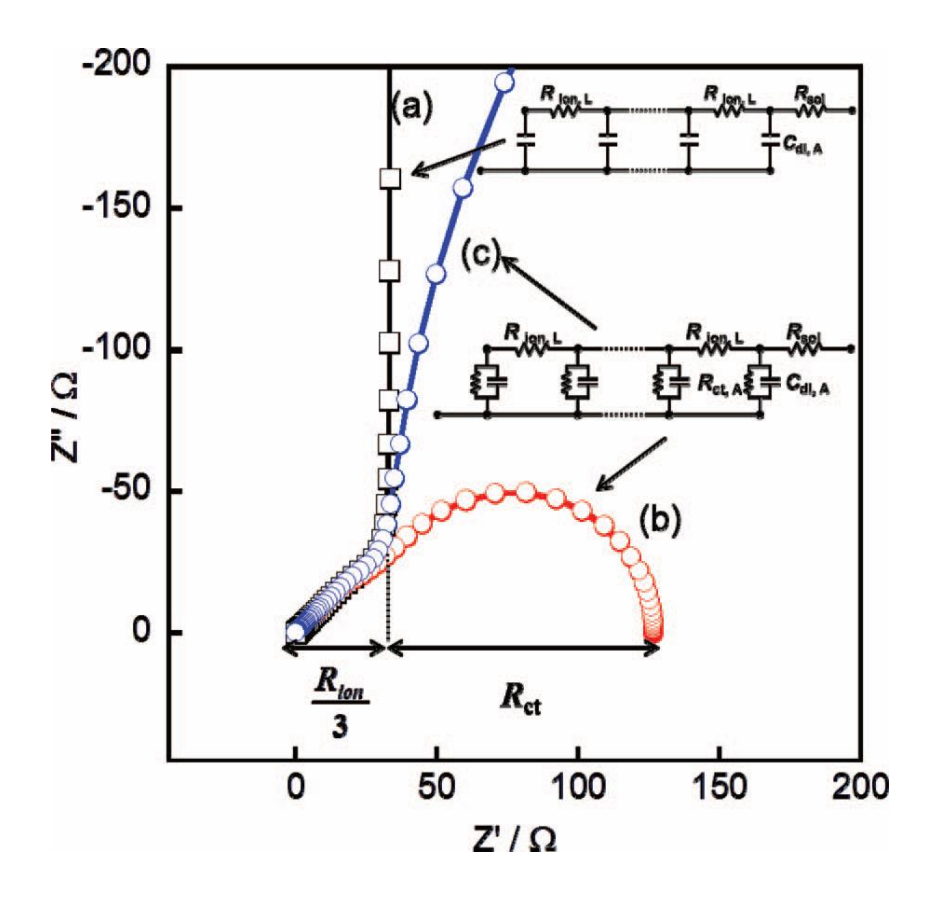
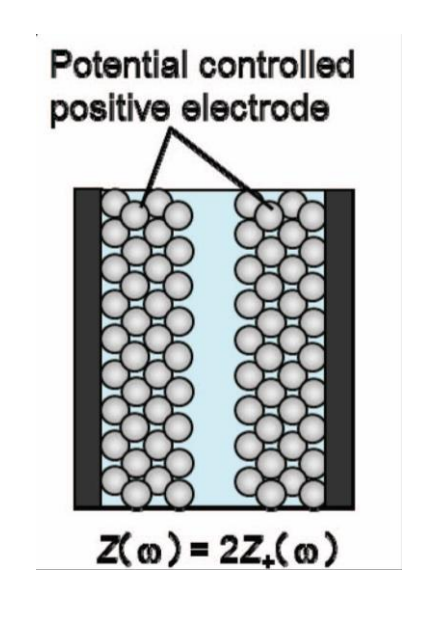


Figure 5-9: Simulated Nyquist plots for a cylindrical pore in an electrode with different models. (a) Non-faradaic, (b) faradaic with low charge transfer resistance, and (c) is faradaic with high charge transfer resistance [83].

### 5.3.2.1 Reliability of TLM based EIS-SC technique

To demonstrate the reliability of TLM based EIS-SC method, EIS test was conducted with using electrodes with various loadings (Figure 5-10). The symmetric cell was fabricated with SOC 0 % electrodes after preconditioning cycles to form a stable SEI layer (Figure 5-10a). The two different loading electrodes were selected to compare the effects of loading. The loadings for graphite electrodes were 1.2 mAh cm<sup>-2</sup> and 5.5 mAh cm<sup>-2</sup>, respectively, and the open porosity was fixed as 50 %. As seen in Figure 5-10bc, both SC with different loadings show a linearly

sloped region at the higher frequencies and a linear tale at lower frequencies. This behavior is consistent with non-faradaic model of Ogihara *et al*[83]. Although graphite is a non-blocking electrode, the charge transfer reaction was not observed in the frequency range used. Therefore, the ionic resistance in porous graphite electrode can be interpreted by the non-faradaic model. The SC with 1.2 mAh cm<sup>-2</sup> electrode had less resistance by ~65 % compared to 5.5 mAh cm<sup>-2</sup> of the same porosity (Figure 5-10bc). Since the 5.5 mAh cm<sup>-2</sup> electrode consists of longer and more tortuous Li-ion diffusion paths, the internal resistance should be higher than that of the thin electrodes (1.2 mAh cm<sup>-2</sup>). In addition, it should be pointed out that their different bulk resistances in the high frequency region. The bulk resistances are mainly from the electrolyte-filled porous separator. Therefore, the bulk resistances ideally have the same values due to use the same separator and electrolyte. However, this resistance also includes peripheral componentry such as the cables and stainless steel 304 electrodes, which can account for the 1 ohm variance.



(a)

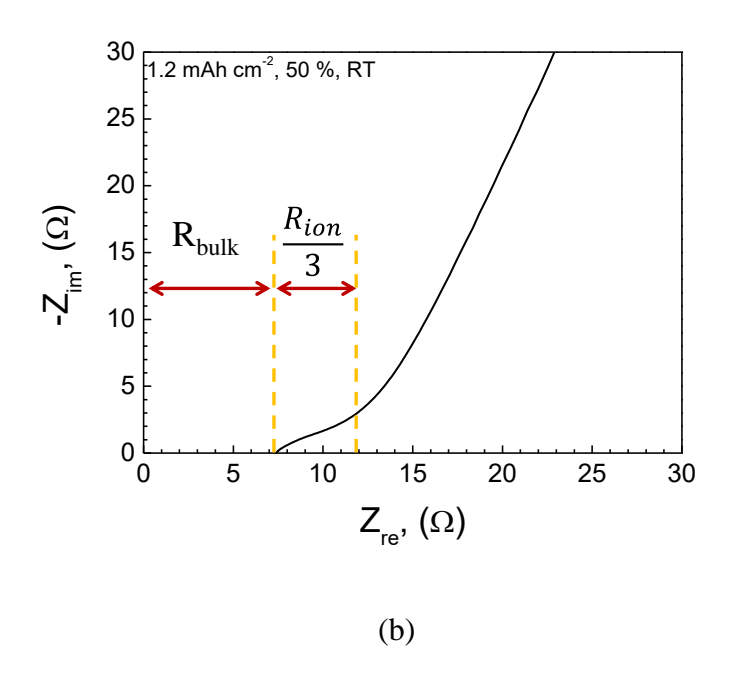


Figure 5-10: (a) Schematic representation symmetric cell (SC)[83], Nyquist plots after TLM-EIS-SC tests with (b)  $1.2 \text{ mAh cm}^{-2}$  and 50 % and (c)  $5.5 \text{ mAh cm}^{-2}$  and 50 % SFG6 symmetric cells.

Figure 5-10 (cont'd).

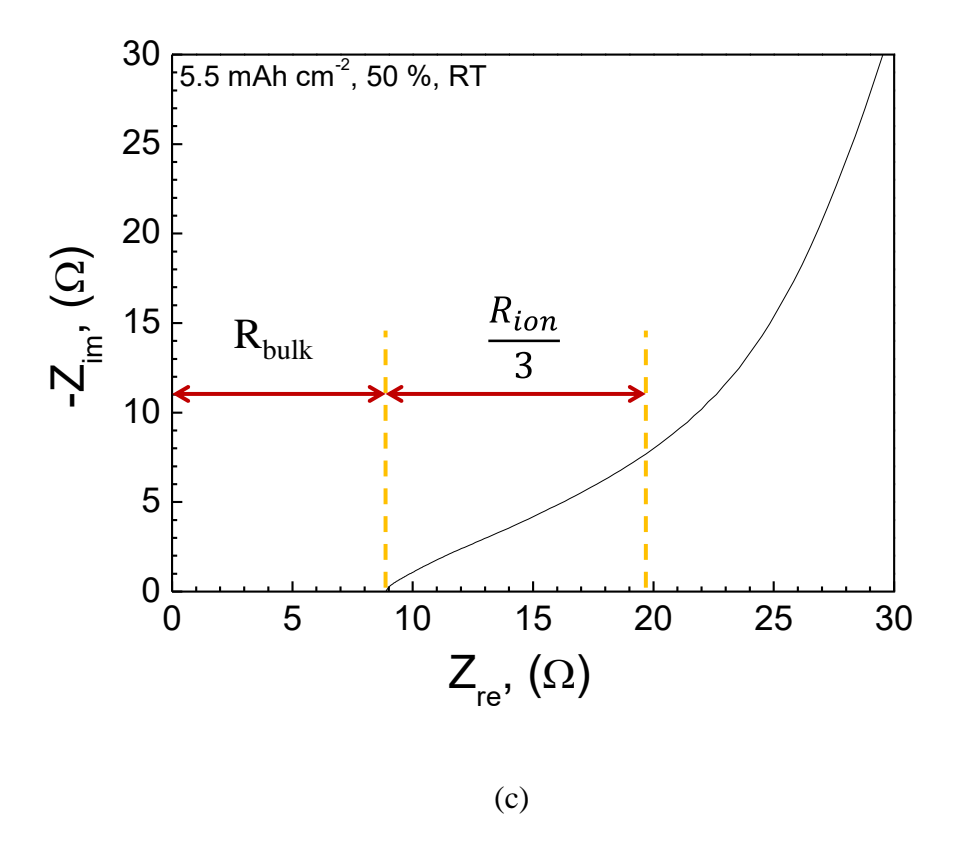


Figure 5-11 shows the temperature dependence of the Nyquist plots of fully delithiated conventional graphite electrodes (SOC 0 %) with 5.5 mAh cm<sup>-2</sup> and 50 %. The temperature range was from RT to 55 °C. In all temperature ranges, the Nyquist plots showed the same behavior. Figure 5-11 clearly shows the decreasing trend for both the bulk resistance ( $R_b$ ) and the resistance of the electrolyte-filled pores ( $R_{ion}$ ) as a function of temperature increase. Since the Li-ion mobility is proportional to the temperature increase, this trend is well matched with predicted behavior. Based on the loading and temperature dependence tests, EIS-SC based on the TLM technique can be adopted to measure the resistance of electrolyte-filled pores.

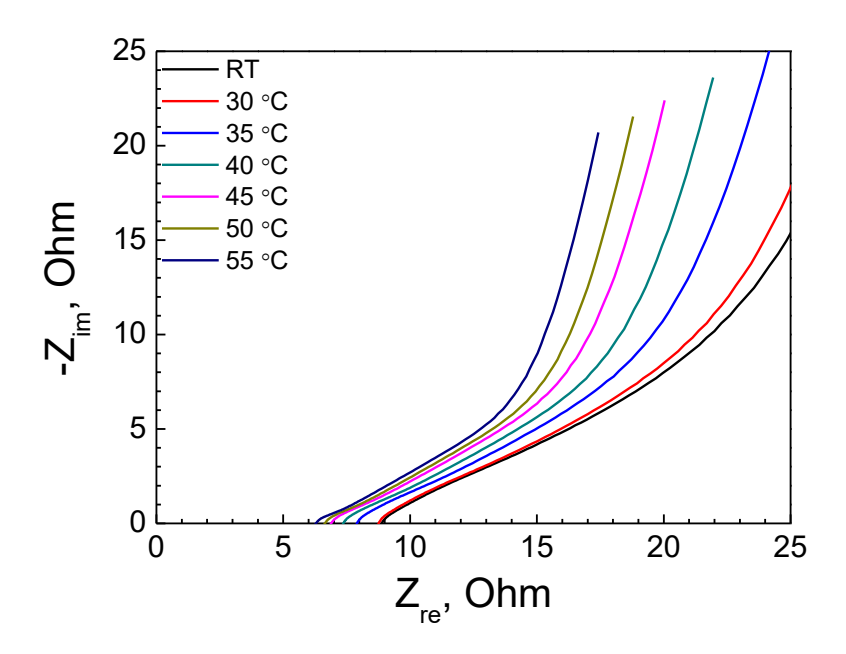


Figure 5-11: Nyquist plots for symmetric cells with two graphite electrodes at SOC 0 %. The loading of 5.5 mAh cm<sup>-2</sup> and porosity of 50 % conventional graphite electrodes were used.

### 5.3.2.2 Comparison the internal resistance of HOH electrodes vs conventional electrodes

Figure 5-12 shows Nyquist plots of both HOH and conventional porous electrodes with 5.5 mAh cm<sup>-2</sup> and 50 % using the EIS-SC technique. The HOH electrode also exhibits a linearly sloped region at the high frequencies. The imaginary impedance increases at low frequency and the plot is nearly a vertical line. The tale at low frequencies is ideally a vertical line, which indicates electrical blocking behavior but they showed a low angle slope (Figure 5-11). The slope of this region can be attributed to leakage current effect. Since the HOH electrodes also exhibited non-faradaic behavior, the Li-ions transport resistance in porous electrode can be estimated by Eq. 5-1. The resulting resistance showed  $\sim 35 \%$  lower resistance compared to conventional electrodes

with the same loading and open porosity. This trend is consistent with the rate mapping and polarization interrupt tests.

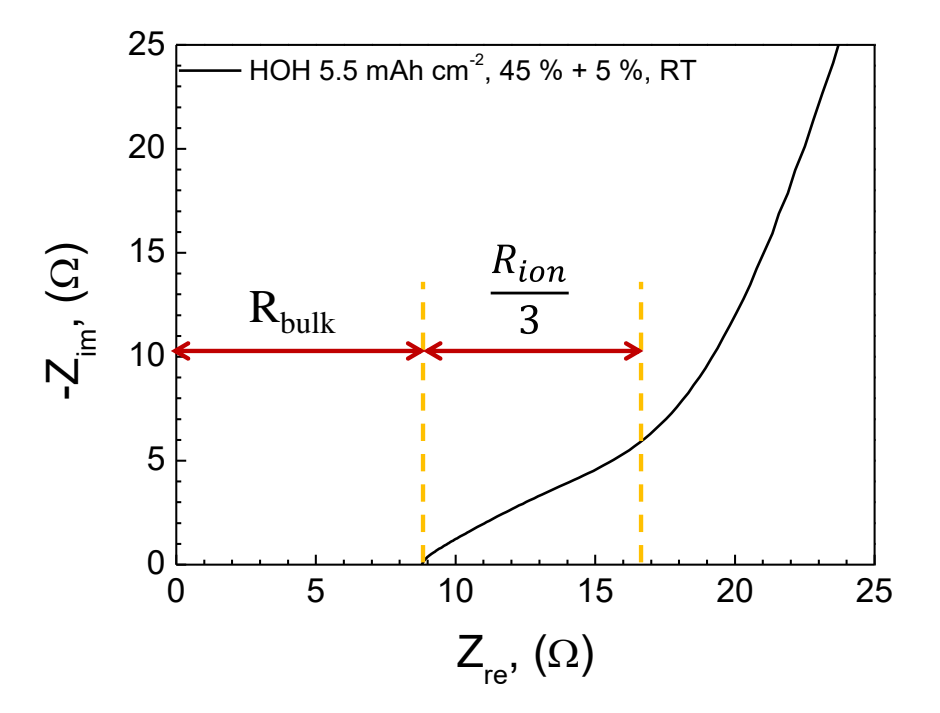


Figure 5-12: Nyquist plots after TLM-EIS-SC test with HOH symmetric cell (5.5 mAh cm $^{-2}$  and 45 + 5 %).

### 5.4 Summary

In Chapter 5, the solid-state Li diffusivity of SFG6 grade electrode was characterized by GITT. The measured Li diffusivity range was consistent with previous work (10<sup>-7.5</sup>-10<sup>-9.5</sup> cm<sup>2</sup> s<sup>-1</sup>)[111]. In addition, the surface area of fabricated electrode showed ~60 % lower values compared to that of particles due to pore occlusion likely from the polymer binder and calendaring.

The rate mapping tests were conducted to measure the effects of loading. As was expected, high loading electrode (5.5 mAh cm<sup>-2</sup>) showed ~55 % lower capacity compared to that of low loading electrode (1.15 mAh cm<sup>-2</sup>) at 1/3 C-rate. It can be attributed to different current density requirements dependent on different loadings at the same C-rate.

The rate capability of an HOH electrode was compared with that of a conventional electrode. Based on rate mapping tests with different loading electrodes, the internal resistance of electrolyte-filled pores seems to be significantly increased between 4 mAh cm<sup>-2</sup> and 5.5 mAh cm<sup>-2</sup>. When the electrode loading was 5.5 mAh cm<sup>-2</sup>, an HOH electrode, which has 45 % intrinsic open porosity and 5 % laser ablated open porosity, showed 65 % and 120 % higher rate capability compared to the conventional electrodes of the same loading and porosity at 1/3 C and 1/2 C-rate, respectively. The polarization interrupt test and TLM-EIS-SC tests demonstrated that HOH electrodes have lower internal resistance compared to conventional electrodes. However, the capacities retention of both types of electrodes approaches zero at high C-rate (>1 C-rate). Also, it was shown that solid-state Li diffusivity causes concentration polarization, which leads premature potential cut-off when the rate is >1 C-rate. In conclusion, HOH electrodes can improve the rate capability and ameliorate safety concerns by suppressing concentration

polarization. However, when the C-rate is beyond a critical level (~1 C-rate), the relatively slow solid-state Li diffusion rate can dominate the internal resistance.

# 6 The effect of microstructure on the mechanical properties of hot-pressed cubic $Li_7La_3Zr_2O_{12}$

As a result of increased demands for higher energy and safety the novel hybrid cell design including LLZO ceramic electrolyte was proposed in this study. To be used in this situation the solid electrolyte must meet several important requirements [47]. These include: 1) high ionic conductivity with low electronic conductivity, 2) chemical stability against the Li negative electrode and positive electrode and 3) good mechanical properties. Of the possible Li-ion conducting solid electrolytes cubic,  $\text{Li}_7\text{La}_3\text{Zr}_2\text{O}_{12}$  (LLZO) is a potential candidate as a result of its high ionic conductivity ( $\sim 10^{-4}$  to  $10^{-3}$  S cm<sup>-1</sup> [54]) and stability with Li [52]. There have been many investigations on the ionic conductivity of LLZO [50-52]. The effects of microstructure (e.g., porosity and grain size) on the ionic conductivity of LLZO are well documented [128]. In contrast, there have been very few investigations focusing on the mechanical properties of LLZO and none reported on the effects of microstructure on mechanical behavior [129].

As consequence, it is the purpose of this Chapter to investigate and relate the mechanical properties such as hardness and fracture toughness of hot-pressed Al-substituted LLZO to the microstructure. In addition, the ionic conductivity will be measured. The correlation between ionic conductivity, hardness, fracture toughness and microstructure (porosity and grain size) will be reported. This information is needed if cubic LLZO is to be used as a Li-ion conducting electrolyte in a solid-state battery and/or hybrid cell design which was proposed in this study.

#### 6.1 LLZO ceramic electrolyte characterization

# **6.1.1 Density of LLZO**

From Table 6-1, it is observed that as the hot-pressing time increased, the relative density increased, reaching the maximum value of 98 % at 240 min. In addition, it can be seen that a minimum hot-pressing time of about 60 min is needed to achieve relative densities above 95 %, where the porosity typically transitions from open to closed [130-132].

Table 6-1: It presents the information of hot-pressed LLZO pellets as changing hot-pressing time.

Hot-press time (min)	30	60	90	240
Relative density (%)	85	95	96	98
Grain size (µm)	$2.7 \pm 1.68$	$3.2 \pm 1.87$	$3.5 \pm 1.83$	$3.7 \pm 1.84$
Lattice parameter (Å)	13.023	12.981	12.978	12.964

#### **6.1.2** Phase characterization

The X-ray diffraction patterns of the LLZO calcined powder, the hot-pressed LLZO as a function of hot-pressing time, and the reference pattern for cubic LLZO are shown in Figure 6-1. A comparison of the X-ray diffraction patterns for the calcined and hot-pressed samples with that for the reference pattern suggests that the pellets were predominantly cubic LLZO with no observable second phases except a small amount (~0.5 wt.%) of pyrochlore (La<sub>2</sub>Zr<sub>2</sub>O<sub>7</sub>) that was present only in the sample hot-pressed for 60 min. However, closer inspection of Figure 6-1 reveals that the triple peaks between 50-53° two-theta of the calcined powder and the hot-pressed sample for 30 min show a slightly right-skewed shape. According to previous studies, a skewed peak shape can result from the presence of some tetragonal phase due to a Li content above that

needed to form the pure cubic phase [56]. It is likely that presence of the tetragonal phase in these calcined and sample hot-pressed for 30 min samples is a due to the incomplete evaporation of the 10 wt.% excess Li precursor that was intentionally added to compensate for Li loss during high temperature processing. At longer hot-pressing times when the excess Li has evaporated only the pure cubic phase is exhibited (Figure 6-1).

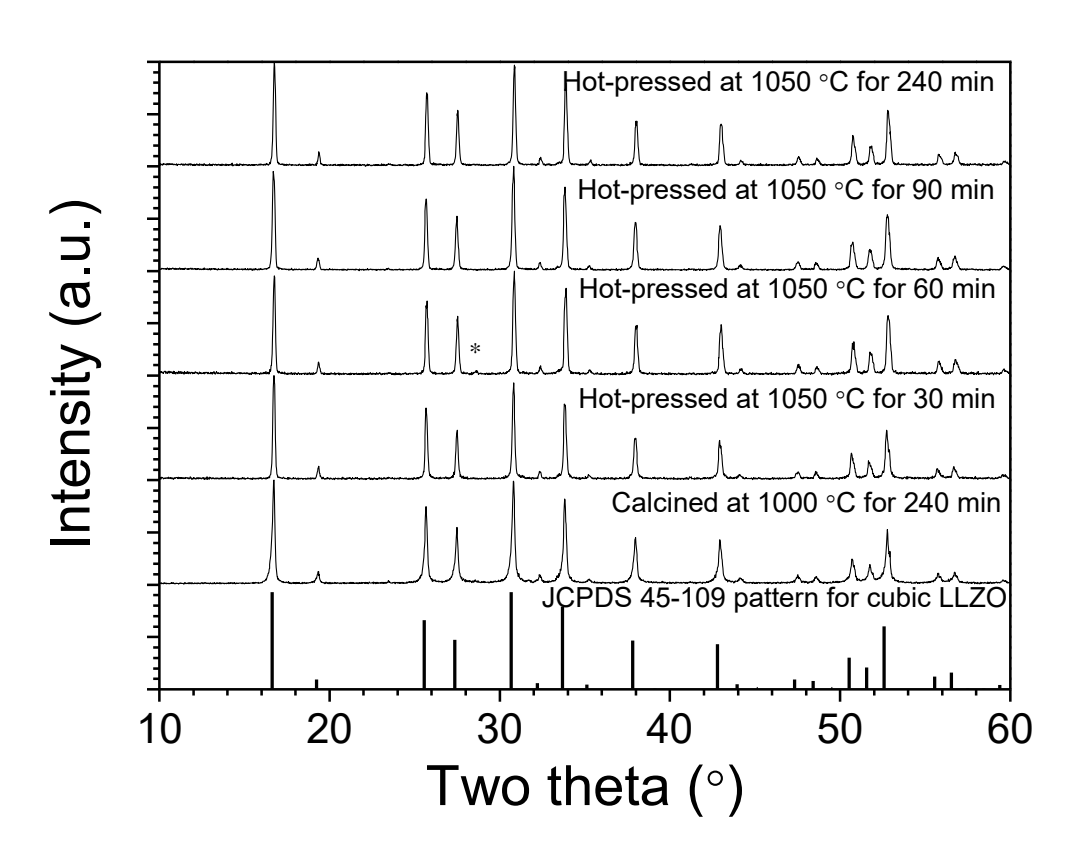


Figure 6-1: X-ray diffraction patterns of  $Li_{6.19}Al_{0.27}La_3Zr_2O_{12}$  calcined powder and hot-pressed pellets pressed for 30, 60, 90, and 240 min at 1050 °C. \* Pyrochlore ( $La_2Zr_2O_7$ )[133]

#### **6.1.3 Micro structure of LLZO**

Fracture surfaces of the hot-pressed LLZO samples as a function of relative density are shown in Figure 6-2. From Figure 6-2, several points are noted. First, in agreement with density measurements, it is seen that the relative density increased (porosity decreased) with increasing hot-pressing time. Second, the dominant fracture mode changed from inter to intragranular with increased relative density. It can be seen that the 85 % relative density (hot-pressed for 30 min) sample exhibited almost 100 % intergranular fracture (Figure 6-2a) whereas intragranular fracture was the primary fracture mode at above 95 % relative density (hot-pressed for 60 min, Figure 6-2b). At the highest relative density of 98 % (hot-pressed for 240 min, Figure 6-2d), the fracture mode was almost entirely intragranular.

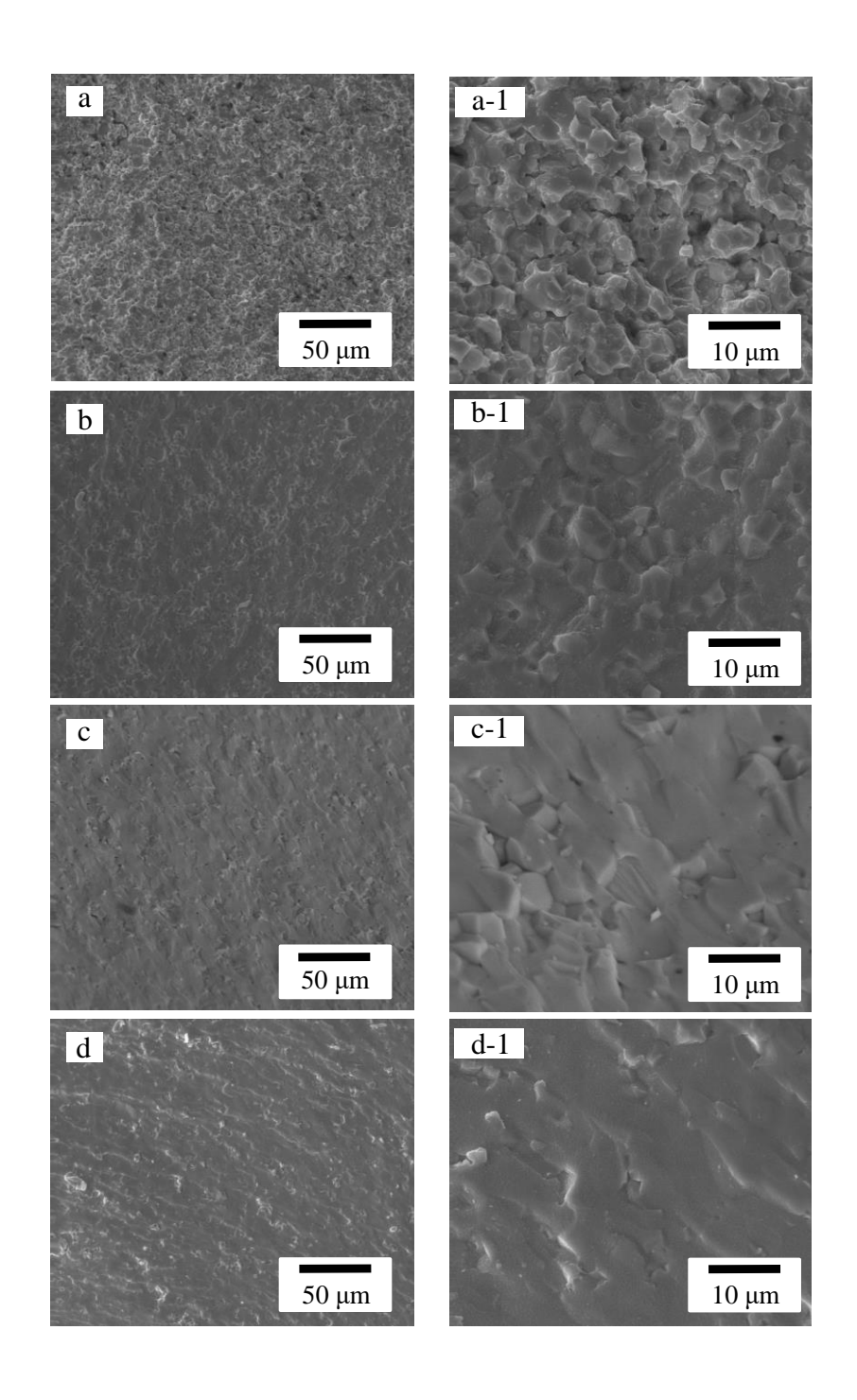


Figure 6-2: Fracture surface of  $Li_{6.19}Al_{0.27}La_3Zr_2O_{12}$  hot-pressed for: (a) 30 min, (b) 60 min, (c) 90 min, and (d) 240 min. The relative densities are indicated in top right of each image [133].

Microstructures of the thermally etched hot-pressed LLZO samples as a function of relative density are shown in Figure 6-3. From Figure 6-3, several points are noted. First, the majority of the porosity is located at the grain boundaries and decreases with increasing pressing time, which is in agreement with the density measurements and fracture surface micrographs (Figure 6-2). Second, the average grain size, determined using the average length between the major axis and minor axis is listed in Table 6-1. From Table 6-1, it is seen that the grain size increased with increasing pressing time (increased density). Because each hot-pressed sample contained a wide range of grains between  $\leq 1 \mu m$  to  $12 \mu m$  (Figure 6-3), a large standard deviation resulted (Table 6-1). Consequently, the grain size distribution was determined using *Eq.* 6-1 and plotted in Figure 6-4 for as a function of relative density (hot-pressing times).

$$GSD_{i,j,k} = \frac{n_{i,j,k}}{n_i + n_{j+} n_k}$$
 (Eq. 6-1)

where GSD is the grain size distribution (i = 0-2, j = 2-4, and  $k = 4-12 \mu m$ ) and n is the number of grains in a grain size range.

From Figure 6-4, it is observed that the fraction of 0-2  $\mu$ m grains decreased from 0.42 to 0.17, and the fraction of 4-12  $\mu$ m grains increased from 0.16 to 0.36 for the 85 % and 98 % relative density samples, respectively. This result is in good agreement with the average grain size measurements (Table 6-1), confirming that the grain size increased with increasing relative density (or hot-pressing time). The average grain size after hot-pressing (~2-4  $\mu$ m) is much smaller than those typically observed in conventionally sintered LLZO, which exhibit grain sizes in the range of ~20-200  $\mu$ m [128].

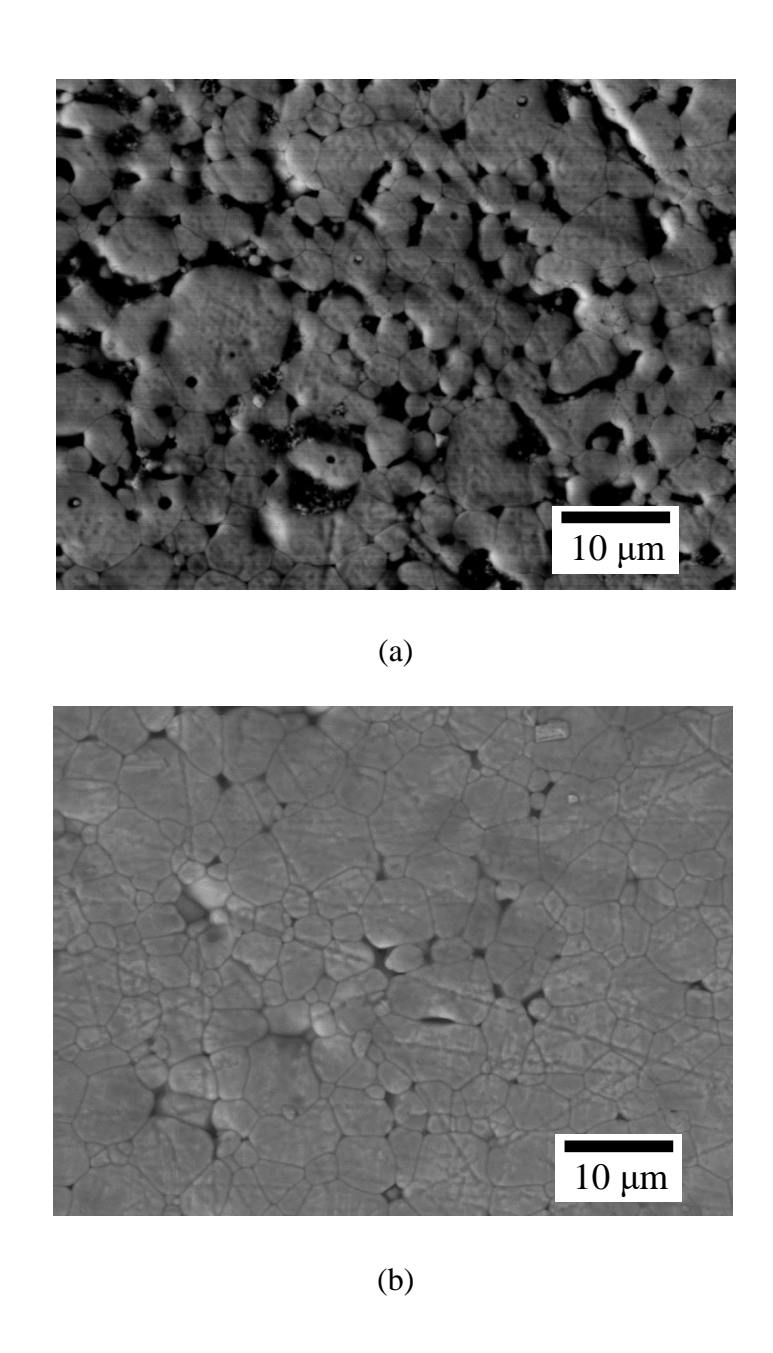
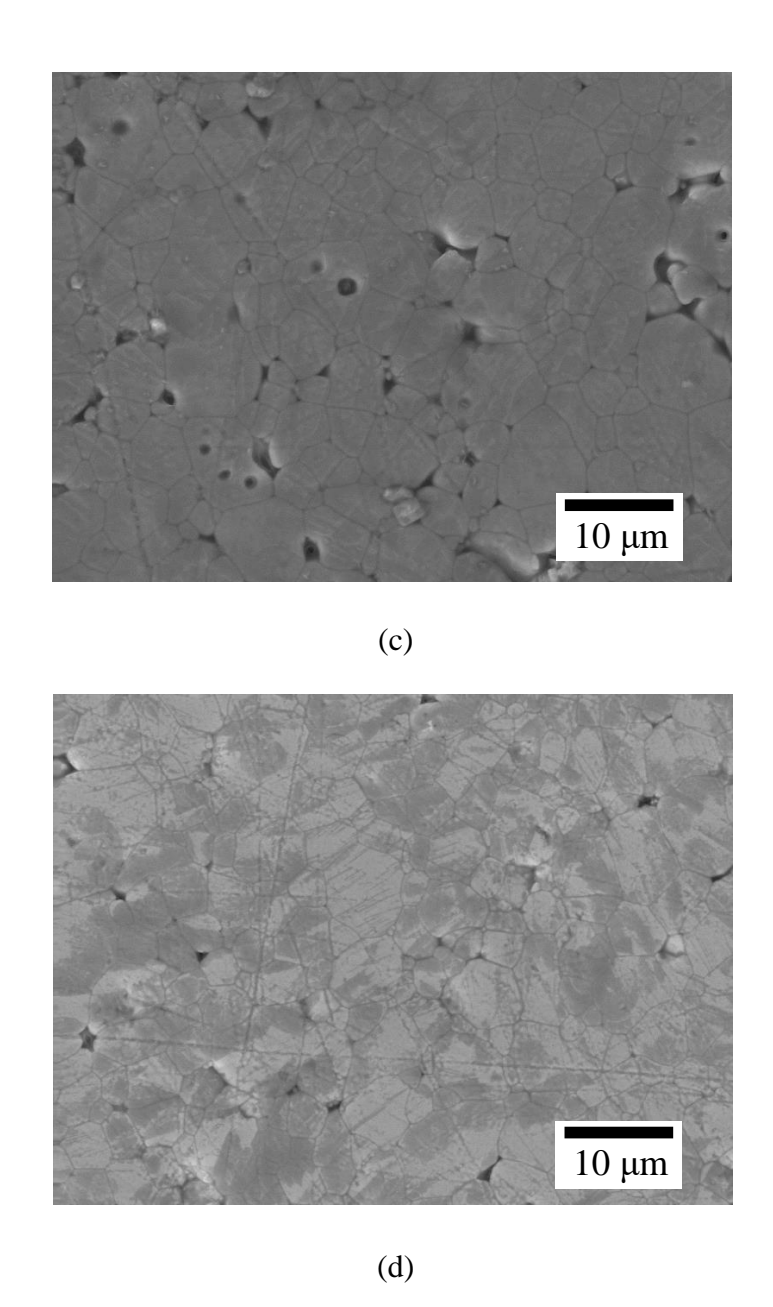


Figure 6-3:  $\text{Li}_{6.19}\text{Al}_{0.27}\text{La}_3\text{Zr}_2\text{O}_{12}$  hot-pressed pellets after thermal etching at  $700^{\circ}\text{C}$  for 30 min in air. The  $\text{Li}_{6.19}\text{Al}_{0.27}\text{La}_3\text{Zr}_2\text{O}_{12}$  pellets were hot-pressed at  $1050^{\circ}\text{C}$  for: (a) 30 min, (b) 60 min, (c) 90 min, and (d) 240 min. The relative densities are indicated in top right of each image [133].

Figure 6-3 (cont'd).



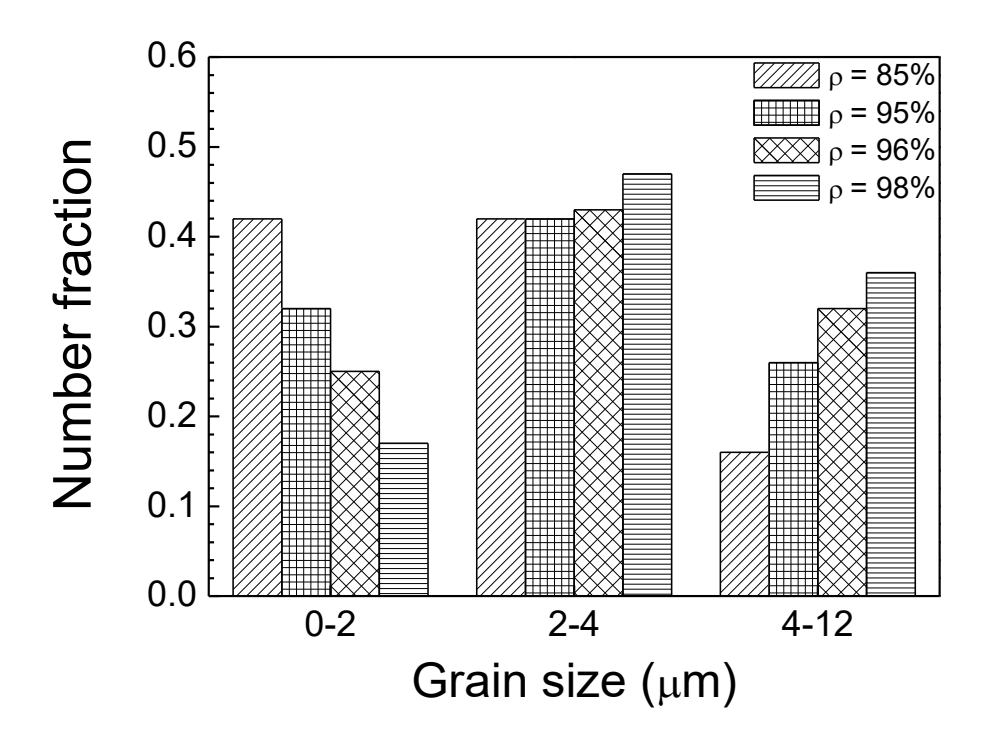


Figure 6-4: Grain size distributions of hot-pressed Li<sub>6.19</sub>Al<sub>0.27</sub>La<sub>3</sub>Zr<sub>2</sub>O<sub>12</sub> [133].

One important aspect of the microstructural characterization is that a change in fracture mode from inter to intragranular with increasing hot-pressing time was observed. This could be associated with microstructural variables such as the grain size and/or porosity at the grain boundaries or the grain boundary composition/cohesion. In general, an increase in grain size and/or decrease in porosity at the grain boundaries can lead to an increase in the percentage of intragranular fracture [134-136]. While a difference in grain size is observed, the maximum disparity is ~25%; the average grain size was 2.7  $\mu$ m and 3.7  $\mu$ m for the 85 %  $\nu$ s 98 % relative density samples, respectively. Thus, we do not believe the difference in grain size is responsible for the dramatic transition from inter to intragranular fracture when comparing the 85 % and  $\geq$ 95 % relative density samples. In a first approximation, we believe that the pores could act as stress

intensifiers, thus initiating cracks at the grain boundaries. Because the 85 % relative density sample had the highest fraction of intergranular porosity, intergranular fracture was the primary fracture mode. At 98 % relative density where the volume fraction of porosity was the lowest, intragranular fracture was dominant. It is also possible that the grain boundary composition/strength could increase with increasing hot-pressing time, though this cannot be verified at this time. In summary, it was observed that hot-pressing times of at least 60 min is required to obtain high density (>95 %) LLZO with relatively strong grain boundaries compared to the 85 % relative density sample.

## 6.2 Mechanical properties of LLZO

#### 6.2.1 Hardness of LLZO

The hardness of hot-pressed LLZO as a function of relative density is shown in Figure 6-5. The Vikcers hardness ( $H_v$ ) is shown by the open symbols while the nanoindentation hardness ( $H_n$ ) is shown by the closed symbols. From Figure 6-5, several important points are noted. First, both the  $H_v$  and  $H_n$  values increase with increasing relative density and gradually level off at high relative densities. For the nanoindentation, the increase in  $H_n$  with relative density is not as pronounced compared to the increase in  $H_v$  for the reasons explained below. Second, at the lowest relative density of 85%, the  $H_v$  is  $4.7 \pm 0.2$  GPa, which is about half the value for the  $H_n$  of  $8.1 \pm 0.8$  GPa at 95 % relative density. This difference diminishes ( $H_v$  is  $7.4 \pm 0.4$  GPa vs 9.3  $\pm$  0.5 GPa for  $H_n$ ) above a relative density of 96 % for both the  $H_v$  and  $H_n$ , which are nearly equal at 9.1 GPa.

The results of Figure 6-5 can be explained by the difference in microstructural variables (porosity and grain size) and measurement techniques ( $H_v$  and  $H_n$ ). In general hardness can be affected by porosity and grain size. Typically hardness decreases with increasing porosity and increasing grain size [137-139]. Since the average grain size was nearly the same (within 25 %) among all relative densities, we believe the main microstructural variable that influences the hardness is the porosity. In nanoindentation, the indent impression size was ~1  $\mu$ m or less. This is smaller than the average grain size (~2-4  $\mu$ m), thus each valid nanoindentation measurement was essentially in a LLZO single crystal. However, the 85 % relative density LLZO exhibited a lower average  $H_n$  compared to the  $\geq$ 95 % relative density samples. This could result from nanoindentations in the proximity of pores. Since the 85 % relative density LLZO consisted of more porosity than the other relative densities, it was more likely that there were more nanoindentations in the proximity of pores, which lowered the average hardness value. The large standard deviation in the  $H_n$  ( $\pm$  0.8 GPa) among all the relative densities measured for the 85 % samples most likely results from a non-uniform pore distribution within this sample.

For the case of  $H_{\nu}$ , the indent impression size was between 10-15 µm. This is bigger than the average grain size, thus the  $H_{\nu}$  can be affected by the intergranular porosity. It is expected that as the porosity decreases, the  $H_{\nu}$  should increase. According to the data in Figures 6-3 and 6-5, the  $H_{\nu}$  indeed increases as the relative density increases. Furthermore, additional proof that the  $H_{\nu}$  is influenced by the intergranular porosity is the increase in  $H_{\nu}$  with increasing density follows the change in fracture mode from inter to intragranular (Figure 6-2). From Figure 6-2, it is observed that at low relative density, the fracture mode is intergranular, implying relatively weak grain boundaries that decrease the hardness compared to the higher relative density samples. Additionally, as the relative density increases the fracture mode changes to

intragranular implying relatively stronger grain boundaries exhibiting relatively higher hardness compared to the 85 % relative density sample. At the highest relative density (98 %), where the fracture mode is almost entirely intragranular, the  $H_{\nu}$  should equal the  $H_n$  value since the effects of porosity and grain size are negligible. From Figure 6-5, it can be observed that indeed both values are about equal (~9.1 GPa).

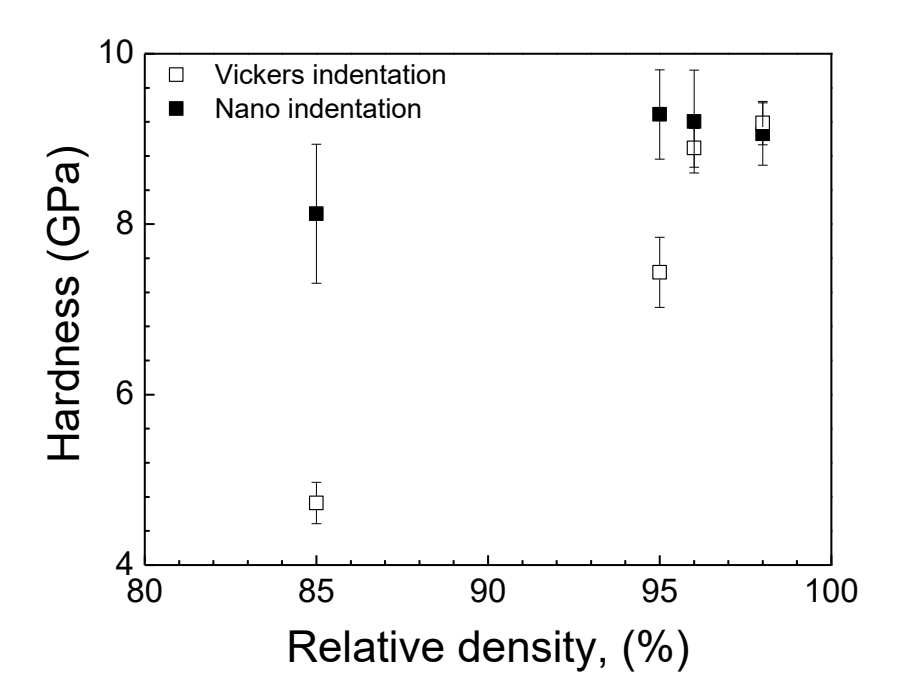


Figure 6-5:  $H_v$  and  $H_n$  of Li<sub>6.19</sub>Al<sub>0.27</sub>La<sub>3</sub>Zr<sub>2</sub>O<sub>12</sub> as a function of relative density [133].

It was shown by Sirdeshmukh *et al.*[140] that the  $H_{\nu}$  (measured on the (111) face) of several oxide based garnet single crystals can be correlated with lattice parameter. It was observed that  $H_{\nu}$  decreased linearly with an increase in lattice parameter. Sirdeshmukh *et al.*[140] suggested

that a smaller lattice parameter results in stronger interatomic binding and hence, higher hardness. The  $H_{\nu}$  values  $\nu s$  lattice parameter for the single crystal oxide based garnets from Sirdeshmukh et al.[140] are plotted in Figure 6-6. Also Figure 6-6 includes the  $H_{\nu}$  for the highest relative density (98 %) LLZO. It should be noted that from Figure 6-5 that this value is equivalent to the  $H_{n}$ . The lattice parameter for this material determined by Rietveld refinement is 12.964 Å. From Figure 6-6, it is observed that the measured  $H_{\nu}$  of LLZO is in good agreement with the predicted value. These results suggest that the correlation between hardness and lattice parameter is similar to other garnets, thus the single crystal hardness of LLZO was estimated to be 9.1 GPa.

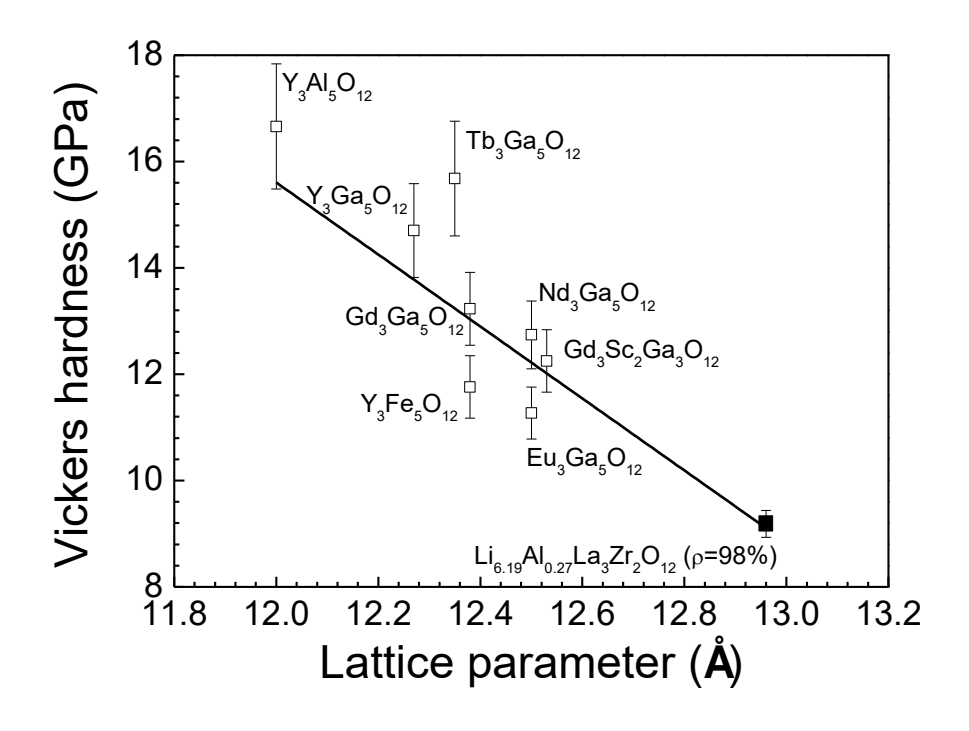


Figure 6-6:  $H_v$  vs lattice parameter for single crystalline garnets from the literature (open squares)[140] and the value for  $Li_{6.19}Al_{0.27}La_3Zr_2O_{12}$  from this work (closed square) [133].

## **6.2.2 Fracture toughness of LLZO**

The  $K_{IC}$  of hot-pressed LLZO as a function of relative density is shown in Figure 6-7. From Eq. 2-11 [90], it is seen that a value of E is required to determine  $K_{IC}$ . It was observed that E varied from ~135 GPa for the 85% relative density sample to ~140 GPa for denser samples ( $\geq$ 95%). The E values for the higher relative density samples are in agreement with the experimental value of E ~150 GPa determined using resonant ultrasonic spectroscopy for the 97 % relative density  $\text{Li}_{6.24}\text{Al}_{0.24}\text{La}_3\text{Zr}_2\text{O}_{11.98}$  sample [129]. From Figure 6-7, it can see that the  $K_{IC}$  decreased with increasing relative density. The  $K_{IC}$  values are  $2.37 \pm 0.1$  MPa $\sqrt{\text{m}}$  and  $0.97 \pm 0.1$  MPa $\sqrt{\text{m}}$  for the 85 % and 98 % relative density samples, respectively. These values are within the range typically exhibited by polycrystalline ceramics ~2-5 MPa $\sqrt{\text{m}}$  [129,141].

The predicted  $K_{IC}$  value for the 97 % relative density sample was ~1.11 MPa $\sqrt{m}$  (Figure 6-7). This value is in good agreement with the  $K_{IC}$  value of ~1.25 MPa $\sqrt{m}$  for a sample of the same relative density (97 %), similar composition (Li<sub>6.24</sub>Al<sub>0.24</sub>La<sub>3</sub>Zr<sub>2</sub>O<sub>11.98</sub>), but slightly larger grain size of ~5 µm [142]. The decrease in  $K_{IC}$  with increasing density could be a result of the change in grain size and/or the amount of porosity at the grain boundaries. It has been observed that the  $K_{IC}$  is independent of grain size for cubic oxides over the grain size range investigated in this study [143-144]. Thus, the difference in grain size of LLZO cannot explain the decrease in  $K_{IC}$  with increasing density.

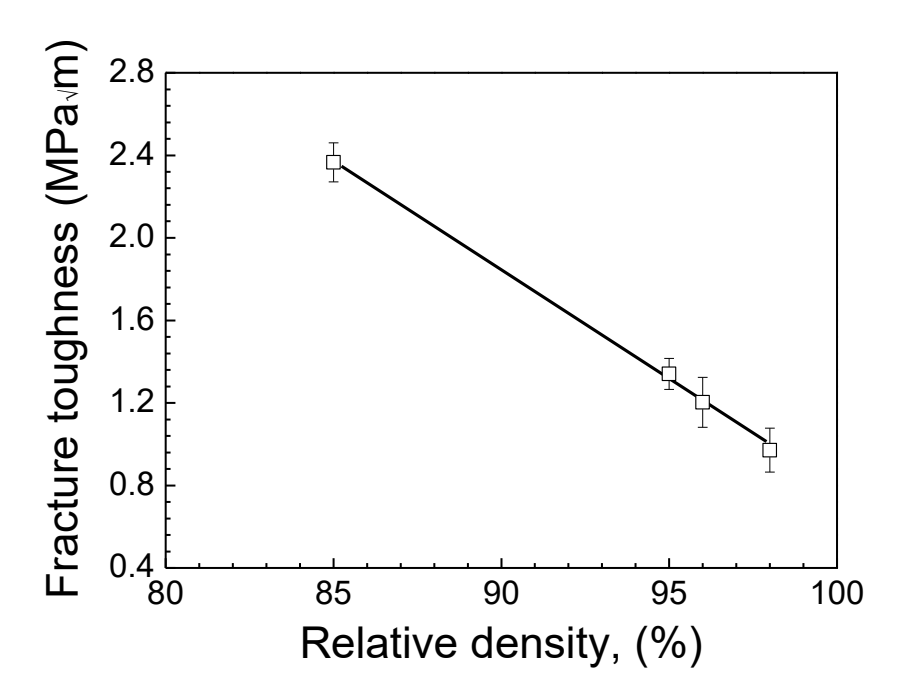


Figure 6-7: Fracture toughness of Li<sub>6.19</sub>Al<sub>0.27</sub>La<sub>3</sub>Zr<sub>2</sub>O<sub>12</sub> as a function of relative density [133].

Examination of the crack propagation path from the corner of the Vickers indents (Figure 6-8) in the 85 % and 98 % relative density samples clearly shows different fracture modes. For the sample with the 85 % relative density, the crack propagation path is primarily intergranular, whereas for the sample with 98 % relative density, the crack propagation path is mainly intragranular. Similar trends were observed on the fracture surfaces shown in Figure 6-2. At 85 % relative density, the fracture mode was intergranular whereas at 98 % relative density, it was predominately intragranular. We believe, the relatively high volume fraction of intergranular porosity (Figure 6-3) in the 85 % relative density sample can explain why the primary fracture mode is intergranular. Typically, intergranular porosity is correlated with relatively weak grain boundaries [135]. Thus, the weak grain boundaries deflect the cracks out of the plane of

maximum driving force and hence, require more energy to propagate compared to the samples exhibiting strong grain boundaries where intragranular fracture was observed [145].

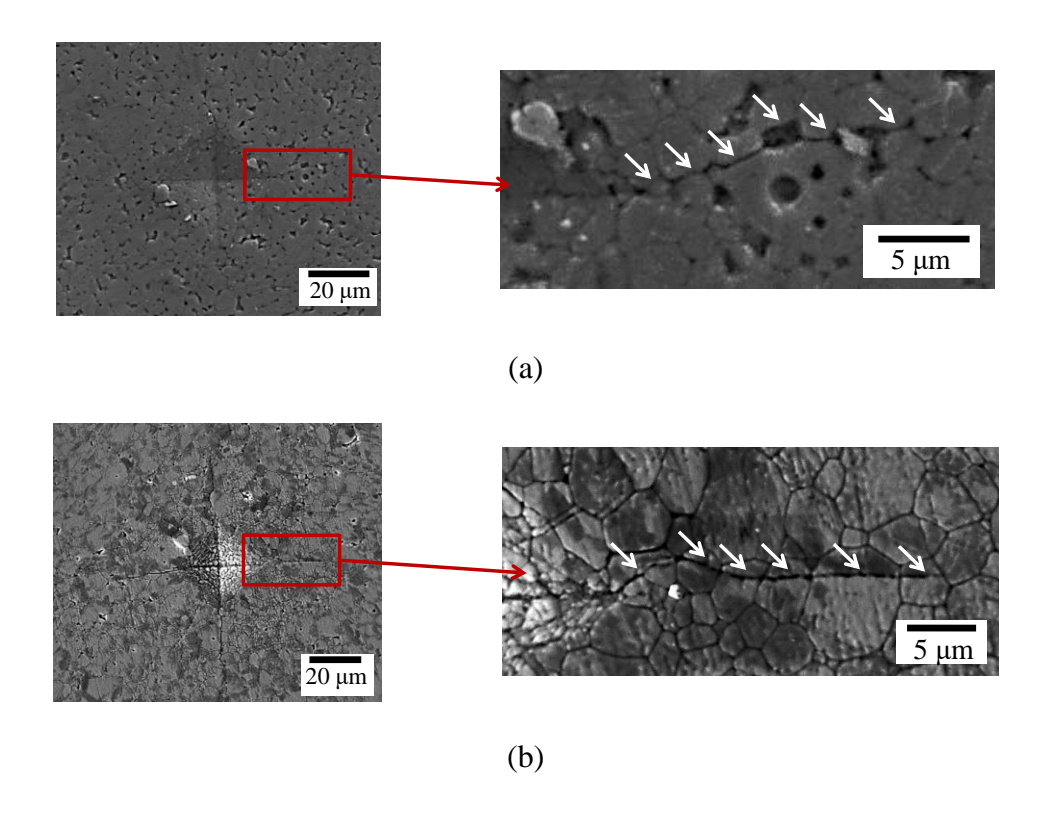


Figure 6-8: The Vickers indentation crack propagation path trajectories for (a) relative density of 85 % and (b) relative density of 98 %. Arrows point to crack the propagation path in each grain [133].

From the  $K_{IC}$  values for LLZO, the fracture surface energy ( $\gamma$ ) can be determined using Eq. 6-2 [135,137-139]:

$$\gamma = \frac{K_{IC}^2}{2E} \qquad (Eq. 6-2)$$

Using values of  $K_{IC} \sim 0.97$  MPa $\sqrt{m}$  and  $E \sim 140$  GPa into Eq. 6-2 yields a  $\gamma \sim 3$  J m<sup>-2</sup>. This value is in very good agreement with  $\gamma$  values of  $\sim 0.5$  to 3 J m<sup>-2</sup> commonly exhibited by single crystal ceramics [135]. This result suggests that the  $K_{IC}$  values for high relative density (98 %) LLZO

sample measured in this study is likely approaching the single crystal  $K_{IC}$  values. Using values of  $K_{IC} \sim 2.37$  MPa $\sqrt{m}$  and  $E \sim 135$  GPa for LLZO with 85% relative density in Eq. 6-2 yields a  $\gamma \sim 21$  J m<sup>-2</sup>. This value is within the range typically exhibited by polycrystalline ceramics (10-50 J m<sup>-2</sup>)[135].

# 6.3 Ionic conductivity of LLZO

The logarithm of total ionic conductivity of hot-pressed LLZO as a function of relative density is shown in Figure 6-9. From Figure 6-9, it is observed that the total ionic conductivity increases with increasing relative density. This trend is typically observed in LLZO and is usually associated with a decrease in the grain boundary resistance [146]. The decrease in the grain boundary resistance component could be a result of a change in the nature of the grain boundary as suggested by David *et al*[73]. At 85 % relative density, the total ionic conductivity is 0.0094 mS cm<sup>-1</sup> and increases to 0.34 mS cm<sup>-1</sup> for the 98 % relative density sample. The value of 0.34 mS cm<sup>-1</sup> is in good agreement with the upper values of total conductivity for Al-substituted LLZO of similar composition (0.02 to 0.5 mS cm<sup>-1</sup>)[73,147]. Extrapolation of the curve in Figure 6-9 yields a total ionic conductivity of ~0.4 mS cm<sup>-1</sup>, which is in excellent agreement with previously reported bulk conductivity values [56].

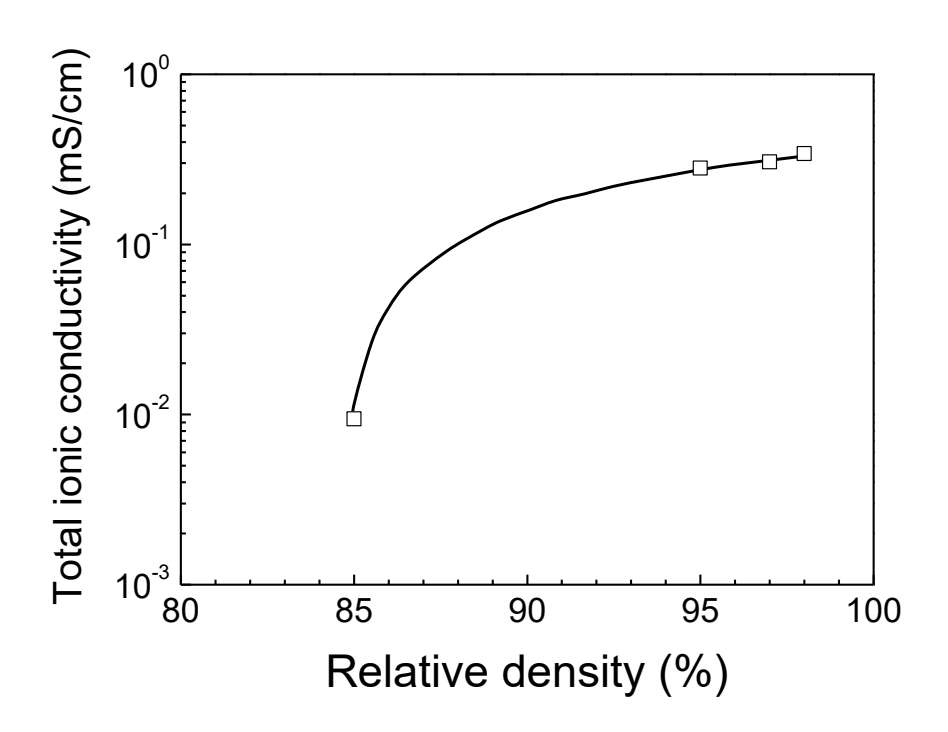


Figure 6-9: Total ionic conductivity of  $Li_{6.19}Al_{0.27}La_3Zr_2O_{12}$  as a function of relative density [133].

One of the important results of this study is the opposite trend in  $K_{IC}$  (decrease) and total ionic conductivity (increase) with increasing relative density. This is likely a result of the nature of the grain boundaries that vary with relative density. At low relative density, weak grain boundaries result as evidenced by intergranular fracture whereas, at high relative density strong grain boundaries result as evidenced by intragranular fracture. It is suggested that that the nature of the grain boundaries is mainly controlled by the volume fraction of intergranular porosity, which is known to correlate with grain boundary strength [135]. These results suggest that if high ionic conductivity LLZO is the goal, a sacrifice in  $K_{IC}$  will occur.

One possible solution to this dilemma is to engineer a toughening mechanism that acts within the grains yet, leaves strong grain boundaries to yield high ionic conductivity. A method that may

increase  $K_{IC}$  without drastically decreasing the total ionic conductivity would be the addition of partially stabilized ZrO<sub>2</sub> particles within the LLZO matrix, as has been used for the case of beta Al<sub>2</sub>O<sub>3</sub> [148-149]. This could lead to increased  $K_{IC}$  due to transformation toughening within the matrix and hopefully, would not diminish the high conductivity grain boundaries that result from hot-pressing to high relative density. Another possible solution could be the addition of a second phase (e.g., glass) along the LLZO grain boundaries that allows for high Li-ion conductivity across the grain boundaries but, when subjected to a mechanical stress would preferentially fracture along the grain boundaries giving improved toughness.

### 6.4 Summary

The effect of relative density (porosity) on the hardness,  $K_{IC}$  and total ionic conductivity of hotpressed Al-substituted cubic LLZO was investigated. It was observed that hot-pressing for 30 min, 60 min, 90 min, and 240 min at 1050 °C, resulted in 85 %, 95 %, 96 %, and 98 % relative densities, respectively. The average grain size varied from about 2.7  $\mu$ m to 3.7  $\mu$ m, while the primary fracture mode changed from inter to intragranular as the hot-pressing time increased from 30 min to 240 min.

The  $H_{\nu}$  increased with relative density up to approximately 96 %, above which the  $H_{\nu}$  was constant. The increase in  $H_{\nu}$  was correlated with a change in fracture mode from inter to intragranular as a result of reduced porosity at the grain boundaries leading to stronger boundaries as the relative density increased. At 98 % relative density, where almost 100 % intragranular fracture was exhibited, the  $H_{\nu}$  was equal to the  $H_{n}$ . This hardness value is in good

agreement with the predicted value based on the behavior of single crystalline oxide garnets, suggesting that the single crystal hardness of LLZO is approximately 9.1 GPa.

The  $K_{IC}$  values decreased linearly with increased relative density. The  $K_{IC}$  values were ~2.37 and ~0.97 MPa $\sqrt{m}$  for the samples with 85 and 98% relative density, respectively. Microstructural analysis suggests that the reasons for the increased  $K_{IC}$  values at low density are a result of increased intergranular porosity at the grain boundaries. The intergranular porosity results in weak grain boundaries, which deflects cracks out of the plane of maximum driving force and hence, increasing  $K_{IC}$ .

The total ionic conductivity increased with increasing relative density. This increase is associated with an increase in the grain boundary conductivity as a result of the change in the nature of the grain boundaries with the increasing relative density. At a relative density of 85%, the total ionic conductivity was 0.0094 mS cm<sup>-1</sup> and increased to 0.34 mS cm<sup>-1</sup> for the sample with a relative density of 98 %.

An interesting correlation between ionic conductivity and  $K_{IC}$  was observed. As the relative density increased, the ionic conductivity increased while the  $K_{IC}$  decreased. This correlation suggests that if one desires a LLZO material with high ionic conductivity a sacrifice in  $K_{IC}$  will occur. One possible solution to this dilemma is the addition of partially stabilized  $ZrO_2$  particles within the LLZO matrix which results in a toughening mechanism that acts with in the grains yet, leaves strong grain boundaries to yield high ionic conductivity. Another possibility is the addition of a low  $K_{IC}$  phase along the grain boundaries that exhibits good Li-ion transport, but promotes inter rather than intragranular fracture.

### 7 Summary and future work

# 7.1 Summary

To improve the performance and safety of Li-ion batteries for vehicle electrification, an HOH graphite electrode was developed and characterized. The HOH electrodes, which consisted of 5 % volume fraction of linear channels, were successfully manufactured using a custom-fabricated laser patterning technique development and maturation of the HOH electrode concept could help to decouple energy and power density while improving safety during charge and discharge processes. In this work, it was shown that the introduction of uniformly spaced, through-thickness macro-scale linear channels facilitate Li-ions transport in thick (high energy density) graphite electrodes up to 157 µm. Rate mapping results showed that an HOH electrode, consisting of 5.5 mAh cm<sup>-2</sup> loading with 45 % intrinsic open porosity and 5 % laser ablated open porosity, exhibited 65 % higher charge capacity retention compared to that of a conventional graphite electrodes at 1/3 C-rates. It was also shown that the HOH electrodes reduced the concentration polarization related to formation of deleterious metallic Li dendrites compared to conventional electrodes with the same loading and percent porosity.

The laser patterning technique that was developed is advantageous over other electrode patterning techniques owing to the following attributes: 1) fast patterning speed and simplicity, 2) precise position of the channels, 3) ability to pattern relatively thick electrodes (~157 µm), and 4) potentially low cost. In addition, since laser patterning uses a conventional graphite electrode, it is also possible to use the current typical electrode manufacturing process.

A novel hybrid design with LLZO ceramic electrolyte was proposed to mitigate safety issue related to Li dendrite growth. For this design, an important characteristic is the mechanical

properties of ceramic electrolyte. Since the mechanical properties of ceramics are strongly affected by defects, the relation between the microstructure and the mechanical properties of LLZO were characterized. It was shown that the lowest relative density (85 %) LLZO exhibited the highest fracture toughness ( $2.37 \pm 0.1 \text{ MPa}\sqrt{\text{m}}$ ) resulting from intergranular fracture (crack deflecting) and tip blunting. In contrast, high relative density (98 %) exhibited approximately half the fracture toughness values ( $0.971 \pm 0.11 \text{ MPa}\sqrt{\text{m}}$ ) compared to that of pellet with 85 % density. The main fracture mode was intragranular in the high relative density LLZO. However, the ionic conductivity values linearly increased by increasing the relative density. Therefore, to optimize for fracture toughness and ionic conductivity, additional research is required.

#### 7.2 Future work

## 7.2.1 HOH charge abuse testing

As was discussed in Chapter 3, the intentional overcharge test is an effective technique to characterize Li-ion concentration polarization based on color changes associated with different Li concentrations in graphite (gold: SOC ~100 %, red: SOC ~50 %, and black: SOC <~20 %). Based on the observed Li-ion concentration gradients, Li-ions tended to transport first through the macro-scale linear (laser ablated) channels followed by transport into the micro-scale intrinsic pores through the walls between channels. The improved rate mapping results support this assumption. In addition, the polarization interrupt test and TLM-EIS-SC methods demonstrated that HOH electrodes exhibit lower internal mass transport resistance compared to that of conventional electrodes under the same conditions. It is expected that the intentional overcharge test clearly shows the different Li-ion flow paths in HOH electrode compared to

conventional electrode. Figure 7-1 shows optical microscopy images of HOH electrodes (with 5.5 mAh cm $^{-2}$  and 5 % linear channels and 30 % intrinsic porosity (~115  $\mu m))$  that were intentionally overcharged in preliminary tests. The intentional overcharge conditions were conducted at 1 C-rate for 1 h. The majority of the overcharged HOH electrode surfaces were gold (SOC 100 %), and partially covered with metallic Li (silver color) (Figure 7-1a). The metallic Li deposition area was much smaller compared to what was observed on the conventional electrodes (Figure 3-8a). In addition, the gold color observed on the fracture surface indicated that through thickness concentration polarization was minimized compared to the conventional electrode (Figure 7-1b). It is also interesting to note that Li metal deposition was apparent on the inner walls of the macro-scale channels. This indicates that Li-ions flow path was lateral, i.e. from the macro-scale linear channels into the intrinsic porosity. Based on this observation, the HOH may also provide improved safety by orienting Li-ion dendrite growth laterally into the macro-channels rather than into the separator and toward the positive electrode, which would result in a short-circuit. However, there is a discrepancy between what is observed in the optical images and what is shown in the potential versus time plots during the preliminary overcharge tests. Both electrode types indicated the lower-bound cut-off potential (0 V) was reached in ~ 100 s. If Li plating was suppressed, the time to reach the 0 V cut-off potential should have been greater. Therefore, further studies are needed to understand the relationship between the potential vs time plot and the optical images.

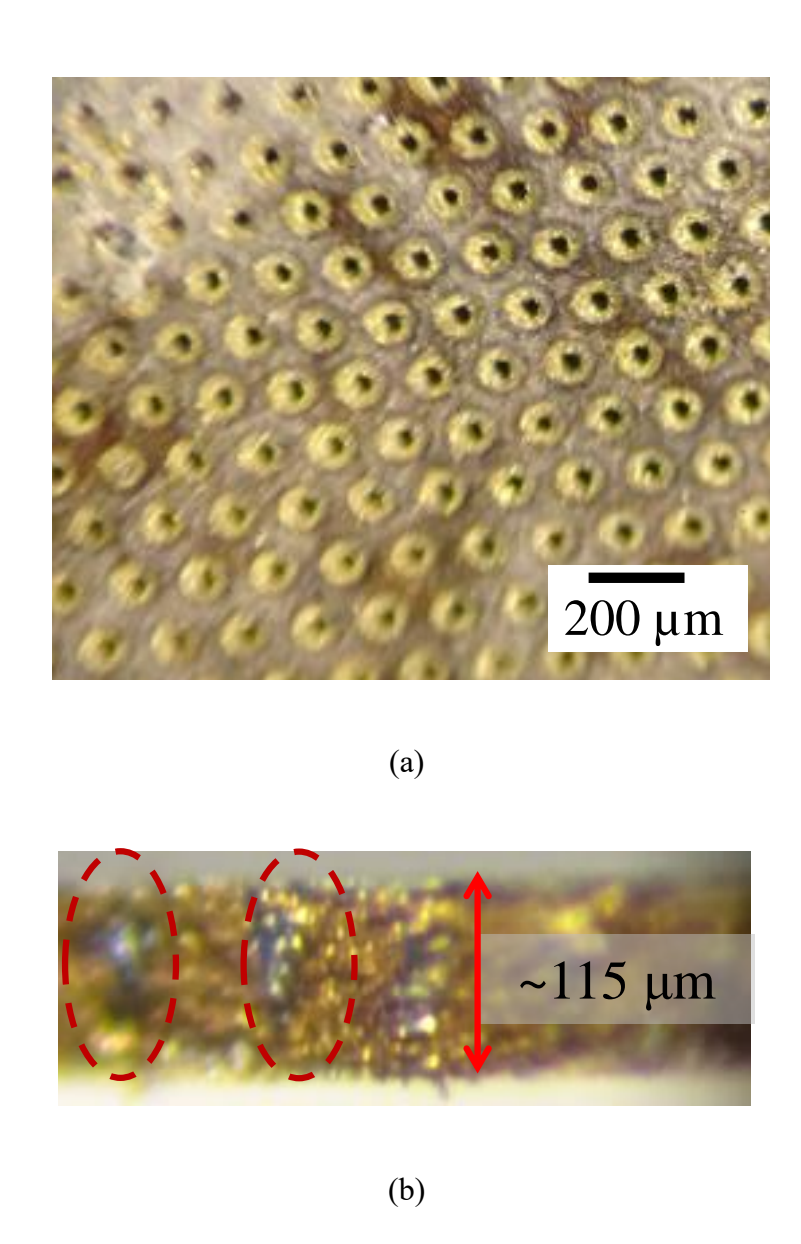


Figure 7-1: (a) Optical top image and (b) fracture surface images of electrode with 5.5 mAh cm<sup>-2</sup> and 35 total porosity (30 % intrinsic porosity and 5 % laser ablated porosity) after overcharging at 1 C-rate for 1 h.

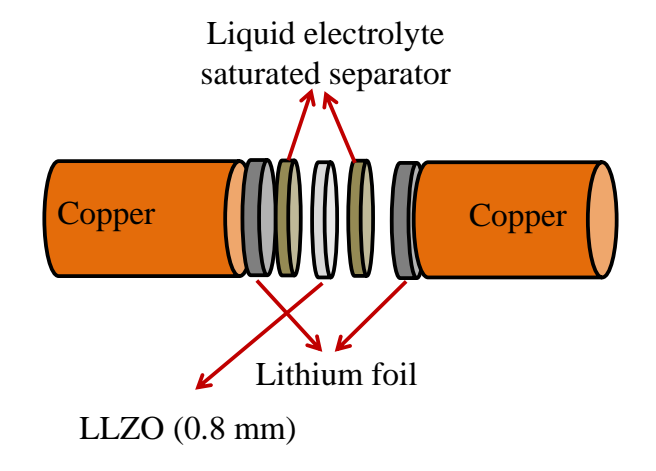
### 7.2.2 Rate mapping at low temperature

It is known that capacity retention decreases with decreasing temperature in Li-ion batteries [126]. Therefore, it is necessary to understand and improve the de/intercalation mechanisms at low temperature. The poor performance and metallic Li plating that occurs during low temperature charging is believed to be due to relatively slow Li-ion mobility in the electrolyte-filled pores [126]. As was discussed, since HOH electrode improves rate capability by improving Li-ion transport, HOH might improve the performance and safety of Li-ions batteries at low temperature. Furthermore, because the mechanisms that contribute to cell impedance have different activation energies, lowering the temperature may enable isolation or amplification of certain kinetic phenomena to better understand the rate limiting step(s) in high energy density electrodes.

### 7.2.3 Realizing a novel hybrid cell design with ceramic electrolytes

A novel hybrid cell design employing an LLZO ceramic electrolyte was proposed to improve safety and performance. In Chapter 6, the relationship between the mechanical properties and the relative densities was investigated. Based on this study, the relative density can be determined that optimizes for fracture toughness and ionic conductivity. Although the LLZO cubic phase has high ionic conductivity (0.4-1 mS cm<sup>-1</sup>), integrating it into all solid-state batteries may be challenging due to high interfacial impedance. However, the proposed hybrid solid-liquid cell design can reduce the interfacial contact resistance. To support this argument, a symmetric hybrid cells employing LLZO separators were fabricated and characterized (Figure 7-

2). The cell was composed of an LLZO electrolyte membrane placed between 2 electrolyte-saturated separators, placed between two Li metal electrodes (Figure 7-2). The symmetric cell exhibited stable and ohmic behavior with negligible contact resistance up to 1 mA cm<sup>-2</sup> current density (Figure 7-2b). Moreover, the results of DC cycling test of the hybrid symmetric cell also showed stable behavior at 1 mA cm<sup>-2</sup> current density for 20 cycles (Figure 7-2c). These demonstrate that a fast ion conducting ceramic electrolyte may allow for the facile transport of Li-ions while acting as a physical barrier to stop Li dendrite propagation. Therefore, the same hybrid cell should be investigated as an alternative approach to mitigate safety concerns related Li metal dendrites. Furthermore, the combining HOH electrode and the ceramic electrolyte is expected to result in higher performance and safety (Figure 7-3). This combined approach may enable the development of high energy and power density Li-ion batteries with improved safety.



(a)

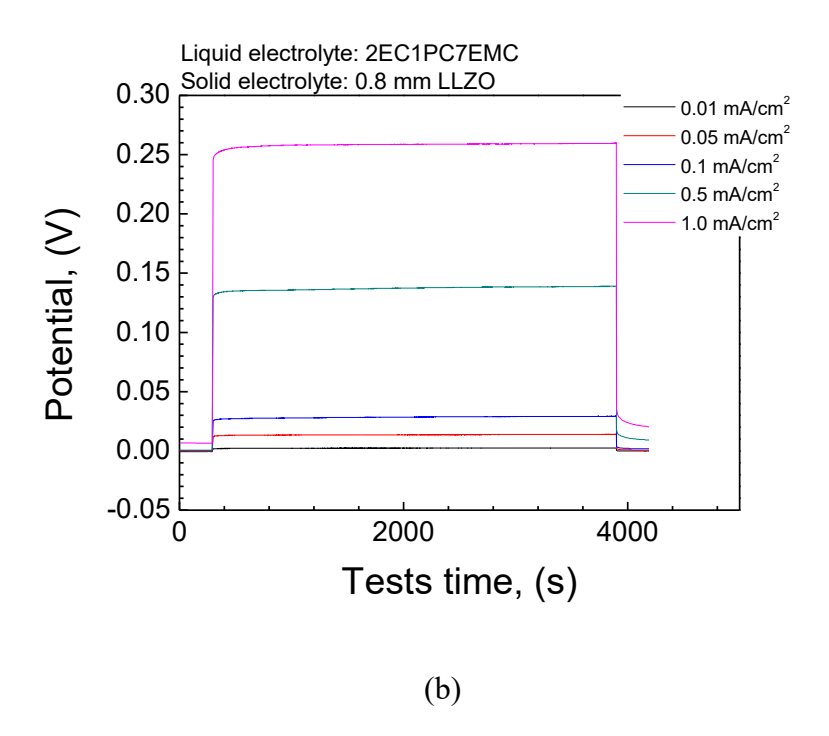
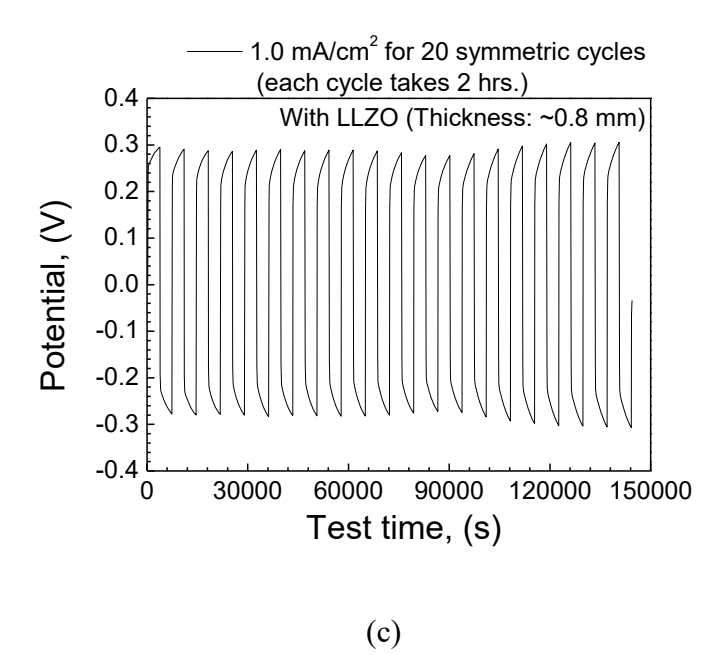


Figure 7-2: Schematic of (a) cell configuration for asymmetric DC test, (b) the results of the DC test, and (c) DC cycling test. The DC test was conducted after conditioning cycles at 0.01 mA cm<sup>-2</sup> for 10 symmetric cycles (each cycle takes 2h). Then DC cycling test was conducted at 1 mA cm<sup>-2</sup> for 20 cycles. The each cycle takes 2h.

Figure 7-2 (cont'd).



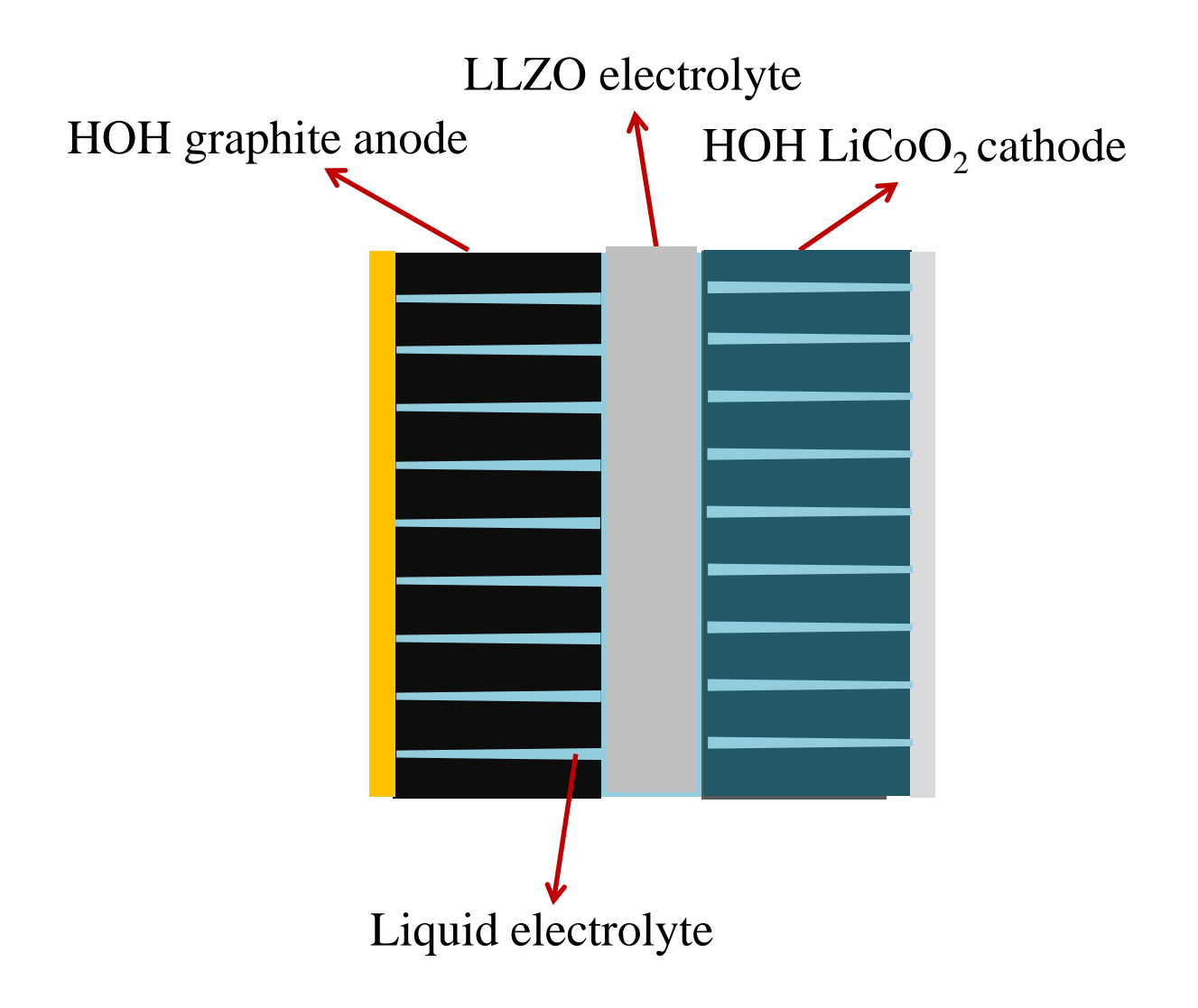


Figure 7-3: Schematic of novel hybrid design of Li-ion batteries with combining HOH concept and LLZO electrolyte for the higher performance and safety.

REFERENCES

#### REFERENCES

- [1] Q. Wang, P. Ping, and X. Zhao *et al.* "Thermal runaway caused fire and explosion of lithium ion battery," *Journal of Power Sources* 208 (2012): 210-224.
- [2] L.X. Yuan, Z.H. Wang, and W.X. Zhang *et al.* "Development and challenges of LiFePO<sub>4</sub> cathode material for lithium-ion batteries," *Energy & Environmental Science* 4 (2011): 269-284.
- [3] G. Majeau-Bettez, T.R. Hawkins, and A.H. Stromman. "Life cycle environmental assessment of lithium-ion and nickel metal hydride batteries for plug-in hybrid and battery electric vehicles," *Environmental Science & Technology* 45 (2011): 4548-4554.
- [4] J. Chen. "Recent progress in advanced materials for lithium ion batteries," *Materials* 6 (2013): 156-183.
- [5] G.L. Soloveichik. "Battery technologies for large-scale stationary energy storage," *Annual Reviews of Chemical and Bimolecular Engineering* 2 (2011): 503-27.
- [6] E.D. Wachsman and K.T. Lee. "Lowering the temperature of solid oxide fuel cells," *Science* 334 (2011): 935-939.
- [7] B. Dunn, H. Kamath, and J.M. Tarascon. "Electrical Energy Storage for the Grid: A Battery of Choices," *Science* 18 (2011): 928-935.
- [8] J.M. Tarascon and M. Armand. "Issues and challenges facing rechargeable lithium batteries." *Nature* 414 (2001): 359-367.
- [9] Y.P. Wu, E. Rahm, and R. Holze. "Carbon anode materials for lithium ion batteries," *Journal of Power Sources* 114 (2003): 228-236.
- [10] R. Moshtev and B. Johnson. "State of the art of commercial Li ion batteries." *Journal of Power Sources* 91 (2000): 86-91.
- [11] T. Nagaura and K. Tozawa. "Lithium ion rechargeable battery." *Prog. Batteries Solar Cells* 9 (1990): 209-217.
- [12] C. Jiang, E. Hosono, and H. Zhou. "Nanomaterials for lithium ion batteries." *Nano Today* 1 (2006): 28-33.
- [13] P. Arora, R.E. White, and M. Doyle. "Capacity fade mechanisms and side reactions in lithium-ion Batteries." *Journal of the Electrochemical Society* 145 (1998): 3647-3667.

- [14] A.S. Arico, P. Bruce, and B. Scrosati *et al.* "Nanostructured materials for advanced energy conversion and storage devices." *Nature Materials* 4 (2005): 366-377.
- [15] R.A. Huggins. Advanced batteries, Springer Science+Business Media, LLC (2009).
- [16] "Basic research needs for electrical energy storage" Office of Basic Energy Science, U.S. Department of Energy, Washington, DC, July (2007).
- [17] W.A. van Schalkwijk, B. Scrosati. Advances in lithium ion batteries, Kluwer Academic Publishers (2002)
- [18] R. Yazami and D. Universitarie. "A reversible graphite-lithium negative electrode for electrochemical generators," *Journal of Power Sources* 9 (1983): 365-371.
- [19] H. Buqa, D. Goers, and M. Holzapfel *et al.* "High rate capability of graphite negative electrodes for lithium-ion batteries." *Journal of the Electrochemical Society* 152 (2005): A474-A481.
- [20] X. Zhu, Y. Zhu, and S. Murali *et al.* "Nanostructured reduced graphene oxide/Fe<sub>2</sub>O<sub>3</sub> composite as a high-performance anode material for lithium ion batteries." *ACS Nano* 5 (2011): 3333-3338.
- [21] D.D. Richardson. "A calculated of Van Der Walls intercalations in and between layers of atoms: application to graphite," *Journal of Physics C: Solid State Physic* 10 (1977): 3235-3242.
- [22] A. Lerf. "Storylines in intercalation chemistry," *Dalton Transactions* 43 (2014): 10276-10291.
- [23] M. Winter, J.O. Besenhard, M.E. Spahr, and P. Novak. "Insertion electrode materials for rechargeable lithium batteries," Advanced Materials 10.10. (1999):725-763.
- [24] J.O. Besenhard and H.P. Fritz. "The electrochemistry of black carbons," *Angewandte Chemie International Edition* 22 (1983): 950-975.
- [25] C.K. Chan, H. Peng, and G. Liu *et al.* "High-performance lithium battery anodes using silicon nanowires," *Nature Nanotechnology* 3.1 (2008): 31-35.
- [26] M. Winter and J.O. Besenhard. "Electrochemical lithiation of tin and tin-based intermetallics and composites," *Electrochimica Acta* 45.1 (1999): 31-50.
- [27] B. Scrosati and J. Garche. "Lithium batteries: Status, prospects and future," *Journal of Power Sources* 195 (2010): 2419-2430.
- [28] A. Manthiram. "Materials challenges and opportunities of lithium ion batteries," *The Journal of Physical Chemistry Letters* 2.3 (2011): 176-184.

- [29] K. Mizushima, P.C. Jones, P.J. Wiseman, J.B. Goodenough. "Li<sub>x</sub>CoO<sub>2</sub> (0<x<-1: A new cathode material for batteries of high energy density," *Materials Research Bulletin* 15 (1980): 783–789.
- [30] B. Xu, D. Qian, and Z. Wang *et al.* "Recent progress in cathode materials research for advanced lithium ion batteries," *Materials Science and Engineering R* 73 (2012): 51-65.
- [31] B. L. Ellis, K.T. Lee, and L.F. Nazar. "Positive electrode materials for Li-ion and Libatteries," *Chemistry of Materials* 22.3 (2010): 691–714.
- [32] Z.H. Chen, Z.H. Lu, and J.R. Dahn. "Staging phase transitions in Li<sub>x</sub>CoO<sub>2</sub>," *Journal of the Electrochemical Society* 149 (2002): A1604-A1609.
- [33] S.A. Hallaj, R. Venkatachalapathy, J. Prakash, and J.R. Selman. "Entropy changes due to structural transformation in the graphite anode and phase change of the LiCoO<sub>2</sub> cathode," *Journal of the Electrochemical Society* 147 (2000): 2432-2436.
- [34] X. Yuan, H. Liu, and J. Zhang. Lithium-Ion Batteries: Advanced Materials and Technologies. CRC Press, 2011.
- [35] J. Bréger, Y.S. Meng, and Y. Hinuma *et al.* "Effect of high voltage on the structure and electrochemistry of LiNi<sub>0.5</sub>Mn<sub>0.5</sub>O<sub>2</sub>: A joint experimental and theoretical study," *Chemistry of Materials* 18.20 (2006): 4768-4781.
- [36] M.M. Thackeray, W.I.F. David, P.G. Bruce, and J.B. Goodenough. "Lithium insertion into manganese spinels," *Materials Research Bulletin* 18 (1983): 461-472.
- [37] A.K. Padhi, K.S. Nanjundaswamy, and C. Masquelier *et al.* "Effect of structure on the Fe<sup>3+</sup>/Fe<sup>2+</sup> redox couple in iron phosphates," *Journal of the Electrochemical Society* 144.5 (1997): 1609–1613.
- [38] S. Nishimura, G. Kobayashi, and K. Ohoyama *et al.* "Experimental visualization of lithium diffusion in Li<sub>x</sub>FePO<sub>4</sub>," *Nature Materials* 7 (2008): 707-711.
- [39] D. Aurbach, Y. Talyosef, and B. Markovsky *et al.* "Design of electrolyte solution for Li and Li-ion batteries: a review," *Electrochimica Acta* 50 (2004): 247-254.
- [40] H. Tao, H. Liu, and X. Kan *et al.* "Reality and future of rechargeable lithium batteries," *The Open Materials Science Journal* 5 (2011): 204-214.
- [41] S.K. Jeong, M. Inaba, and R. Mogi *et al.* "Surface film formation on a graphite negative electrode in lithium-ion batteries: Atomic force microscopy study on the effects of film-forming additives in propylene carbonate solutions," *Langmuir* 17.26 (2001): 8281-8286.

- [42] S.S. Zhang, K. Xu, and J.L. Allen *et al.* "Effect of propylene carbonate on the low temperature performance of Li-ion cells," *Journal of Power Sources* 110.1 (2002): 216-221.
- [43] S.S. Zhang, M.S. Ding, and K. Xu et al. "Understanding solid electrolyte interface film formation on graphite electrodes," *Electrochemical and Solid-State Letters* 4 (2001): A206-A208.
- [44] T. Ohsaki, T. Kishi, and T. Kuboki *et al.* "Overcharge reaction of lithium-ion batteries," *Journal of Power Sources* 146 (2005): 97-100.
- [45] Y.H. Liu, C.H. Hsieh, and Y.F. Luo. "Search for an optimal five-step charging pattern for Li-ion batteries using consecutive orthogonal array," *IEEE Transactions on Energy Conversion* 26 (2011): 654-661.
- [46] P.G. Balakrishnan, R. Ramesh, and T.P. Kumar. "Safety mechanisms in lithium-ion batteries," *Journal of Power Sources* 155 (2006): 401-414.
- [47] P. Birke, F. Salam, S. Döring, and W. Weppner. "A first approach to a monolithic all solid state inorganic lithium battery," *Solid State Ionics* 118 (1999): 149-157.
- [48] J.B. Goodenough. "Review lecture: fast ionic conduction in solid," *Processing of the Royal Society of London* A 393 (1984): 215-234.
- [49] P. Knauth. "Inorganic solid Li ion conductors: An overview," *Solid State Ionics* 180 (2009): 911-916.
- [50] K. Takada. "Progress and prospective of solid-state lithium batteries," *Acta Materialia* 61 (2013): 759-770.
- [51] G.Y. Adachi, N. Imanaka, and H. Aono. "Fast Li<sup>+</sup> conducting ceramic electrolytes," *Advanced Materials* 8.2 (1996): 127-135.
- [52] V. Thangadurai, H. Kaack, and W. Weppner. "Novel fast lithium ion conduction in garnet-type  $Li_5La_3M_2O_{12}$  (M = Nb, Ta)," *Journal of the American Ceramic Society* 86 (2003): 437-440.
- [53] R. Murugan, V. Thangadurai, and W. Weppner. "Fast lithium ion conduction in garnet-type Li<sub>7</sub>La<sub>3</sub>Zr<sub>2</sub>O<sub>12</sub>," *Angewandte Chemie International Edition* 46 (2007): 7778-7781.
- [54] A. Logéat, T. Kohler, and U. Eisele *et al.* "From order to disorder: The structure of lithium-conducting garnets Li<sub>7-x</sub>La<sub>3</sub>Ta<sub>x</sub>Zr<sub>2-x</sub>O<sub>12</sub> (x=0-2)," *Solid State Ionics* 206 (2012): 33-38.
- [55] J. Wolfenstine, J. Allen, E. Rangasamy and J. Sakamoto. "Synthesis and high Li-ion conductivity of Ga-stabilized cubic Li<sub>7</sub>La<sub>3</sub>Zr<sub>2</sub>O<sub>12</sub>," *Journal of Materials Science* 134 (2012): 571-575.

- [56] E. Rangasamy, J. Wolfenstine, and J. Sakamoto. "The role of Al and Li concentration on the formation of cubic garnet solid electrolyte of nominal composition Li<sub>7</sub>La<sub>3</sub>Zr<sub>2</sub>O<sub>12</sub>," *Solid State Ionics* 206 (2012): 28-32.
- [57] US Advanced Battery Consortium (USABC) goals for advanced batteries for EVs (2006). Available at: <a href="http://uscar.org/commands/files\_download.php?files\_id=27">http://uscar.org/commands/files\_download.php?files\_id=27</a>.
- [58] J. Vetter, P. Novak, and M.R. Wagner *et al.* "Ageing mechanisms in lithium-ion batteries," *Journal of Power Sources* 147 (2005): 269-281.
- [59] H. Okamoto. "Cu-Li (Copper-Lithium)." *Journal of Phase Equilibria and Diffusion* 32.2 (2011): 172-172.
- [60] L. Fransson, T. Eriksson, and K. Edstrom *et al.* "Influence of carbon black and binder on Liion batteries," *Journal of Power Sources* 101 (2001): 1-9.
- [61] U. Kasavajjula, C. Wang, and A.J. Appleby. "Nano- and bulk-silicon-based insertion anodes for lithium-ion secondary cells," *Journal of Power Sources* 163 (2007): 1003-1039.
- [62] A. Yaqub, Y.J. Lee, and M.J. Hwang *et al.* "Effects of electrode loading on low temperature performances of Li-ion batteries," *Physica Status Solidi A* 211 (2014): 2625-2630.
- [63] D. Belov and M.H. Yang. "Failure mechanism of Li-ion battery at overcharge conditions," *Journal of Solid State Electrochemistry* 12 (2008): 885-894.
- [64] J. Cho, Y.W. Kim, and B. Kim *et al.* "A breakthrough in the safety of lithium secondary batteries by coating the cathode material with AlPO<sub>4</sub> nanoparticles," *Angewandte Chemie International Edition* 42 (2003): 1618-1621.
- [65] S.I. Tobishima, K. Takei, Y. Sakurai, and J.I. Yamaki. "Lithium ion cell safety," *Journal of Power Sources* 90.2 (2000): 188-195.
- [66] J.J Krol, M. Wessling, and H. Strathmann. "Concentration polarization with monopolar ion exchange membranes: current–voltage curves and water dissociation," *Journal of Membrane Science*, 162 (1999): 145-154.
- [67] A.V. Virkar, J. Chen, C.W. Tanner, and J.W. Kim. "The role of electrode microstructure on activation and concentration polarizations in solid oxide fuel cells," *Solid State Ionics* 131 (2000): 189-198.
- [68] J.S. Sakamoto and B. Dunn. "Hierarchical battery electrodes based on inverted opal structures," *Journal of Materials Chemistry* 12 (2002): 2859-2861.
- [69] H. Zhang, X. Yu, and P.V. Braun. "Three-dimensional bicontinuous ultrafast-charge and discharge bulk battery electrodes," *Nature Nanotechnology Letter* 6 (2011): 277-281.

- [70] C.J. Bae, C.K. Erdonmez, and J.W. Halloran *et al.* "Design of battery electrodes with dual-scale porosity to minimize tortuosity and maximize performance," *Advanced Materials* 25 (2013): 1254-1258.
- [71] P. Birke, F. Salam, S. Döring, and W. Weppner. "A first approach to a monolithic all solid state inorganic lithium battery," *Solid State Ionics* 118 (1999): 149-157.
- [72] V. Srinivasan, Batteries for vehicular applicaions, Lawrence Berkely National Laboratory, Berkeley, CA, 2008. http://rael.berkeley.edu/old\_drupal/sites/default/files/old-site-files/apsenergy/3.4%20Venkat%20S%20Mar%207.2008.pdf.
- [73] I.N. David, T. Thompson, J. Wolfenstine, J.L. Allen, and J. Sakamoto. "Microstructure and Li-ion conductivity of hot-pressed cubic Li<sub>7</sub>La<sub>3</sub>Zr<sub>2</sub>O<sub>12</sub>," *Journal of American Ceramic Society* 98.4 (2015): 1209-1214.
- [74] J.L. Allen, J. Wolfenstine, E. Rangasamy, and J. Sakamoto. "Effect of substitution (Ta, Al, Ga) on the conductivity of Li<sub>7</sub>La<sub>3</sub>Zr<sub>2</sub>O<sub>12</sub>," *Journal of Power Sources* 206 (2012): 315-319.
- [75] Y. Jin and P.J. McGinn. "Li<sub>7</sub>La<sub>3</sub>Zr<sub>2</sub>O<sub>12</sub> electrolyte stability in air and fabrication of a Li/Li<sub>7</sub>La<sub>3</sub>Zr<sub>2</sub>O<sub>12</sub>/Cu<sub>0.1</sub>V<sub>2</sub>O<sub>5</sub> solid-state battery," *Journal of Power Sources* 239 (2013): 326-331.
- [76] G. Larraz, A. Orera, J. Sanz, I. Sobrados, V. Diez-Gomex, and M.L. Sanjuan. "NMR Study of Li distribution in Li<sub>7-x</sub>H<sub>x</sub>La<sub>3</sub>Zr<sub>2</sub>O<sub>12</sub> garnets," *Journal of Materials Chemistry A* 3 (2015): 5683-5691.
- [77] B.V. Ratnakumar, M.C. Smart, and S. Surampudi. "Effects of SEI on the kinetics of lithium intercalation," *Journal of Power Sources* 97-98 (2001): 137-139.
- [78] S.S. Zhang, K. Xu, and T.R. Jow. "EIS study on the formation of solid electrolyte interface in Li-ion battery," *Electrochimica acta*, 51 (2006): 1636-1640.
- [79] W. Weppner and R.A. Huggins. "Determination of the kinetic parameters of mixed-conducting electrodes and application to the system Li<sub>3</sub>Sb," *Journal of The Electrochemical Society* 124.10 (1977): 1569-1578.
- [80] I.V. Thorat, D.E. Stephenson, and N.A. Zacharias *et al.* "Quantifying tortuosity in porous Li-ion battery materials," *Journal of Power Sources* 188 (2009): 592-600.
- [81] R.A. Huggins. "Simple method to determine electronic and ionic components of the conductivity in mixed conductors: A review," *Ionics* 8 (2002): 300-313.
- [82] J.T.S. Irvine, D.C. Sinclair, A.R. West. "Electroceramics: Characterization by impedance spectroscopy," *Advanced Materials* 2.3 (1990): 132-138.

- [83] N. Ogihara, S. Kawauchi, and C. Okuda *et al.* "Theoretical and experimental analysis of porous electrodes for lithium-ion batteries by electrochemical impedance spectroscopy using a symmetric cell," *Journal of The Electrochemical Society* 159 (2012): A1034-A1039.
- [84] R.D. Levie. "On porous electrode in electrolyte solutions-IV," *Electrochimica Acta* 9 (1964): 1231-1245.
- [85] J.H. Jang, S. Yoon, B.H. Ka, Y.H. Jung, and S.M. Oh. "Complex capacitance analysis on leakage current appearing in electric double-layer capacitor carbon electrode," *Journal of the Electrochemical Society* 152.7 (2005): A1418-A1422.
- [86] R.L. Smith and G.E. Sandland. "An accurate method of determining the hardness of metals, with particular reference to those of a high degree of hardness," *Proceedings of the Institution of Mechanical Engineers* 102.1 (1922): 623-641.
- [87] G.D. Quinn and R.C. Bradt. "On the vickers indentation fracture toughness test," *Journal of the American Ceramic Society* 90.3 (2007): 673-680.
- [88] A.G. Evans and A. Charles. "Fracture toughness determinations by indentation," *Journal of the American Ceramic society* 59.7-8 (1976): 371-372.
- [89] B.R. Lawn, A.G. Evans, and D.B. Marshall. "Elastic/plastic indentation damage in ceramics: the median/radial crack system," *Journal of the American Ceramic Society* 63.9-10 (1980): 574-581.
- [90] G.R. Anstis, P. Chantikul, B.E. Lawn, and D.B. Marshall. "A critical evaluation of indentation techniques for measuring fracture toughness: I, Direct crack measurements," *Journal of the American Ceramic Society* 64.9 (1981): 533-538.
- [91] D.G. Bhat. "Comment on "Elastic/plastic indentation damage in ceramics: The median/radial crack system," *Journal of the American Ceramic Society* 64.11 (1981): C165-C166.
- [92] W.C. Oliver and G.M. Pharr. "An improved technique for determining hardness and elastic modulus using load and displacement sensing indentation experiments," *Journal of Materials Research* 7.06 (1992): 1564-1583.
- [93] W.C. Oliver and G.M. Pharr. "Measurement of hardness and elastic modulus by instrumented indentation: Advances in understanding and refinements to methodology," *Journal of Materials Research* 19.01 (2004): 3-20.
- [94] B.D. Cullity. "Elements of X-ray diffraction," Adisson-Wesley Publish hing. USA (1978).
- [95] L.M. Malard, M.A. Pimenta, G. Dresselhaus, and M.S. Dresselhaus. "Raman spectroscopy in graphene," *Physics Reports*, 473.5-6 (2009): 51-87.

- [96] K.M. Abraham, D.M. Pasquariello, and E.M. Willstaedt. "Discharge rate capability of the LiCoO<sub>2</sub> electrode," *Journal of the Electrochemical Society* 145 (1998): 482-486.
- [97] T. Abe, H. Fukuda, Y. Iriyama, and Z. Ogumi. "Solvated Li-ion transfer at interface between graphite and electrolyte," *Journal of the Electrochemical Society* 151 (2004): A1120-A1123.
- [98] T. Abe, F. Sagane, M. Ohtsuka, and Y. Iritama *et al.* "Lithium-ion transfer at the interface between lithium-ion conductive ceramic electrolyte and liquid electrolyte-A key to enhancing the rate capability of lithium-ion batteries," *Journal of the Electrochemical Society* 152 (2005): A2151-A2154.
- [99] B. Marinho, M. Ghislandi, and E. Tkalya *et al.* "Electrical conductivity of compacts of graphene, multi-wall carbon nanotubes, carbon black, and graphite powder," *Powder Technology* 221 (2012): 351-358.
- [100] S.S. Zhang. "A review on electrolyte additives for lithium-ion batteries," *Journal of Power Sources* 162 (2006): 1379-1394.
- [101] D. Aurbach, K. Gamolsky, and B. Markovsky *et al.* "On the use of vinylene carbonate (VC) as an additive to electrolyte solutions for Li-ion batteries," *Electrochimica Acta* 47.9 (2002): 1423-1439.
- [102] M. Matyka, A. Khalili, and Z. Koza. "Tortuosity-porosity relation in porous media flow," *Physical Review E* 78.2 (2008): 026306-1-8.
- [103] D.W. Chung, M. Ebner, and D.R. Ely *et al.* "Validity of the Bruggeman relation for porous electrodes," *Modelling and Simulation in Materials Science and Engineering* 21 (2013): 074009-1-16.
- [104] P.R. Shearing, L.E. Howard, and P.S. Jorgensen *et al.* "Characterization of the 3-dimensional microstructure of a graphite negative electrode from a Li-ion battery," *Electrochemistry communications* 12 (2010): 374-377.
- [105] Y.C.K.C. Wiegart, R. DeMike, and C. Eronmez *et al.* "Tortuosity characterization of 3D microstructure at nano-scale for energy storage and conversion materials," *Journal of Power Sources* 249 (2014): 349-356.
- [106] D.W. Chung, P.R. Shearing, and N.P. Brandon *et al.* "Particle size polydispersity in Li-ion batteries," *Journal of the Electrochemical Society* 161 (2014): A422-A430.
- [107] R.B. MacMullin and G.A. Muccini. "Characteristics of porous beds and structures," *American Institute of Chemical Engineers Journal* 2 (1956): 393-403.

- [108] D. Kehrwald, P.R. Shearing, and N.P. Brandon *et al.* "Local tortuosity inhomogeneities in a lithium battery composite electrode," *Journal of the Electrochemical Society* 158.12 (2011): A1393-A1399.
- [109] L.A. Giannuzzi and F.A. Stevie. Introduction to focused ion beams: instrumentation, theory, techniques and practice, Springer 2005.
- [110] P. Yu, B.N. Popov. J.A. Ritter, and R.E. White. "Determination of the lithium ion diffusion coefficient in graphite," *Journal of the Electrochemical Society* 146 (1999): 8-14.
- [111] N. Takami, A. Satoh, M. Hara, and T. Ohsaki *et al.* "Structural and kinetic characterization of lithium intercalation into carbon anode for secondary lithium batteries," *Journal of the Electrochemical Society* 142 (1995): 371-379.
- [112] M.D. Levi and D. Aurbach. "Diffusion coefficients of lithium ions during intercalation into graphite derived from the simultaneous measurements and modeling of electrochemical impedance and potentiostatic intermittent titration characteristics of thin graphite electrodes," *The Journal of Physical Chemistry B* 101 (1997): 4641-4647.
- [113] H. Tao, Z. Feng, and H. Liu *et al.* "Reality and future of rechargeable lithium batteries," *The Open Materials Science Journal* 5 (2011): 204-214.
- [114] C.H. Doh, D.H. Kim, and H.S. Kim *et al.* "Thermal and electrochemical behaviour of C/Li<sub>x</sub>CoO<sub>2</sub> cell during safey test," *Journal of Power Sources* 175 (2008): 881-885.
- [115] L. Lu, X. Han, and J. Li *et al.* "A review on the key issues for lithium-ion battery management in electric vehicles," *Journal of power sources* 226 (2013): 272-288.
- [116] J. Jiang and J.R. Dahn. "ARC studies of the reaction between Li<sub>0</sub>FePO<sub>4</sub> and LiPF<sub>6</sub> or LiBOB EC/DEC electrlytes," *Electrochemistry Comunications* 6 (2004) 724-728.
- [117] Y. Qi and S.J. Harris. "In situ observation of strains during lithiation of a graphite electrode," *Journal of the Electrochemical Society* 157 (2010): A741-A747.
- [118] C.L. Cobb and M. Blanco. "Modeling mass and density distribution effects on the performance of co-extruded electrodes for high energy density lithium-ion batteries," *Journal of Power Sources* 249 (2014): 357-366.
- [119] H. Ji, L. Zhang, and M.T. Pettes *et al.* "Ultrathin graphite foam: a three-dimensional conductive network for battery electrodes," *Nano letters* 12 (2012): 2446-2451.
- [120] C.C. Ho, K. Murata, and D.A. Steingart *et al.* "A super ink jet printed zinc–silver 3D microbattery," *Journal of Micromechanics and Microengineering* 19.9 (2009): 094013-1-5.

- [121] H. Zheng, J. Li, and X. Song *et al.* "A comprehensive understanding of electrode thickness effects on the electrochemical performances of Li-ion battery cathodes," *Electrochimica Acta* 71 (2012): 258-265.
- [122] J. Backholm, P. Georen, and G.A. Niklasson. "Determination of solid phase chemical diffusion coefficient and density of states by electrochemical methods: Application to iridium oxide-based thin films," *Journal of Applied Physics* 103.2 (2008): 023702-1-10.
- [123] A. Funabiki, M. Inaba, and Z. Ogumi. "AC impedance analysis of electrochemical lithium intercalation into highly oriented pyrolytic graphite," *Journal of Power Sources* 68.2 (1997): 227-231.
- [124] R.S. Nicholson. "Theory and application of cyclic voltammetry for measurement of electrode reaction kinetics," *Analytical Chemistry* 37.11 (1965): 1351-1355.
- [125] Z. Shen, L. Cao, C.D. Rahn, and C.Y. Wang. "Least squares galvanostatic intermittent titration technique (LS-GITT) for accurate solid phase diffusivity measurement," *Journal of the Electrochemical Society* 160.10 (2013): A1842-A1846.
- [126] C.K. Huang, J.S. Sakamoto, J. Wolfenstine, and S. Surampudi. "The limits of low-temperature performance of Li-ion cells," *Journal of the Electrochemical Society* 147 (2000): 2893-2896.
- [127] S.S. Zhang. "A review on the separators of liquid electrolyte Li-ion batteries," *Journal of Power Sources* 164.1 (2007): 351-364.
- [128] L. Cheng, W. Chen, and M. Kunz *et al.* "Effect of surface microstructure on electrochemical performance of garnet solid electrolytes," *ACS Applied Materials & Interfaces* 7.3 (2015): 2073-2081.
- [129] J.E. Ni, E.D. Case, and J.S. Sakamoto *et al.* "Room temperature elastic moduli and Vickers hardness of hot-pressed LLZO cubic garnet," *Journal of Materials Science* 47.23 (2012): 7978-7985.
- [130] R.L. Coble, "Sintering alumina: Effect of atmospheres," *Journal of American Ceramic Society* 45.3 (1962): 123-127.
- [131] Y.K. Paek, K.Y. Eun, and S.J.L. Kang. "Effect of sintering atmosphere on densification of MgO-doped Al<sub>2</sub>O<sub>3</sub>," *Journal of American Ceramic Society* 71.8 (1988): C380-C382.
- [132] S.R. James. Introduction to the Principles of Ceramic Processing, Wiley Interscience, New York, USA, 1988.

- [133] Y. Kim, H. Jo, J.L. Allen, H. Choe, J. Wolfenstine, and J. Sakamoto. "The effect of relative density on the mechanical properties of hot-pressed cubic Li7La3Zr2O12," *Journal of the American Ceramic Society Accepted* (2015).
- [134] S.B. Kim et al. "Effect of grain size and poling on the fracture mode of lead zirconate titanate ceramics," *Journal of the American Ceramic Society* 73.1 (1990): 161-163.
- [135] R.W. Davidge, Mechanical behavior of ceramics, Cambridge University Press, Cambridge, UK 1979.
- [136] R.W. Rice. Strength and fracture of Hot-pressed MgO, *Proceedings of the British Ceramic Society* 20 (1972): 329-64.
- [137] D.J. Green. An Introduction to the mechanical properties of ceramics, Cambridge University Press, Cambridge, UK 1998.
- [138] M.W. Barsoum. Fundamentals of ceramics, The McGraw-Hill Companies Inc., New York, USA 2002.
- [139] J.B. Wachtman, W.R. Cannon, and M.J. Matthewson. Mechanical properties of ceramics, Wiley & Sons Inc., New York, USA (2009).
- [140] D.B. Sirdeshmukh, L. Sirdeshmukh, and K.G. Subhadra *et al.* "Systematic hardness measurements on some rare earth garnet crystal," *Bulletin of Materials Science* 24.5 (2001): 469-473.
- [141] Y.M. Chiang, D.P. Birnie, and W.D. Kingery. Physical ceramics, Wiley, New York, USA 1996.
- [142] J. Wolfenstine, H. Jo, and Y.H. Cho *et al.* "A preliminary investigation of fracture toughness of Li<sub>7</sub>La<sub>3</sub>Zr<sub>2</sub>O<sub>12</sub> and its comparison to other solid Li-ion conductors," *Materials Letters* 96 (2013): 117-120.
- [143] R.W. Rice. "Grain size and porosity dependence of ceramic fracture energy and toughness at 22 °C," *Journal of Materials Science* 31.8 (1996): 1969-1983.
- [144] R.W. Rice, C.C. Wu, and F. Borchelt. "Hardness–grain-size relations in ceramics," *Journal of the American ceramic society* 77.10 (1994): 2539-2553.
- [145] K.T. Faber and A.G. Evans. "Crack deflection processes—I. Theory," *Acta Metallurgica* 31.4 (1983): 565-576.
- [146] J. Wolfenstine, E. Rangasamy, J.L. Allen and J. Sakamoto. "High conductivity of dense tetragonal Li<sub>7</sub>La<sub>3</sub>Zr<sub>2</sub>O<sub>12</sub>," *Journal of Power Sources* 208 (2012): 193-196.

- [147] R.J. Chen, M. Huang, and W.Z. Huang *et al.* "Effect of calcining and Al doping on structure and conductivity of  $\text{Li}_7\text{La}_3\text{Zr}_2\text{O}_{12}$ ," *Solid State Ionics* 265 (2014): 7-12.
- [148] L. Viswanathan, Y. Ikuma, and A.V. Virkar. "Transformation toughening of  $\beta$ "-alumina by incorporation of zirconia," *Journal of Materials Science* 18 (1983): 109-113.
- [149] D.J. Green, and M.G. Metcalf. "Properties of slip-cast transformation-toughened  $\beta$ "-Al<sub>2</sub>O<sub>3</sub>/ZrO<sub>2</sub> composites," *American Ceramic Society Bulletin* 63.6 (1984): 803-807.